OXFORD

Depleted Mantle-sourced CFB Magmatism in the Jurassic Africa–Antarctica Rift: Petrology and ^{40}Ar/^{39}Ar and U/Pb Chronology of the Vestfjella Dyke Swarm, Dronning Maud Land, Antarctica

Arto V. Luttinen[1]*, Jussi S. Heinonen[1], Matti Kurhila[2], Fred Jourdan[3], Irmeli Mänttäri[2], Saku K. Vuori[2] and Hannu Huhma[2]

[1]Finnish Museum of Natural History, PO Box 44, FIN-00014 University of Helsinki, Finland, [2]Geological Survey of Finland, PO Box 96 (Betonimiehenkuja 4), 02151 Espoo, Finland and [3]Western Australian Argon Isotope Facility, Department of Applied Geology and JdL-CMS, Curtin University of Technology, GPO Box U1987, Perth, WA 6845, Australia

*Corresponding author. E-mail: arto.luttinen@helsinki.fi

ABSTRACT

The Jurassic Vestfjella dyke swarm at the volcanic rifted margin of western Dronning Maud Land represents magmatism related to the incipient Africa–Antarctica rift zone; that is, rift-assemblage magmatism of the Karoo continental flood basalt (CFB) province. Geochemical and Nd–Sr isotopic data for basaltic and picritic dyke samples indicate diverse low-Ti and high-Ti tholeiitic compositions with ε_{Nd}(180 Ma) ranging from +8 to –17. Combined with previously reported data on a subcategory of ferropicritic dykes, our new data facilitate grouping of the Vestfjella dyke swarm into seven geochemically distinct types. The majority of the dykes exhibit geochemical affinity to continental lithosphere and can be correlated with two previously identified chemical types (CT) of the wall-rock CFB lavas and are accordingly referred to as the CT1 and CT3 dykes. The less abundant Low-Nb and High-Nb dykes, a relatively enriched subtype of CT3 (CT3-E) dykes, and dykes belonging to the depleted and enriched ferropicrite suites represent magma types found only as intrusions. The chemically mid-ocean ridge basalt (MORB)-like Low-Nb and the depleted ferropicrite suite dykes represent, respectively, relatively high- and low-degree partial melting of the same overall depleted mantle (DM)-affinity source in the sublithospheric mantle. In contrast, we ascribe the chemically ocean island basalt (OIB)-like High-Nb dykes and the enriched ferropicrite suite dykes to melting of enriched components in the sublithospheric mantle. Geochemical modelling suggests that the low-Ti affinity CT1 and CT3, and high-Ti affinity CT3-E magma types of Vestfjella dyke may predominantly result from mixing of DM-sourced Low-Nb type magmas with <10 wt % of crust- and lithospheric mantle-derived melts. U/Pb zircon dating confirms synchronous emplacement of CT1 dykes and Karoo main-stage CFBs at 182·2 ± 0·9 and 182·2 ± 0·8 Ma, whereas two ^{40}Ar/^{39}Ar plagioclase plateau ages of 189·2 ± 2·3 Ma (CT1) and 185·5 ± 1·8 Ma (depleted ferropicrite suite), and a mini-plateau age of 186·9 ± 2·8 Ma (CT3-E) for the Vestfjella dykes raise the question of whether the onset of rift-zone magmatism could predate the province-wide *c.* 179–183 Ma main stage of Karoo magmatism. Notably variable Ca/K spectra suggest that younger ^{40}Ar/^{39}Ar plagioclase plateau ages of 173, 170, 164, and 154 Ma are related to crystallization of secondary minerals during the late-stage tectono-magmatic development of the Antarctic rifted margin. The occurrence of rare MORB- and OIB-like magma types in Vestfjella and along the African and Antarctic rifted margins suggests melting of geochemically variable depleted and enriched

sublithospheric mantle beneath the Africa–Antarctica rift zone. Our models for the Vestfjella dyke swarm indicate that the voluminous lithosphere-affinity low-Ti and high-Ti rift-assemblage tholeiites could have been derived from MORB-like parental magmas by contamination, which implies sublithospheric depleted mantle as the principal source of the CFB magmas of the Africa–Antarctica rift zone.

INTRODUCTION

The Karoo continental flood basalt (CFB) province is one of the Jurassic–Cretaceous large igneous provinces scattered along the rifted margins of the Atlantic and SW Indian oceans, and, together with the coeval Ferrar province, relates to the initial stages of Gondwana break-up. Erosional remnants of extrusive and intrusive Karoo CFBs are found over an area of $>3 \times 10^6 \, \text{km}^2$ across southern Africa and along the Princess Martha Coast of western Dronning Maud Land (DML), Antarctica (Fig. 1). Geochemical and geochronological investigations have shown that the main stage of Karoo CFB magmatism was emplaced over a duration of *c.* 4 Myr, between *c.* 179 and 183 Ma, and was characterized by province-wide emplacement of relatively monotonous low-Ti tholeiites contemporaneously with formation of a diverse assemblage of high-Ti and low-Ti tholeiites and picrites, nephelinites and rhyolites along the incipient Africa–Antarctica triple rift (e.g. Burke &

Dewey, 1973; Duncan *et al.*, 1984; Luttinen *et al.*, 1998; Jones *et al.*, 2001; Riley *et al.*, 2004, 2005, 2009; Svensen *et al.*, 2007, 2012; Jourdan *et al.*, 2008; Manninen *et al.*, 2008; Neumann *et al.*, 2011) (Fig. 1). We refer to these geographically and geochemically discernible major categories, respectively, as the plateau-assemblage and the rift-assemblage (see Duncan *et al.*, 1984) (Fig. 1). Numerous geochemically defined magma types have been recognized among both assemblages. Nearly all of the Karoo CFB magma types exhibit incompatible element and isotopic compositions that indicate melt contributions from continental crust or lithospheric mantle. This geochemical lithosphere affinity has been frequently interpreted to indicate derivation of the Karoo CFBs largely from subcontinental lithospheric mantle (SCLM) sources (e.g. Hawkesworth *et al.*, 1984; Sweeney *et al.*, 1994; Luttinen & Furnes, 2000; Jourdan *et al.*, 2007a), which indicates a fundamental transition from predominantly
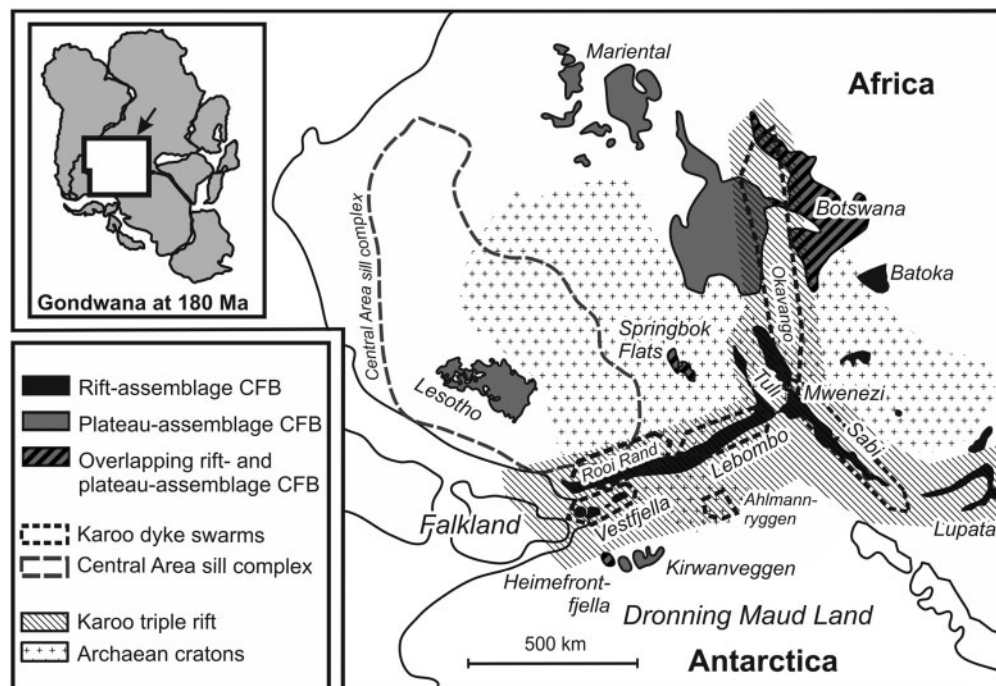

Fig. 1. Distribution of Karoo CFB in a reconstructed Gondwana configuration at *c.* 180 Ma (see inset). Occurrences of extrusive and intrusive CFB related to the Africa–Antarctica rift (rift-assemblage CFB and Karoo dyke swarms) and those found outside the rift system (plateau-assemblage, Central Area sill complex) are indicated in black and grey, respectively. Striped areas indicate regions where plateau-assemblage CFB are intercalated with subordinate rift-assemblage CFB (Botswana, Jourdan *et al.*, 2007a; Springbok Flats, Marsh *et al.*, 1997). Gondwana reconstruction is modified after Lavwer *et al.* (1992). (For definition of the rift- and plateau-assemblages see the main text.)

lithospheric to sublithospheric sources as CFB eruptions gave way to mid-ocean ridge basalt (MORB) magmatism during Gondwana break-up.

This study concerns the age and petrogenesis of the Karoo rift-assemblage CFB (Fig. 1). High-precision geochemical and geochronological data are crucial to understanding the origin of the compositionally diverse rift-assemblage magmas and the evolution from incipient continental rifting to formation of volcanic passive margins. The dataset across the *c.* 1500 km long rift system (Fig. 1) remains rather patchy, however. Large portions of the system lack or have very few rare earth element (REE) and isotopic data (see Duncan *et al.*, 1990; Ellam & Cox, 1991; Sweeney *et al.*, 1994), which, together with uncertainties caused by limited bedrock exposure and faulting (e.g. Klausen, 2009), undermines characterization of magma compositions and their spatial–temporal variations. Furthermore, reliable age data for the rift-assemblage (*c.* 176–182 Ma) are based on silicic extrusive intercalations at relatively high stratigraphic level, as well as silicic and mafic intrusive rocks (Riley *et al.*, 2004; Jourdan *et al.*, 2005, 2007*b*), which renders timing of the onset of magmatism ambiguous. Based on broad enriched (E)-MORB affinities in some of the margin-parallel, late-stage dykes of the rift-assemblage (e.g. Duncan *et al.*, 1990) and structural and geochemical studies of lavas and dykes of the central Lebombo Monocline, progressive lithospheric extension along the Africa–Antarctica rift may have led to incipient oceanic spreading magmatism and successful break-up already at *c.* 176 Ma (Jourdan *et al.*, 2007*b*), and, perhaps in some rift segments, immediately after the main stage of CFB magmatism (Klausen, 2009).

The CFBs of the conjugate Antarctic rifted margin also remain poorly dated (Zhang *et al.*, 2003; Riley *et al.*, 2005), whereas detailed geochemical mapping of the Vestfjella and Ahlmannryggen rift sections has provided insights into the evolution of the Africa–Antarctica rift system: (1) the Antarctic rifted margin is typified by intimate intercalation of geochemically extremely variable CFB lavas and dykes; (2) sublithospheric mantle sources have been identified for some high-Mg CFB dykes at Ahlmannryggen (Riley *et al.*, 2005) and Vestfjella (Heinonen & Luttinen, 2008; Heinonen *et al.*, 2010) (Fig. 1). It has been unclear, however, whether these rare and poorly age-constrained sublithospheric mantle-derived intrusive rock types represent a late-stage transition from a continental to an oceanic tectonic setting (see Jourdan *et al.*, 2007*b*), or main-stage CFB magmas previously inferred only from extrapolations of geochemical trends (e.g. Ellam & Cox, 1991; Ellam *et al.*, 1992).

Here we report geochemical and $^{40}Ar/^{39}Ar$ plagioclase and U/Pb zircon and baddeleyite age data for basaltic and picritic intrusive rocks of the Vestfjella dyke swarm at the volcanic rifted margin of western DML. Our new data and petrogenetic modelling suggest derivation of diverse low-Ti and high-Ti tholeiites mainly from sublithospheric depleted mantle sources and

imply that the rift-assemblage CFBs of Vestfjella may represent relatively early stages of Karoo magmatism.

All $^{40}Ar/^{39}Ar$ ages reported in this study have been recalculated using the ^{40}K decay constants proposed by Renne *et al.* (2011) that have been directly calibrated against the ^{238}U decay constant. This causes $^{40}Ar/^{39}Ar$ ages to be 1% older (+1·8 Ma) than previously reported.

GEOLOGICAL BACKGROUND

Bedrock lithologies
Karoo CFB lavas crop out at four localities in western DML (Fig. 2a): Kirwanveggen, Sembberget, Heimefrontfjella (Björnnutane), and Vestfjella (Faure & Elliot, 1971; Harris *et al.*, 1990; Luttinen & Furnes, 2000; Luttinen *et al.*, 2010). Karoo-related intrusive rocks are more widespread and are also found at Ahlmannryggen, H. U. Sverdrupfjella, and Mannefallknausane (Harris *et al.*, 1991; Zhang *et al.*, 2003; Riley *et al.*, 2005, 2009; Leat *et al.*, 2006) (Fig. 2a). The original size of the Antarctic subprovince is poorly constrained; flood basalts and intrusions may well have extended across a notably larger area than that implied by the exposed bedrock in the coastal ranges and nunataks.

The Jurassic CFB sequences at Kirwanveggen, Sembberget and Heimefrontfjella are located at the East Antarctic Plateau escarpment and overlie Paleozoic sedimentary strata and the Mesoproterozoic Maud Belt basement (Aucamp *et al.*, 1972; Juckes, 1972; Jacobs *et al.*, 1993; Groenewald *et al.*, 1995). The Vestfjella nunataks at the rifted continental margin consist of seaward-dipping flood basalts, minor sedimentary interbeds, and cross-cutting intrusive rocks (Hjelle & Winsnes, 1972). The base of the Vestfjella CFB succession is not exposed: the lava suite may well be underlain by Permian sedimentary rocks similar to those found at Fossilryggen, northeastern Vestfjella (Hjelle & Winsnes, 1972) and the basement probably represents the Maud Belt (Fig. 2b). However, the southern boundary of the Archaean Grunehogna craton, an extension of the Zimbabwe–Kaapvaal craton, is probably nearby (Wolmarans & Kent, 1982; Barton *et al.*, 1987; Krynauw *et al.* 1991; Peters *et al.*, 1991; Corner, 1994; Marschall *et al.*, 2010) (Fig. 2).

Rift-assemblage and plateau-assemblage magmas in DML
The CFBs of the DML subprovince of the Karoo are typified by notably variable incompatible element and isotopic ratios; previous studies have identified up to 17 CFB magma types (Harris *et al.*, 1990; Luttinen *et al.*, 1998, 2010; Vuori & Luttinen, 2003; Riley *et al.*, 2005, 2009; Heinonen & Luttinen, 2008; Heinonen *et al.*, 2010). As in Africa, CFB sequences spatially associated with the Africa–Antarctica rift (Vestfjella and Ahlmannryggen; Fig. 2a) are composed of various tholeiitic low-Ti and high-Ti magma types accompanied by minor silicic and alkaline rock types (Luttinen *et al.*, 2002;
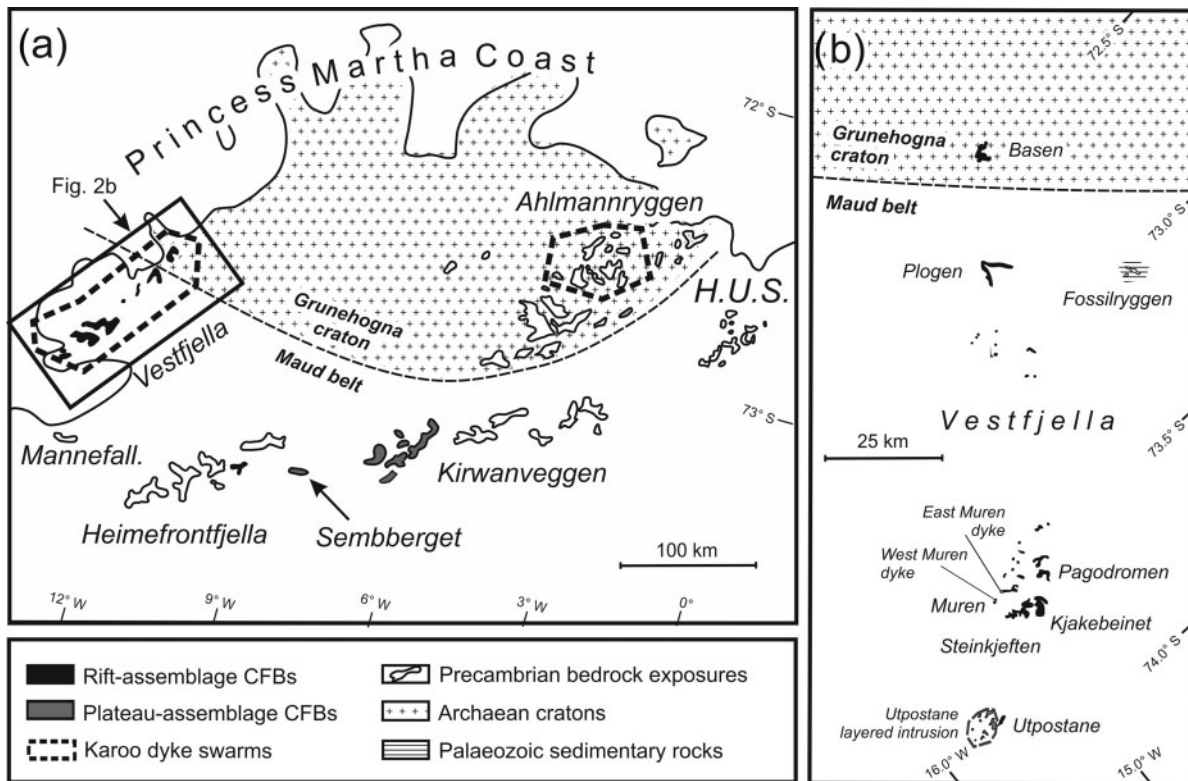
Fig. 2. Distribution of Karoo CFB in (a) western Dronning Maud Land and (b) Vestfjella. Occurrences of CFB related to the Africa–Antarctica rift (rift-assemblage CFB, Karoo dyke swarms) and those found outside the rift system (plateau-assemblage, Utpostane layered intrusion) are indicated in black and grey, respectively. Exposures of Precambrian bedrock and the extent of the Archaean (Grunehogna) craton and Proterozoic (Maud) belt are indicated. The Archaean–Proterozoic boundary is after Corner (1994). H.U.S., H. U. Sverdrupfjella.

Vuori & Luttinen, 2003). The rift-assemblage low-Ti and high-Ti CFBs of DML, previously referred to as the Grunehogna group by Luttinen et al. (2010), exhibit strongly fractionated Sm/Yb ($>1.9 \times$ C1 chondrite) indicative of magma generation at high pressure within the garnet stability field (see Fram & Lesher, 1993). In addition to a strong 'garnet fingerprint', they are typified by pronounced isotopic heterogeneity [e.g. ε_{Nd}(180 Ma) from +9 to –16].

In contrast, the low-Ti CFBs of Kirwanveggen and Sembberget, located furthest away from the rifted margin (Fig. 2a), have only mildly fractionated Sm/Yb ($<1.9 \times$ C1 chondrite) suggestive of relatively low-pressure melting. These basalts have monotonous geochemical characteristics including isotopic compositions [e.g. ε_{Nd}(180 Ma) from +3 to –3], and we refer to them as the plateau-assemblage magmas of DML [Maud group of Luttinen et al. (2010)].

Sparse $^{40}Ar/^{39}Ar$ plagioclase plateau age data for the DML subprovince imply emplacement of rift-assemblage and plateau-assemblage magmas coevally with the Karoo volcanism in southern Africa. The dated samples include a rift-assemblage high-Ti dyke (180.9 ± 1.2 Ma), a plateau-assemblage gabbro (181.2 ± 0.5 Ma), and three plateau-assemblage lavas (183.7 ± 0.6 to 186.0 ± 0.6 Ma) (Duncan et al., 1997; Zhang et al., 2003; all ages recalculated using

$R_{FCs}^{FCTb} = 1.0086 \pm 0.00155$ from Di Vincenzo & Skála, 2009). Evidence of excess argon, Ar-loss, recoil and, more importantly, the lack of plateau ages for other published data render reported younger and older emplacement ages of the tholeiitic magmas doubtful (190–165 Ma; Brewer et al., 1996; Riley et al., 2005; See also Zhang et al., 2003) and these will not be considered further in this study.

Vestfjella dyke swarm

Mafic intrusive rock types are common at the rifted margin of DML; in Vestfjella, exposed dykes locally indicate up to 14% crustal extension (Hjelle & Winsnes, 1972; Vuori & Luttinen, 2003) and geophysical data suggest the presence of several mafic bodies in the adjacent glaciated area (Corner, 1994; Leitchenkov et al., 1996; Ruotoistenmäki & Lehtimäki, 1997). The Vestfjella dyke swarm is composed of texturally and compositionally diverse, aphanitic to coarse-grained basaltic and picritic rock types. The swarm is dominated by subvertical, <10 m wide dykes that mainly strike NE–SW to north–south, although dykes that strike east–west and/or have small dip angles, including concordant sills, are also found (see Hjelle & Winsnes, 1972; Furnes & Mitchell, 1978; Furnes et al., 1982; Peters, 1989; Grind et al., 1991). Previously published geochemical data

combined with the data reported in this study suggest the predominance of subalkaline, tholeiitic compositions broadly similar to the Vestfjella CFB lavas (e.g. Furnes *et al.*, 1982; Luttinen *et al.*, 1998). The gabbroic rocks of East and West Muren are now recognized as two exceptionally wide dykes (*c.* 350 m and *c.* 500 m, respectively) belonging to the dyke swarm (see Vuori & Luttinen, 2003). The Vestfjella ferropicrite suites represent two compositionally distinctive (relatively depleted and enriched) subcategories of dykes with unusually high FeO_{tot} (>13 wt %) at a given MgO (12–18 wt %) (Heinonen & Luttinen, 2008). These suites also include basalt dykes and a few highly magnesian, komatiite-like, glacially transported dike-derived boulders (MgO = 18–24 wt % and TiO_2 = 1·2–1·5 wt %; classified as meimechites according to Le Bas, 2000; see Heinonen & Luttinen, 2010).

The 181 Ma Utpostane layered intrusion (Vuori & Luttinen, 2003; recalculated from Zhang *et al.*, 2003), recently correlated with the plateau-assemblage CFBs of Kirwanveggen and Sembberget (Luttinen *et al.*, 2010) (Fig. 2), and the geochemically distinctive 162 Ma lamproite dykes of south Vestfjella (recalculated from Luttinen *et al.*, 2002) are excluded from the dyke swarm.

DATASET AND ANALYTICAL METHODS

Basaltic and picritic intrusive rocks belonging to the Vestfjella dyke swarm range from aphanitic to coarse-grained. The samples were collected during several Finnarp (Finnish Antarctic Research Programme) expeditions in the period 1989–2008 using rock hammers. Multiple samples were collected from exceptionally wide or laterally well-exposed dykes. New whole-rock, major and trace element, and Sr-isotope data are listed in Tables 1 and 2. The complete dataset for 117 samples from 85 intrusions of the Vestfjella dyke swarm is provided in Supplementary Data Electronic Appendix 1 (supplementary data are available for downloading at http://www.petrology.oxfordjournals. org).

Major and trace elements

All of the major and trace element data were obtained at the Geoanalytical Laboratory, Washington State University. For this study, whole-rock compositions were analyzed for 69 hand-sized samples representing 61 dykes. The samples were ground in a steel jawcrusher and the freshest chips were handpicked for analysis to avoid weathered surfaces and contamination with the preparation equipment. A tungsten carbide mill and a steel mill were used respectively for preparation of powders for X-ray fluorescence (XRF) and inductively coupled plasma mass spectrometry (ICP-MS) analysis to avoid contamination with mill material. Technical notes and principles of these methods have been given by Johnson *et al.* (1999) and Knaack *et al.* (1994), respectively. Repeat analyses of

standards indicate high precision in general (Supplementary Data Electronic Appendix 1).

Nd and Sr isotopes

Isotopic compositions were analyzed at the Research Laboratory of the Geological Survey of Finland (GSF; $n = 15$) and at the NERC Isotope Geosciences Laboratory (NIGL; $n = 10$), Keyworth, UK. For the analyses, we used rock powders initially prepared for the whole-rock ICP-MS analyses. More detailed descriptions of the analytical procedures have been given by Riley *et al.* (2006) and Heinonen and Luttinen (2008).

At GSF, the isotope ratios of Sm, Nd, and Sr were measured on a VG sector 54 mass spectrometer (those of Nd and Sr in dynamic mode), whereas those of Rb were measured using a non-commercial Nier-type mass spectrometer built at GSF. The estimated errors in isotope dilution measurements of $^{147}Sm/^{144}Nd$ and $^{87}Rb/^{86}Sr$ are 0·4% and 0·6%, respectively. The $^{143}Nd/^{144}Nd$ ratio was normalized to $^{146}Nd/^{144}Nd = 0·7219$ and the $^{87}Sr/^{86}Sr$ ratio to $^{86}Sr/^{88}Sr = 0·1194$. The average value for the La Jolla standard is $^{143}Nd/^{144}Nd = 0·511850 \pm 0·000010$ (mean and external 2σ, $n = 18$), and for SRM987 $^{87}Sr/^{86}Sr = 0·710250 \pm 0·000025$ (2σ, $n = 20$). At NIGL, the isotope ratios of Sm, Nd, and Sr were measured on a Finnegan-MAT 262 mass spectrometer (Sr in multidynamic peak-jumping mode and Nd in static collection mode). An in-house J&M Nd isotope standard gave a value of $0·511196 \pm 0·000022$ (2σ, $n = 31$); reported $^{143}Nd/^{144}Nd$ values were normalized to a value of 0·511130 for this standard, equivalent to 0·511864 for La Jolla. The Sr isotope standard NBS987 gave a value of $0·710250 \pm 0·000016$ (2σ, $n = 32$). Age-corrections for NIGL data were calculated using Rb and Sr contents measured by ICP-MS at the Geoanalytical Laboratory. The Nd–Sr isotopic data are reported in Table 2.

U–Pb dating

For U–Pb dating, we collected large (up to 150 kg) samples of zircon-bearing, coarse-grained gabbroids from West Muren (leucogabbro just below the capping felsic unit), and East Muren (gabbronorite from the middle part) intrusions (Fig. 2b; see Vuori & Luttinen, 2003). The samples were crushed in a jaw mill and ground in a roller mill to <0·3 mm grain size. The heavy minerals were concentrated with a shaking table and the magnetic minerals were removed with a Carpco® induced roll magnetic separator. The zircons and baddeleyites were separated according to a method described by Vaasjoki *et al.* (1991). For multigrain isotope dilution thermal ionization mass spectrometry (ID-TIMS) U–Pb dating, the decomposition of minerals and the extraction of U and Pb followed the procedure described by Krogh (1973, 1982). The isotopic analyses were performed at GSF using a VG Sector 54 thermal ionization multicollector mass spectrometer. Isotopic ratios were measured for both $^{235}U–^{208}Pb$ spiked and non-spiked

Table 1: Representative whole-rock geochemical data for the Vestfjella dyke swarm

Sample:	AL/B19c-98	P3-KHG-90	P7-KHG-90	P10-KHG-90	AL/P5-98	AL/P6-98	AVL/P2-03	AL/PD7-98	AL/PD10-98	115-KHG-91	121-KHG-91	218sk-92	AL/P3b-98	AL/P4-98	AL/KB1-98
Magma type:*	CT1	CT1	CT1	CT1	CT1	CT1	CT1	CT1	CT1	CT1	CT1	CT1	CT3	CT3	CT3
Location:*	B	P	P	P	P	P	P	Pd	Pd	Sk	Sk	Sk	P	P	Kb
Width (m):	1	0.7	—	1	8	2	—	4–5	1	4	1	—	—	—	—
Strike/dip:†	000/70	230/75	—	030/40	030/60	040/90	—	026/30	315/?	030/75	120/75	—	295/76	022/82	354/90
Lat. (S):	73°01'42"	73°12'18"	73°13'10'	73°12'38'	73°12'57"	73°13'15"	73°13'23"	73°44'33"	73°44'29"	73°46'17"	73°46'16"	73°46'15"	73°12'40"	73°12'40"	73°47'48"
Long. (W):	13°25'17"	13°49'01"	13°44'42'	13°47'30'	13°49'07"	13°48'56"	13°43'54"	14°45'17"	14°45'02"	14°57'32"	14°55'52"	14°57'58"	13°49'11"	13°49'11"	14°54'55"
Major elements (wt %, normalized to 100% volatile free)															
SiO_2	48.43	51.64	50.76	50.47	49.25	52.91	50.70	52.88	51.65	54.87	50.25	54.93	50.14	46.53	47.67
TiO_2	2.08	1.49	1.24	2.20	1.40	1.63	1.33	1.59	1.37	1.66	1.34	1.60	1.94	2.19	2.31
Al_2O_3	16.06	14.84	13.38	14.96	13.70	15.35	14.21	14.89	13.37	14.78	13.92	15.73	13.19	14.80	14.31
FeO_{tot}	12.87	11.88	11.71	12.92	12.06	10.56	10.95	10.48	11.57	11.17	11.93	11.03	12.31	14.66	14.82
MnO	0.15	0.15	0.18	0.18	0.19	0.16	0.17	0.17	0.17	0.17	0.19	0.16	0.17	0.20	0.26
MgO	6.02	7.65	9.23	5.82	10.61	6.02	9.11	6.41	9.33	4.64	8.98	4.70	7.82	8.21	6.48
CaO	10.58	9.57	10.56	9.64	9.81	10.04	10.77	10.04	9.95	7.98	10.41	6.41	11.72	9.83	11.16
Na_2O	2.79	2.07	2.19	2.56	2.19	2.23	1.85	2.27	1.55	2.58	2.18	2.74	1.99	2.66	1.98
K_2O	0.79	0.53	0.59	0.89	0.64	0.86	0.76	1.05	0.85	1.88	0.63	2.45	0.50	0.64	0.80
P_2O_5	0.23	0.20	0.16	0.35	0.16	0.24	0.16	0.22	0.21	0.26	0.19	0.25	0.21	0.27	0.22
LOI	—	—	—	—	0.43	2.33	—	1.32	3.23	—	2.30	—	1.07	0.97	2.10
Trace elements (ppm) (Cr–Sr by XRF; Sc–Lu by ICP-MS)															
Cr	212	325	650	136	648	77	644	94	755	12	497	35	302	108	134
Ni	177	177	262	102	327	93	228	113	258	60	227	54	142	180	94
V	353	324	319	361	324	303	325	317	277	310	315	279	357	379	377
Cu	234	108	128	137	168	77	150	90	132	66	141	57	173	98	271
Zn	94	84	78	111	92	94	83	94	95	104	87	86	94	115	104
Ga	23	20	19	26	17	20	22	20	18	21	23	24	20	21	22
Zr	164	116	115	173	109	149	116	157	151	212	106	188	132	135	124
Sr	341	339	277	427	277	375	260	329	250	383	305	300	332	500	285
Sc	30	33	36	30	33	30	33	31	33	26	36	24	39	33	37
Ta	0.42	0.31	0.29	0.50	0.37	0.53	0.29	0.50	0.67	0.64	0.30	0.71	0.49	0.58	0.68
Nb	6.8	5.4	5.1	9.0	6.6	9.7	5.3	9.0	12.1	11.4	4.9	12.6	7.8	9.3	10.2
Hf	4.31	3.07	2.96	4.59	2.90	3.98	3.13	4.18	3.79	5.21	2.65	4.87	3.48	3.64	3.36
Y	28	23	22	32	22	26	22	26	24	28	22	29	23	25	27
Ba	185	236	257	381	235	356	251	395	297	747	301	1072	170	296	205
Rb	13	10	12	19	13	10	20	24	10	32	10	41	5	10	10
Cs	0.37	0.53	1.29	2.12	1.07	0.16	0.42	0.63	0.16	0.41	0.26	—	0.12	1.16	0.19
Th	1.89	1.16	1.04	2.12	1.56	2.68	1.35	3.36	2.76	5.07	0.91	4.09	1.10	0.86	1.25
U	0.34	0.25	0.18	0.43	0.25	0.41	0.20	0.53	0.40	0.92	0.17	0.81	0.22	0.22	0.26
Pb	4.48	2.95	3.09	5.69	3.36	6.06	3.90	6.55	6.12	9.45	2.51	8.00	3.03	2.53	2.65
La	16.83	14.35	14.81	22.99	14.15	23.98	15.38	24.98	24.76	33.96	12.44	32.94	13.94	15.02	11.51
Ce	34.82	29.92	29.09	48.87	28.42	47.15	32.29	49.27	46.87	65.99	25.37	63.16	30.01	35.55	26.03
Pr	4.47	3.78	3.58	6.38	3.48	5.57	4.17	5.85	5.36	8.34	3.27	7.18	3.93	4.82	3.54
Nd	20.85	17.05	15.50	27.95	15.51	23.91	17.63	24.70	22.11	33.19	14.74	29.46	18.57	22.70	17.13
Sm	5.95	4.67	4.25	7.31	4.28	5.75	4.35	6.01	5.36	7.06	4.09	6.81	5.15	6.07	5.24
Eu	2.05	1.63	1.42	2.37	1.47	1.85	1.47	1.82	1.59	2.07	1.44	2.03	1.81	2.05	1.80
Gd	6.09	4.80	4.61	7.10	4.56	5.54	4.66	5.65	5.13	6.56	4.36	6.27	5.23	5.89	5.66
Tb	0.97	0.76	0.73	1.14	0.76	0.89	0.77	0.89	0.83	1.02	0.72	0.98	0.83	0.92	0.95
Dy	5.78	4.51	4.39	6.39	4.60	5.03	4.56	5.25	4.85	5.86	4.41	5.57	4.79	5.27	5.64
Ho	1.08	0.86	0.86	1.23	0.88	0.98	0.89	1.00	0.95	1.13	0.83	1.10	0.90	0.97	1.08
Er	2.73	2.20	2.10	3.12	2.22	2.48	2.26	2.57	2.41	2.88	2.18	2.75	2.25	2.44	2.72
Tm	0.36	0.30	0.29	0.42	0.30	0.34	0.31	0.35	0.34	0.40	0.29	0.38	0.29	0.32	0.35
Yb	2.10	1.82	1.72	2.45	1.80	2.05	1.86	2.05	2.02	2.40	1.73	2.25	1.73	1.92	2.08
Lu	0.31	0.28	0.26	0.37	0.27	0.30	0.28	0.32	0.29	0.36	0.27	0.33	0.25	0.29	0.31

(continued)

Table 1: Continued

Sample:	AL/KB7-98	AL/KB13-98	AL/KB14-98	AL/KB20-98	113-KHG-91	127-KHG-91	ALUP11-98	AVL/FR2d-03	AVL/FR2e-03	11-KHG-90	AL/B21a-98	AL/UP2-98	AVL/P1-03	AL/PD8-98	AL/PD9-98
Magma type:*	CT3	CT3	CT3	CT3	CT3	CT3	CT3	CT3	CT3	CT3	CT3	CT3	CT3-E	CT3-E	CT3-E
Location:*	Kb	Kb	Kb	Kb	Sk	E-Mur	Up	Fr	Fr	B	B	Up	P	Pd	Pd
Width (m):	3	2	—	3	2	5	3	—	—	0.5	1	0.5	10	2	2.5
Strike/dip:†	146/80	142/?	130/90	338/76	060/85	350/75	164/90	sill	sill	265/90	095/?	134/90	170/85	—	318/70
Lat. (S):	73°47'02"	73°47'06"	73°47'06"	73°47'52"	73°46'14"	73°43'43'	73°55'22"	73°22'52"	73°22'52"	73°01'55'	73°01'51"	73°55'08"	73°13'23"	73°44'33"	73°44'29"
Long. (W):	14°52'21"	14°52'46"	14°52'46"	14°51'19"	14°58'02"	15°02'09'	15°38'28"	13°05'31"	13°05'31"	13°25'24"	13°25'11"	15°34'47"	13°43'54"	14°45'17"	14°45'02"

Major elements (wt %, normalized to 100% volatile free)

SiO_2	49.04	50.78	50.49	50.01	50.00	48.16	49.98	51.59	51.51	49.20	46.60	50.61	50.76	49.12	50.04
TiO_2	1.57	1.87	1.74	1.68	1.48	1.50	1.93	1.69	1.74	2.36	2.34	1.84	2.81	3.98	2.88
Al_2O_3	15.16	14.88	14.77	14.42	13.05	12.17	13.93	14.47	14.80	13.99	14.46	14.18	12.94	12.07	13.71
FeO_{tot}	11.35	12.74	11.05	11.90	12.05	12.68	12.66	11.25	11.33	12.99	14.39	12.17	14.30	16.33	14.06
MnO	0.18	0.19	0.16	0.18	0.18	0.20	0.19	0.18	0.18	0.18	0.18	0.18	0.24	0.25	0.22
MgO	7.73	5.43	7.16	7.34	10.58	12.66	6.85	6.83	6.28	7.17	7.88	6.97	5.49	4.62	4.75
CaO	12.22	11.31	12.22	11.53	10.12	10.13	11.74	10.90	10.54	10.59	11.35	11.70	10.47	9.75	10.20
Na_2O	2.16	2.32	2.04	2.39	2.11	1.61	2.19	2.50	2.66	2.69	2.06	2.06	2.24	2.35	2.16
K_2O	0.34	0.29	0.13	0.26	0.23	0.68	0.30	0.34	0.73	0.56	0.50	0.09	0.47	1.02	1.49
P_2O_5	0.24	0.19	0.22	0.27	0.20	0.21	0.21	0.23	0.22	0.25	0.24	0.21	0.28	0.50	0.48
LOI	2.03	1.30	1.99	—	2.11	3.00	0.49	—	—	1.04	—	0.69	—	0.80	1.55

Trace elements (ppm) (Cr–Sr by XRF; Sc–Lu by ICP-MS)

Cr	306	100	386	271	754	865	249	388	283	327	390	276	106	78	95
Ni	112	53	104	105	261	372	86	113	91	183	258	110	575	52	52
V	317	373	360	323	301	316	396	330	339	390	396	377	443	377	420
Cu	121	167	158	135	120	121	84	131	149	163	184	163	341	425	97
Zn	87	99	89	90	92	91	106	100	91	119	120	99	119	155	142
Ga	23	20	21	18	22	18	23	21	21	25	28	20	23	27	26
Zr	122	111	90	136	75	78	108	96	92	134	132	116	173	270	210
Sr	271	289	320	323	305	245	277	325	361	338	291	256	192	295	355
Sc	34	37	36	31	33	32	36	32	31	32	34	36	40	35	30
Ta	0.20	0.25	0.40	0.22	0.20	0.20	0.26	0.31	0.28	0.37	0.40	0.28	0.59	1.50	1.22
Nb	3.3	4.2	7.1	3.6	3.8	4.1	5.2	4.8	4.6	6.7	6.6	4.7	9.1	23.0	18.8
Hf	3.01	3.01	2.43	3.45	1.89	1.86	2.89	2.68	2.64	3.58	3.62	3.01	5.00	7.66	5.67
Y	22	28	22	23	19	19	26	26	26	28	29	26	43	56	40
Ba	159	130	106	213	172	116	131	269	322	187	107	75	135	226	400
Rb	3	4	1	5	10	23	3	7	16	11	8	1	11	24	24
Cs	0.05	0.06	0.15	0.99	1.19	0.40	0.03	0.83	0.35	1.94	0.94	0.02	0.34	0.88	0.55
Th	0.30	0.51	0.54	0.34	0.38	0.33	0.26	0.56	0.52	1.14	1.46	1.72	1.48	2.76	3.12
U	0.09	0.12	0.12	0.10	0.06	0.09	0.13	0.16	0.15	0.29	0.29	0.15	0.35	0.62	0.93
Pb	1.78	1.82	1.12	1.55	1.37	1.25	1.76	1.95	1.65	2.47	2.33	1.56	2.32	3.27	2.84
La	6.61	7.26	9.37	7.44	6.82	6.79	8.61	8.86	8.28	11.71	11.81	7.90	13.61	26.40	26.77
Ce	16.21	17.90	20.69	18.32	15.04	15.17	19.72	20.89	19.78	26.34	26.75	18.89	33.32	59.16	56.58
Pr	2.40	2.62	2.84	2.99	2.14	2.22	2.78	2.97	2.85	3.71	3.70	2.75	4.89	7.89	7.23
Nd	12.50	13.47	13.88	14.89	10.39	10.98	14.22	14.13	13.54	17.79	18.30	14.12	23.08	37.92	33.03
Sm	3.90	4.46	4.19	4.30	3.23	3.24	4.54	4.01	3.96	5.64	5.72	4.52	7.11	11.35	8.84
Eu	1.56	1.70	1.56	1.70	1.24	1.19	1.70	1.46	1.46	2.00	2.12	1.69	2.34	3.37	2.65
Gd	4.50	5.21	4.60	5.02	3.79	3.87	5.25	4.82	4.75	5.99	6.28	5.31	8.16	12.17	8.85
Tb	0.76	0.91	0.77	0.82	0.66	0.64	0.88	0.85	0.85	1.03	1.05	0.90	1.44	1.99	1.43
Dy	4.53	5.52	4.58	4.86	3.64	3.67	5.29	5.13	5.14	5.79	6.05	5.44	8.85	11.57	8.35
Ho	0.88	1.11	0.88	0.93	0.70	0.71	1.04	1.04	1.03	1.13	1.16	1.04	1.75	2.21	1.57
Er	2.25	2.84	2.25	2.38	1.79	1.77	2.62	2.68	2.66	2.76	2.82	2.64	4.53	5.45	3.80
Tm	0.30	0.38	0.30	0.32	0.24	0.24	0.35	0.36	0.38	0.36	0.36	0.35	0.63	0.73	0.50
Yb	1.74	2.23	1.76	1.88	1.45	1.41	2.06	2.21	2.12	2.01	2.04	2.07	3.69	4.18	2.89
Lu	0.26	0.33	0.26	0.28	0.21	0.21	0.30	0.33	0.33	0.30	0.29	0.31	0.56	0.61	0.42

(continued)

Table 1: Continued

Sample:	AL/PD11-98	AL/KB19-98	AL/UP5b-98	AL/UP7b-98	AL/BR1-98	21-mk-91	x7-KHG-91	AL/UP3b-98	AL/UP4-98	P1-KHG-90	P6-KHG-90	P8-KHG-90	P11-KHG-90	AVL/P3-03
Magma type:	CT3-E	CT3-E	CT3-E	CT3-E	CT3-E	CT3-E	H-Nb	H-Nb	H-Nb	L-Nb	L-Nb	L-Nb	L-Nb	L-Nb
Location:*	Pd	Kb	Up	Up	Mfk	Mfk	Up	Up	Up	P	P	P	P	P
Width (m):	6	4		2			1	0·5	0·9			3		
Strike/dip:†	358/76	064/52	351/90	026/?	054/90	—	sill	351/90	—	280/45	100/20	170/60	280/40	—
Lat. (S):	73°44′29″	73°47′52″	73°55′09″	73°55′12″	74°36′46″	74°32′30″	73°55′20″	73°55′09″	73°55′09″	73°12′13″	73°13′10″	73°13′22″	73°12′46″	73°13′10″
Long. (W):	14°45′02″	14°51′19″	15°35′10″	15°35′36″	14°40′13″	14°27′40″	15°38′35″	15°35′10″	15°35′10″	13°48′35″	13°44′42″	13°44′16″	13°47′08″	13°44′42″
Major elements (wt %, normalized to 100% volatile free)														
SiO_2	48·28	49·35	46·01	48·26	47·62	48·48	49·08	45·86	48·72	50·02	50·20	50·55	50·27	48·62
TiO_2	3·28	3·53	4·14	3·24	3·14	4·44	2·05	2·38	2·62	1·59	1·69	1·66	1·58	1·72
Al_2O_3	13·37	12·96	13·25	12·85	13·25	11·93	14·59	14·95	13·54	14·14	13·87	13·80	14·04	13·49
FeO_{tot}	15·51	14·21	15·99	16·51	16·28	16·76	12·45	14·39	15·30	12·26	11·65	11·27	12·23	12·11
MnO	0·23	0·22	0·21	0·25	0·25	0·25	0·19	0·21	0·24	0·17	0·18	0·18	0·19	0·17
MgO	5·16	5·42	5·29	5·41	5·93	4·48	6·51	6·37	5·17	7·08	7·73	7·96	6·84	10·16
CaO	10·38	10·37	11·49	10·21	10·08	9·16	10·96	12·40	10·76	12·23	12·07	11·47	11·98	11·68
Na_2O	2·25	2·47	2·60	2·23	2·54	2·96	2·61	1·97	2·32	2·13	2·22	2·59	2·42	1·78
K_2O	1·14	1·05	0·33	0·71	0·57	1·00	1·07	0·53	0·84	0·24	0·23	0·39	0·30	0·13
P_2O_5	0·40	0·41	0·69	0·33	0·35	0·56	0·49	0·94	0·47	0·14	0·15	0·15	0·14	0·14
LOI	1·71	0·88	1·02	0·27	0·15	0·00	0·55	1·35	0·32	—	—	—	—	—
Trace elements (ppm) (Cr–Sr by XRF; Sc–Lu by ICP-MS)														
Cr	84	133	67	119	148	67	93	51	84	248	402	394	242	569
Ni	62	82	57	70	95	32	39	77	66	85	160	170	85	307
V	415	538	523	434	392	448	343	371	414	362	386	358	376	385
Cu	335	323	272	346	373	447	28	136	182	150	168	164	146	182
Zn	136	115	138	149	143	164	101	123	140	96	78	81	91	88
Ga	25	25	27	26	28	30	24	26	26	23	20	21	23	20
Zr	205	252	275	192	190	289	163	237	182	84	84	84	82	76
Sr	330	351	368	246	243	296	536	670	397	246	244	277	263	197
Sc	34	32	30	34	36	33	27	24	30	36	37	35	35	32
Ta	1·24	0·95	1·02	0·82	0·73	1·40	1·10	3·26	2·33	0·20	0·17	0·19	0·19	0·16
Nb	17·7	14·9	15·3	11·8	11·2	23·7	18·8	35·5	24·5	3·1	2·8	3·0	3·1	2·6
Hf	5·55	6·69	7·21	5·20	5·16	8·45	4·17	5·62	4·87	2·26	2·31	2·26	2·20	2·31
Y	41	37	42	42	41	59	28	37	35	22	23	22	22	21
Ba	274	271	348	252	146	312	443	729	355	88	64	105	98	42
Rb	28	21	4	15	17	26	14	6	12	4	6	8	7	3
Cs	0·67	0·39	0·04	0·18	0·48	1·55	0·11	0·04	0·11	0·57	0·77	1·73	1·83	0·43
Th	3·67	1·95	1·48	1·42	1·59	2·45	1·50	2·95	2·87	0·31	0·22	0·30		0·27
U	0·49	0·54	0·37	0·37	0·36	0·64	0·55	1·40	2·28	0·09	0·06	0·08	0·09	0·07
Pb	1·87	4·68	2·62	1·69	2·99	3·90	3·91	3·04	3·57	1·01	0·82	1·18	1·02	0·65
La	21·59	22·26	25·63	16·51	15·36	27·63	25·61	45·83	28·24	5·19	4·29	4·81	5·11	4·43
Ce	47·07	51·99	60·12	37·51	35·46	62·19	53·64	96·14	58·77	12·66	11·78	12·29	12·75	12·03
Pr	6·29	7·16	8·23	5·17	4·94	8·54	6·83	11·87	7·25	1·93	1·87	1·90	1·96	2·04
Nd	29·87	34·40	39·81	25·28	24·48	41·62	29·73	50·98	32·54	10·01	10·21	10·03	10·27	10·65
Sm	8·50	9·43	10·76	7·92	7·59	11·84	7·16	11·49	8·12	3·59	3·69	3·59	3·54	3·49
Eu	2·88	3·09	3·65	2·52	2·41	3·51	2·39	3·75	2·61	1·47	1·36	1·40	1·38	1·49
Gd	9·08	9·25	10·49	8·73	8·47	13·53	6·77	10·33	8·19	4·39	4·55	4·43	4·34	4·19
Tb	1·48	1·43	1·60	1·47	1·41	2·14	1·08	1·49	1·28	0·73	0·78	0·74	0·73	0·73
Dy	8·60	7·98	9·03	8·70	8·34	12·67	6·09	8·14	7·37	4·39	4·58	4·48	4·39	4·43
Ho	1·62	1·47	1·68	1·67	1·64	2·37	1·12	1·46	1·37	0·86	0·89	0·84	0·87	0·84
Er	4·12	3·61	4·12	4·22	4·05	5·75	2·74	3·50	3·41	2·12	2·18	2·14	2·13	2·12
Tm	0·54	0·47	0·54	0·55	0·55	0·78	0·37	0·46	0·46	0·28	0·29	0·28	0·28	0·29
Yb	3·13	2·71	3·16	3·13	3·24	4·54	2·15	2·63	2·62	1·64	1·72	1·65	1·62	1·65
Lu	0·46	0·40	0·46	0·47	0·47	0·64	0·31	0·38	0·39	0·24	0·26	0·24	0·23	0·24

The complete dataset with standard runs is given in Electronic Appendix 1. Unnormalized totals sum 98–100 wt %. LOI, loss on ignition.

*Locations: B, Basen; E-Mur, East Muren; Fr, Fossilryggen; Kb, Kjakebeinet; Mfk, Mannefallknausane; P, Plogen; Pd, Pagodromen; Sk, Steinkjeften; Up, Utpostane.

†Dip direction 90° clockwise from strike.

Table 2: Sr and Nd isotopic data for the Vestfjella dyke swarm

Sample	Type[1]	Rb (ppm)	Sr (ppm)	$^{87}Rb/^{86}Sr$	$^{87}Sr/^{86}Sr$	$^{87}Sr/^{86}Sr$ initial	Sm (ppm)	Nd (ppm)	$^{147}Sm/^{144}Nd$	$^{143}Nd/^{144}Nd$	$^{143}Nd/^{144}Nd$ initial	ε_{Nd}[2] initial
10-KHG-90[3]	CT1	19.2	500	0.1112	0.707139	0.706854	5.0	22.0	0.1371	0.512007	0.511846	−10.9
AL/B19c-98	CT1	13.9	365	0.1103	0.705910	0.705628	6.4	24.7	0.1556	0.512260	0.512077	−6.4
AL/P5-98[4]	CT1	12.7	265	0.1366	0.706775	0.706425	4.0	16.3	0.1491	0.512189	0.512013	−7.6
AL/PD7-98[4]	CT1	24.2	315	0.2190	0.708451	0.707891	5.6	26.1	0.1301	0.512065	0.511912	−9.6
3a-MHR-94	CT1(EM)	19.9	332	0.1725	0.708080	0.707639	5.1	23.8	0.1285	0.511773	0.511622	−15.3
29-SKV-00	CT1(EM)	26.3	336	0.2260	0.708450	0.707872	4.1	19.1	0.1295	0.511782	0.511629	−15.1
31-SKV-00	CT1(EM)	18.1	350	0.1490	0.710760	0.710760	4.1	19.4	0.1289	0.511660	0.511508	−17.5
26e-SKV-00	CT1(EM)	4.0	308	0.0379	0.706320	0.706223	1.6	6.0	0.1562	0.511982	0.511798	−11.8
38-SKV-00	CT1(WM)	15.2	363	0.1207	0.707200	0.706891	4.5	19.3	0.1412	0.512105	0.511939	−9.1
8-MHR-94	CT1(WM)	10.1	335	0.0868	0.706870	0.706648	3.3	13.5	0.1501	0.512211	0.512034	−7.2
34-SKV-00	CT1(WM)	12.4	324	0.1104	0.707260	0.706977	4.2	16.0	0.1574	0.512230	0.512045	−7.0
38-KHG-90[3]	CT3	10.4	292	0.1034	0.704926	0.704661	4.0	14.4	0.1670	0.512732	0.512535	+2.6
AL/P4-98[4]	CT3	9.5	480	0.0564	0.703980	0.703836	5.6	23.7	0.1430	0.512764	0.512596	+3.7
AL/KB13-98[4]	CT3	3.6	271	0.0379	0.703741	0.703644	4.2	14.2	0.1778	0.512821	0.512612	+4.0
AL/KB14-98[4]	CT3	0.9	301	0.0085	0.703840	0.703818	3.9	14.6	0.1617	0.512704	0.512514	+2.1
AL/B21a-98	CT3	7.8	299	0.0756	0.704941	0.704748	5.6	20.0	0.1699	0.512697	0.512497	+1.8
25-KHG-90[3]	CT3-E	17.9	288	0.1803	0.704468	0.704007	8.5	31.5	0.1632	0.512730	0.512538	+2.6
359f-AVL	CT3-E	9.9	222	0.1284	0.705560	0.705231	11.5	42.7	0.1630	0.512697	0.512505	+2.0
AL/PD11-98[4]	CT3-E	28.0	330	0.2418	0.704936	0.704317	8.0	31.1	0.1554	0.512724	0.512541	+2.7
AL/KB19-98[4]	CT3-E	21.0	337	0.1776	0.704269	0.703814	9.0	37.6	0.1440	0.512719	0.512549	+2.8
AL/UP7b-98[4]	CT3-E	14.5	232	0.1781	0.704074	0.703618	7.5	26.9	0.1685	0.512803	0.512605	+3.9
AL/BR1-98[4]	CT3-E	17.2	230	0.2131	0.704532	0.703987	7.2	25.9	0.1680	0.512745	0.512547	+2.8
21-mk-91	CT3-E	27.6	307	0.2587	0.704170	0.703508	11.7	44.5	0.1592	0.512810	0.512622	+4.3
AL/UP3b-98[4]	High-Nb	6.3	631	0.0285	0.704038	0.703965	10.7	52.2	0.1237	0.512544	0.512398	−0.1
AL/UP4-98	High-Nb	12.0	440	0.0788	0.704652	0.704450	7.8	34.4	0.1374	0.512649	0.512487	+1.6
AL/UP10-98	High-Nb	15.7	666	0.0680	0.704527	0.704353	7.0	32.2	0.1314	0.512533	0.512378	−0.5
P4-KHG-90[5]	Low-Nb	4.1	234	0.0510	0.703348	0.703218	3.0	9.4	0.1923	0.513000	0.512773	+7.2
P6-KHG-90	Low-Nb	6.1	250	0.0701	0.703552	0.703373	3.8	11.9	0.1934	0.512981	0.512753	+6.8
P8-KHG-90	Low-Nb	7.9	278	0.0824	0.703680	0.703469	3.5	11.0	0.1893	0.512932	0.512709	+5.9
P27-AVL[6]	Low-Nb	2.4	226	0.0303	0.703262	0.703184	3.6	11.3	0.1919	0.513024	0.512798	+7.7
5-mk-91[5]	Low-Nb	7.5	161	0.1343	0.703692	0.703348	2.7	8.8	0.1849	0.513014	0.512796	+7.6

[1]EM, East Muren gabbro; WM, West Muren gabbro.

[2]Calculated at 180 Ma using the following values: $^{147}Sm/^{144}Nd = 0.1966$ and $^{143}Nd/^{144}Nd = 0.512636$.

[3]Previously published by Luttinen *et al.* (1998).

[4]Samples analyzed at NIGL (Rb and Sr contents measured by ICP-MS, Sm and Nd by isotope dilution; 2σ within-run error of Sr and Nd isotopic ratios typically smaller than ± 10 in the last significant digits); Other samples analysed at GSF (Rb, Sr, Sm, and Nd by isotope dilution; 2σ within-run error of Sr and Nd isotopic ratios typically smaller than ± 50 and ± 12 in the last significant digits, respectively).

[5]Previously published by Heinonen *et al.* (2010).

[6]Previously published by Luttinen & Furnes (2000).

Table 3: Zircon and baddeleyite U–Pb analytical data for East Muren and West Muren gabbros

Sample information / Analysed mineral and fraction	m (mg)	U (ppm)	Pb (ppm)	$^{206}Pb/^{204}Pb$ measured	$^{208}Pb/^{206}Pb$ radiogenic	Isotopic ratios (%)* $^{206}Pb/^{238}U$	$^{207}Pb/^{235}U$	$^{207}Pb/^{206}Pb$	ρ†	Apparent ages (Ma ± 2σ) $^{206}Pb/^{238}U$	$^{207}Pb/^{235}U$	$^{207}Pb/^{206}Pb$
A1651 East Muren gabbro												
(A) zircon: d > 4·3, dark brown, transparent, prismatic, abraded 1 h	0·49	4067	154	2981	0·46	0·0287 ± 0·52	0·1965 ± 0·53	0·0497 ± 0·12	0·98	182·3 ± 1·1	182·2 ± 1·1	180·2 ± 2·7
(B) baddeleyite: abraded 1/2 h	0·50	631	22	1074	0·28	0·0287 ± 0·39	0·1966 ± 0·59	0·0497 ± 0·44	0·66	182·2 ± 0·9	182·2 ± 1·1	182·9 ± 10
A1727 West Muren gabbro												
(A) zircon: d > 4·3, translucent to transparent, fragmentary, brownish, brown inclusions, abraded 1·5 h	0·27	597	35	1322	1·26	0·0287 ± 0·36	0·1962 ± 0·47	0·0496 ± 0·27	0·81	182·2 ± 0·9	181·9 ± 1·2	177·1 ± 6·3

$^{206}Pb/^{238}U$ ages are preferred over other ages (see text). *d*, density fraction (g cm^{-3}).
*Isotopic ratios corrected for fractionation, blank (50 pg) and age-related common lead (Stacey & Kramers, 1975; $^{206}Pb/^{204}Pb \pm 0.2$; $^{207}Pb/^{204}Pb \pm 0.2$; $^{206}Pb/^{204}Pb \pm 0.1$; $^{208}Pb/^{204}Pb \pm 0.2$). Percentages indicate 2σ variation.
†Error correlation of $^{207}Pb/^{235}U$ vs $^{206}Pb/^{238}U$.

solutions. The measured isotopic ratios were corrected for mass fractionation (0·12 ± 0·05% per atomic mass unit for lead) according to repeated analyses of SRM 981 and U500 standards. The U–Pb ages were calculated using the PbDat-program (Ludwig, 1991), and the Isoplot/Ex rev. 3.6 program (Ludwig, 2008) was used for plotting of the data. The concordia age errors have been calculated at the 2σ level, including the decay-constant errors. (For further information, see Table 3.)

$^{40}Ar/^{39}Ar$ dating

Samples with the least-altered plagioclase were selected for dating. Approximately 1–2 kg of each sample was crushed and sieved to < 0·25 mm; plagioclase fractions were obtained using heavy liquid and magnetic separation. Most of the bulk plagioclase fractions were further purified by hand-picking. In the case of sample AL/UP7b-98, however, plagioclase phenocrysts were directly drilled out of the hand specimen. In most cases, both the hand-picked and the bulk plagioclase fraction were used for analysis. The $^{40}Ar/^{39}Ar$ measurements were performed using general procedures that have been described previously (see Foland *et al.*, 1993; Zhang *et al.*, 2003).

Sized aliquots (typically 20–30 mg, but down to a few milligrams in some hand-picked fractions) of plagioclase were irradiated in the Ford Nuclear Reactor, Phoenix Memorial Laboratory, at the University of Michigan, for 36–100 h and were subsequently analysed incrementally by heating to successively higher temperatures using a custom-built resistance-heating, low-blank Mo furnace. Corrections for interfering reactions producing Ar from K, Ca, and Cl were made using factors determined on K_2SO_4 and CaF_2 salts and fused wollastonite irradiated at the same time. An intralaboratory muscovite standard ('PM-1') with a $^{40}Ar/^{39}Ar$ age of 165·3 Ma was used as the monitor. The age for this monitor was determined by simultaneous cross calibration with several monitors including the Fish Canyon Tuff biotite standard (FCT-3) for which an age of 27·84 Ma was adopted at the time of measurement.

Recalculation of $^{40}Ar/^{39}Ar$ ages relative to common monitor and decay constants

Most of the published high-precision $^{40}Ar/^{39}Ar$ age data for the Karoo province are consistent with an FCT-3 monitor age different from that used at Ohio State University (see Le Gall *et al.*, 2002; Jourdan *et al.*, 2004, 2008). We have therefore recalculated our plateau ages using $R_{FCs}^{FCTb} = 1.0086 \pm 0.00155$ (Di Vincenzo & Skála, 2009) (Table 4; raw data are presented in Electronic Appendix 2). Furthermore, the new ages as well as the previously published Karoo ages reported in this study have been updated relative to the ^{40}K decay constants recently proposed by Renne *et al.* (2011), which are fully intercalibrated with the ^{238}U decay constant [see discussion by Renne (2014)]. The uncertainties quoted include the error on the decay constants, which, using the

Table 4: Summary of $^{40}Ar/^{39}Ar$ ages

Sample	Lab. no.	Coordinates	Type	Mineral analyzed	Plateau age* (Ma, ± 2σ)	Total ^{39}Ar released (%)	Attribute	MSWD	P	Interpretation
121-KHG-91	77A51	73°46′16″, 14°55′52″	CT1	raw feldspar	—		No plateau			
115-KHG-91	77A15	73°46′17″, 14°57′32″	CT1	picked plagioclase	189·2 ± 2·3	72	Plateau	0·93	0·46	Crystallization age
115-KHG-91	77A27		CT1	raw feldspar	176·7 ± 1·3	58	Mini-plateau	1·1	0·37	Alteration age
113-KHG-91	77A26	73°46′14″, 14°58′02″	CT3	raw feldspar		—	No plateau			
11-KHG-90)	77A39	73°01′55″, 13°25′24″	CT3	raw feldspar		—	No plateau			
11-KHG-90	77A22		CT3	picked plagioclase		—	No plateau			
11-KHG-90	77A31		CT3	raw feldspar	169·5 ± 1·9	71	Plateau	1·4	0·14	Alteration age
AL/UP7b-98	77A20	73°55′12″, 15°35′36″	CT3-E	picked plagioclase	186·9 ± 2·8	67	Mini-plateau	1·4	0·19	Maximum crystallization age
AL/KB14-98	77A44	73°47′06″, 14°52′46″	CT3	raw feldspar		—	No plateau			
AL/KB14-98	77A45		CT3	raw feldspar	163·8 ± 1·5	79	Plateau	1·1	0·35	Alteration age
AL/KB20-98	77A25	73°47′52″, 14°51′19″	CT3	raw feldspar	153·9 ± 0·9	72	Plateau	1·2	0·32	Alteration age
AL/KB20-98	77A13		CT3	picked plagioclase		—	No plateau			
P5-KHG-90	77A12	73°13′10″, 13°44′42″	Low-Nb	picked plagioclase	172·9 ± 2·9	97	Plateau	1·7	0·1	Alteration age
117-KHG-91	77A16	73°46′23″, 14°56′38″	D-FP	picked plagioclase		—	No plateau			
128-KHG-91	77A30	73°43′43″, 15°02′09″	D-FP	raw feldspar		—	No plateau			
128-KHG-91	77A18		D-FP	picked plagioclase		—	No plateau			
AL/KB17-98	77A47	73°47′30″, 14°50′30″	D-FP	raw feldspar	185·5 ± 1·8	75	Plateau	1·0	0·42	Crystallization age
AL/KB17-98	77A46		D-FP	raw feldspar	183·3 ± 2·3	58	Mini-plateau	0·95	0·49	Double-deck spectrum

*Recalculated using $R^{FCTb}/_{FCs} = 1.0086 ± 0.00155$ (Di Vincenzo & Skála, 2009).

Monte Carlo optimization method of Renne *et al.* (2010), add only an additional +0·1 Ma (2σ) on top the internal uncertainty. The calculated age errors are reported at the 2σ level.

PETROGRAPHY

Dolerite dykes and ferropicrite dykes

In this section we divide the dyke swarm into dolerite dykes, gabbro dykes and the ferropicrite suites. The aphanitic to fine-grained dolerite dykes and sills are typically phenocryst-poor. Many of the samples are aphyric (38%), and the porphyritic samples mainly have less than 5 vol. % of phenocrysts (typically < 2 vol. %). The phenocryst assemblages in order of abundance are olivine + plagioclase (21% of samples), olivine (16%), plagioclase (13%), olivine + plagioclase + clinopyroxene (5%), plagioclase + clinopyroxene (3%), and olivine + clinopyroxene (3%). In general, the phenocryst assemblages correlate with the whole-rock MgO contents and are consistent with the low-pressure crystallization sequence olivine – olivine + plagioclase – olivine + plagioclase + clinopyroxene typical of tholeiites (see Cox *et al.*, 1979). A highly magnesian sample X4-KHG-91 is petrographically distinct with aggregates of large clinopyroxene (< 5 mm) and olivine (< 4 mm) phenocrysts. Inclusions of Cr-rich spinel are common in the olivine phenocrysts of the dolerites. The groundmass consists mainly of a sub-ophitic to diabasic textured assemblage of plagioclase laths and interstitial clinopyroxene and Fe–Ti oxides. Minor quantities of

biotite are found in a few samples. Irregular patches of secondary sheet silicates and opaque minerals are common and we interpret them to represent a hyalophitic texture (i.e. altered glass or devitrified material). Amygdales are found in many samples of the CT1 and CT3 magma types (see below).

The petrographic characteristics of the ferropicrite suites have been reported in detail by Heinonen & Luttinen (2008). In summary, they include olivine ± clinopyroxene porphyritic (samples with MgO > 10 wt %) and aphyric or sparsely plagioclase-phyric types (MgO < 10 wt %). The groundmass is granular and diabasic with plagioclase representing an interstitial phase in the most magnesian samples. Magmatic kaersutite is found in olivine-hosted inclusions and in the groundmass of the enriched ferropicrites (see Heinonen & Luttinen, 2008).

The dyke rocks generally are less altered than the Vestfjella lavas, but plagioclase and olivine have been at least partially replaced by secondary sheet silicates in many samples, whereas augitic clinopyroxene is typically fresh even in strongly altered samples. However, dyke samples from Utpostane, including those belonging to the depleted ferropicrite suite, show replacement of clinopyroxene by tremolite–actinolite owing to contact metamorphism caused by the nearby Utpostane layered intrusion (see Vuori & Luttinen, 2003) (Fig. 2b).

Gabbroic dykes

The petrographic characteristics of the two gabbroic intrusions belonging to the Vestfjella dyke swarm have

been reported in detail by Vuori & Luttinen (2003) and Vuori (2004). The eastward-dipping East Muren dyke is a relatively homogeneous sub-ophitic gabbronorite with minor biotite, opaque minerals, and granophyric intergrowths of quartz and potassic feldspar, as well as traces of apatite and zircon. Olivine gabbros occur within the narrow eastern and western contact zones and pegmatoid patches are found near the western (upper) contact. In contrast, the westward-dipping West Muren dyke has a thin capping marginal felsic unit of amphibole-bearing quartz-diorite and is dominated by olivine cumulates. The mafic part grades downwards from leucogabbro with granophyric intergrowths of interstitial quartz and potassium feldspar and minor opaque minerals and accessory apatite, biotite, and zircon to increasingly olivine-rich poikilitic olivine gabbro with minor biotite and opaque minerals and traces of apatite.

GEOCHEMISTRY

Here we describe our new geochemical data on the Vestfjella dyke swarm (Tables 1 and 2) and subsequently use these and previously published data to summarize the key geochemical characteristics of the various magma types (Supplementary Data, Electronic Appendix 1).

Major and trace element compositions

The sampled Vestfjella dykes and sills are subalkaline, quartz- or olivine-tholeiitic basalts. Five samples are basaltic andesite and four are picrites based on MgO content >12 wt % (see Le Bas, 2000). The loss on ignition (LOI) values are mainly <2 wt % with the higher values associated with the amygdaloidal dykes of the CT1 and CT3 magma types (see below). We consider that the whole-rock compositions of the relatively weakly altered dykes correspond to magma compositions, although the concentrations of Cs, Rb, and K in single samples should be viewed with caution (see Luttinen & Furnes, 2000).

Mg-number [molar $Mg/(Mg + 0.85Fe_{tot})$] varies from 0.75 to 0.36 and the major element concentrations also vary considerably: the MgO (4–20 wt %) contents correlate negatively with TiO_2 (1.2–4.8 wt %; Fig. 3c), P_2O_5 (0.1–0.9 wt %; Fig. 3d), and FeO_{tot} (10–18 wt %; Fig. 3b), with a pronounced steepening of the trend at MgO of 7–8 wt %. Similar negative correlation can also be observed in the case of Na_2O (1.5–3.7 wt %), K_2O (0.1–2.5 wt %), and SiO_2 (46–55 wt %), although with a relatively larger scatter that probably stems mainly from secondary alteration (see Luttinen & Furnes, 2000). The Al_2O_3 (9–16 wt %; Fig. 3a) and CaO (6–13 wt %) concentrations show concave arrays with the highest concentrations at MgO of ~7–8 wt %.

The concentrations of compatible trace elements, such as Ni (20–580 ppm), show a strong positive correlation with MgO (Fig. 3e). Incompatible high field strength

elements (HFSE), such as Zr (70–290 ppm), Nb (2–35 ppm), and Y (17–62 ppm), show wide ranges and negative correlation with MgO (Fig. 3f–h). Chondrite-normalized REE patterns range from strongly light REE (LREE) enriched to mildly LREE depleted [$(La/Sm)_N = 0.7$–3.0] and lack noticeable Eu anomalies [$Eu/Eu^* = Eu_N/(Sm_N \times Gd_N)^{0.5} = 0.92$–1.36], whereas heavy REE (HREE) are invariably strongly depleted relative to the middle REE [MREE; $(Sm/Yb)_N = 2.0$–4.8] (Fig. 4).

Mantle-normalized incompatible element patterns show highly variable trace element ratios such as Ti/Zr, La/Nb, and Th/Ta (Fig. 5), which do not correlate with MgO. The concentrations of Ba, K, and Pb typically are enriched relative to other large ion lithophile elements (LILE) and HFSE. Incompatible element characteristics are discussed in further detail below.

Nd and Sr isotope compositions

Nd–Sr isotopic data for 31 dolerite and gabbro samples are reported in Table 2 and illustrated in Fig. 6. Initial isotopic compositions were calculated at 180 Ma despite the marginally older ages indicated by our age data. The dolerite dykes and sills and the gabbros record highly variable initial ε_{Nd} (+8 to –17) and $^{87}Sr/^{86}Sr$ (0.70318–0.71038) and form a scattered array from values corresponding to depleted MORB mantle (DMM) (at 180 Ma) across the entire Nd and Sr isotope compositional range previously reported for the Karoo rift-assemblage CFBs (see Hawkesworth *et al.*, 1984; Harris *et al.*, 1990; Sweeney *et al.*, 1994; Luttinen *et al.*, 1998, 2010; Luttinen & Furnes, 2000; Riley *et al.*, 2005; Jourdan *et al.*, 2007a; Heinonen & Luttinen, 2008) (Fig. 6). The relatively good correlation between initial $^{87}Sr/^{86}Sr$ and $^{143}Nd/^{144}Nd$ ($r^2 = 0.90$) suggests that the Sr isotopic compositions have not been strongly affected by alteration. The isotopic data are discussed further below.

MAGMA TYPES OF THE VESTFJELLA DYKE SWARM

Previous studies of the Vestfjella CFB lavas have grouped the samples into three chemical types (CT1, CT2, CT3; Luttinen *et al.*, 1998; Luttinen & Furnes, 2000). Additionally, two intrusive ferropicrite suites have been identified in Vestfjella (Heinonen & Luttinen, 2008). The diagnostic chemical characteristics of the Vestfjella magma types are summarized in Table 5. Apart from the ferropicrite suites (Fig. 3), identification of magma types among the dykes is generally not quite as straightforward as in the case of the Vestfjella lavas owing to the larger scatter of the data. Nevertheless, detailed examination of the geochemical dataset (Supplementary Data Electronic Appendix 1) in a Ti/Zr vs Ti/P diagram, previously used to group the Vestfjella CFB lavas, indicates clustering of the dolerite and gabbro compositions in the fields of the stratigraphically predominant CT1 and CT3 lavas (Fig. 7). Dykes compositionally similar to stratigraphically subordinate CT2
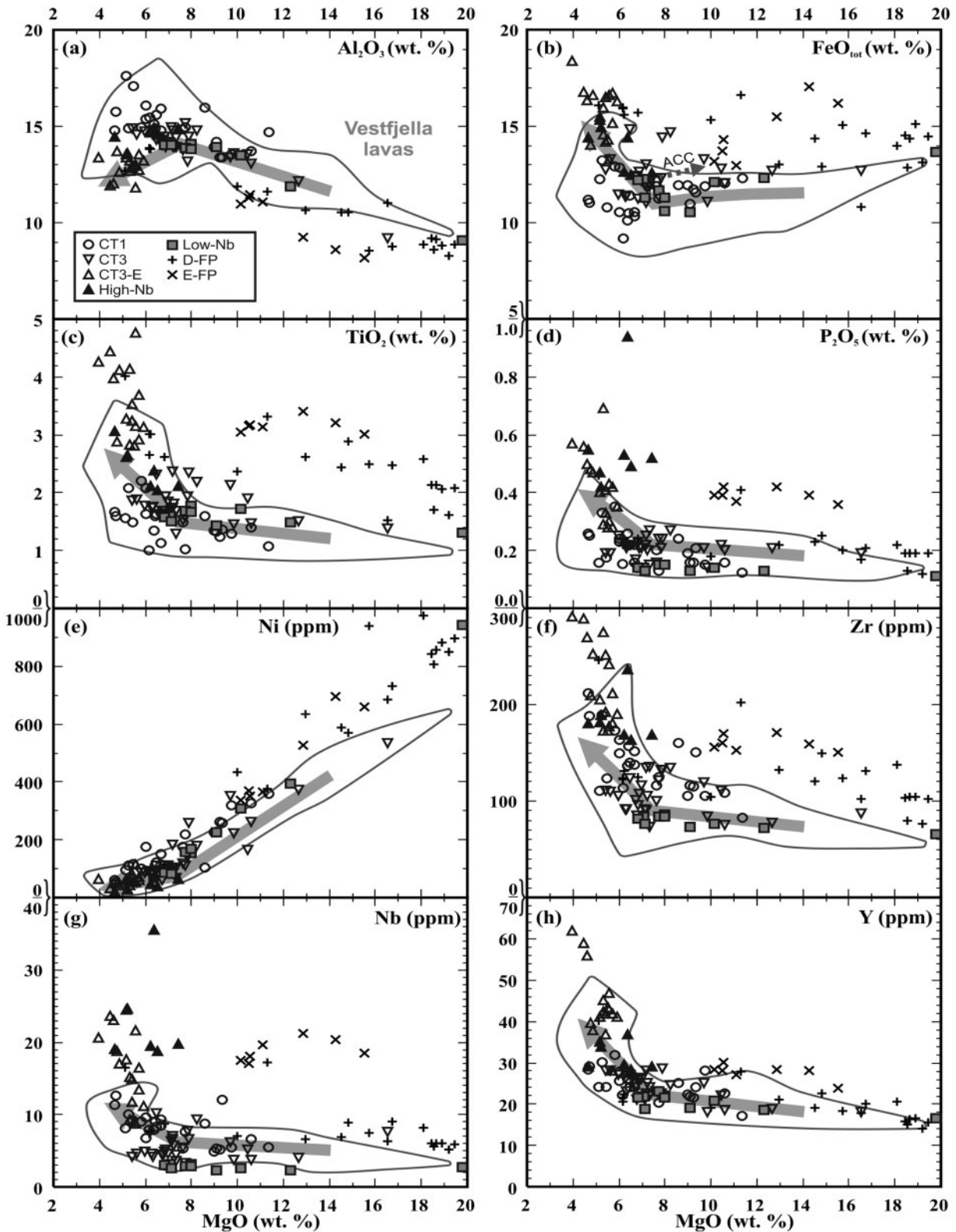
Fig. 3. Al_2O_3, FeO_{tot}, TiO_2, P_2O_5, Ni, Zr, Nb, and Y vs MgO compositions of the Vestfjella dykes (D-FP, depleted ferropicrite suite; E-FP, enriched ferropicrite suite; see Supplementary Data Electronic Appendix 1 for detailed data sources). Compositional fields for the Vestfjella lavas (Luttinen *et al.*, 1998; Luttinen & Furnes, 2000) are shown for comparison. The modelled liquid lines of descent for a hypothetical parental melt with decreasing pressure (5–1 kbar; grey arrow) were calculated using the PELE software (Boudreau, 1999; model results given in Electronic Appendix 3). The parental melt is the average of picritic Vestfjella dyke and lava samples (MgO = 12–19 wt %; ferropicrite suites excluded). Effect of olivine accumulation (ACC; Fo_{76} equilibrium olivine added to sample AL/UP2-98) on FeO_{tot} is also shown.
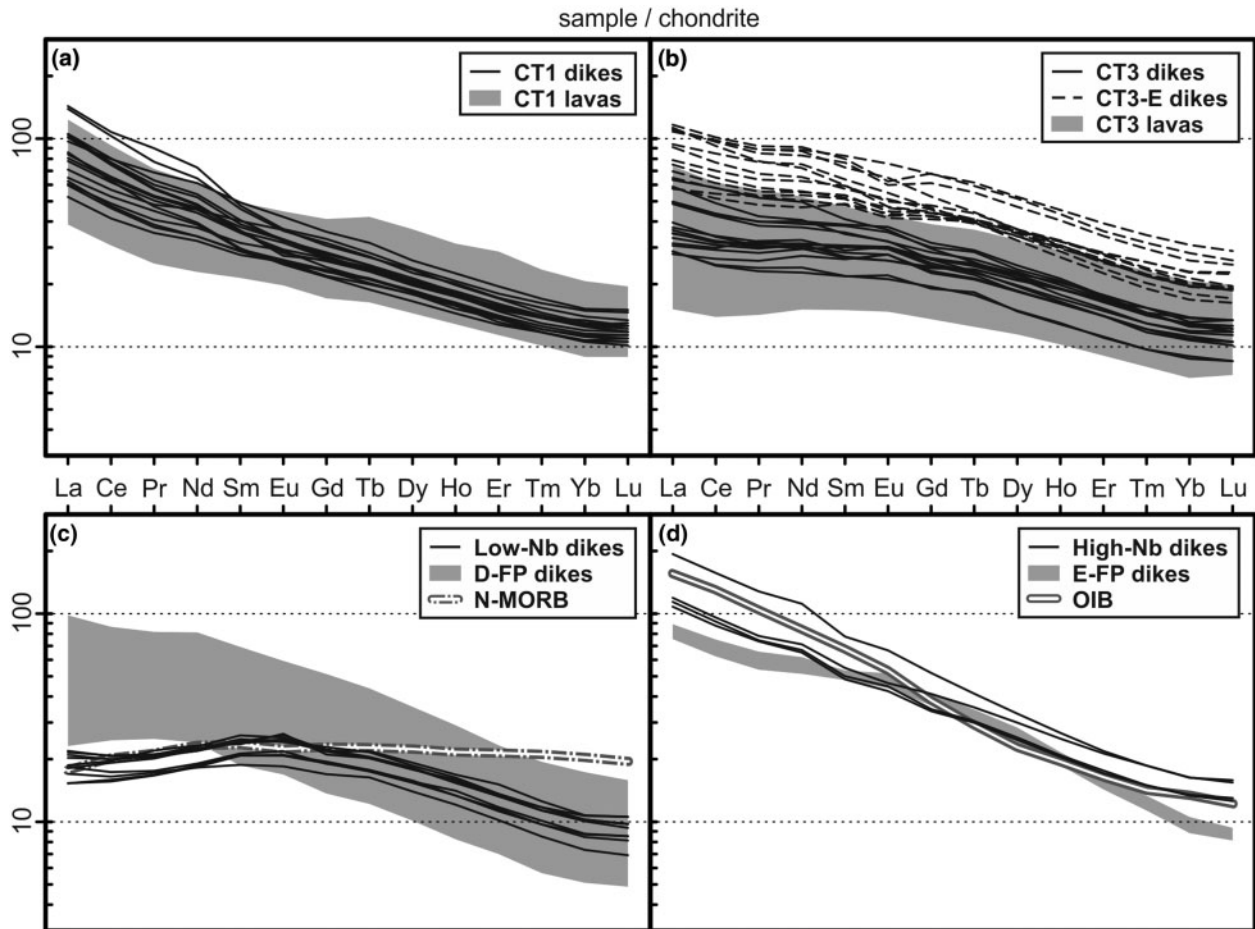
Fig. 4. Chondrite-normalized (McDonough & Sun, 1995) REE patterns for (a) CT1 dykes (cumulate gabbro samples not shown), (b) CT3 dikes, (c) Low-Nb dykes, and (d) High-Nb dykes. Data for CT1 and CT3 lavas (Luttinen *et al.*, 1998; Luttinen & Furnes, 2000), depleted (D-FP) and enriched (E-FP) ferropicrite suites (Heinonen & Luttinen, 2008; Heinonen *et al.*, 2010), average N-MORB (Gale *et al.*, 2013), and average OIB (Sun & McDonough, 1989) are shown for comparison.

lavas (intermediate Ti/Zr, high Ti/P; Fig. 7) were not observed. Further analysis of data using incompatible element ratios, primitive mantle-normalized incompatible element patterns and isotopic data (Figs 3–6) facilitates grouping of the Vestfjella dyke swarm into five magma types (Table 5). We point out that dyke samples that were originally assigned to the CT2 category by Luttinen *et al.* (1998) and Luttinen & Furnes (2000) are regrouped here into CT3, CT3-E, and Low-Nb (see Heinonen *et al.*, 2010).

CT1 magma type

Twenty dolerite dykes and sills, including the gabbroic dykes at West and East Muren, are grouped into the low-Ti affinity CT1 magma type. These rocks have relatively low Ti/Zr (45–80) and Ti/P (7–14) coupled with high $(La/Sm)_N$ (1·8–3·0) and $(Sm/Yb)_N$ (2·5–3·3) (Figs 4a and 7; Table 5) and they are found across Vestfjella. The spiked primitive mantle-normalized incompatible element patterns show an overall enrichment from Lu to Ba combined with negative Ti, P, Nb, and Ta anomalies and a positive Pb anomaly typical of many CFBs (Fig. 5a). Similar to the CT1 lavas, the CT1 dykes show

variably high $(Th/Ta)_N$ (1·5–3·3; Fig. 5a; Table 5) and consistently negative initial ε_{Nd} (from –6·4 to –17·5) and high initial $^{87}Sr/^{86}Sr$ (0·7056–0·7104) (Fig. 6).

CT3 magma type

Thirty-nine dykes are grouped into the CT3 magma type. These rocks are found across the Vestfjella range and are characterized by high Ti/Zr (70–120), low to moderate Ti/P (8–16), moderate $(La/Sm)_N$ (1·0–1·9) at high $(Sm/Yb)_N$ (2·0–3·8), and relatively high initial ε_{Nd} (from +1·8 to +4·3) and low initial $^{87}Sr/^{86}Sr$ (0·7035–0·7052) (Figs 4b, 6 and 7). Twenty-five of the CT3 dykes are similar to the CT3 lavas (Table 5; Fig. 5b) and can be associated with Karoo low-Ti CFBs, but 14 samples are relatively more evolved and enriched in incompatible elements [e.g. high TiO_2 (2·8–4·8) and Zr (170–290) contents (Fig. 3c and f)]; we refer to them as subtype CT3-E. In the conventional low-Ti vs high-Ti grouping of Karoo CFBs (see Erlank *et al.*, 1988), the CT3-E dykes would be ascribed to high-Ti affinity (Table 5). Nevertheless, we group them together with CT3 owing to a likely petrogenetic linkage indicated by the conformity of mantle-normalized incompatible element patterns.
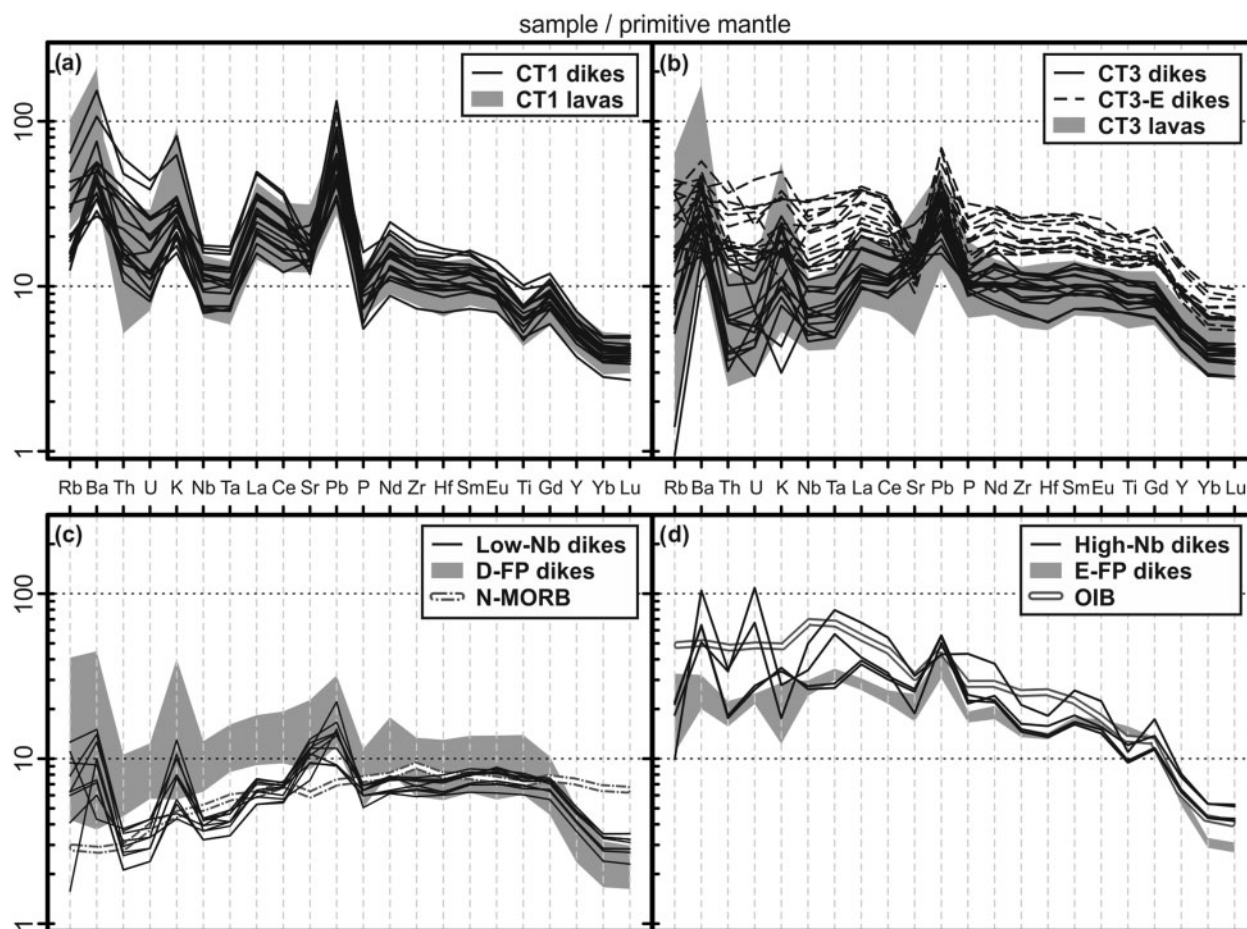
Fig. 5. Primitive mantle-normalized (Sun & McDonough, 1989) incompatible element patterns for (a) CT1 dykes, (b) CT3 dykes, (c) Low-Nb dykes, and (d) High-Nb dykes. Cumulate or highly altered samples are not shown for clarity. Data for CT1 and CT3 lavas (Luttinen *et al.*, 1998; Luttinen & Furnes, 2000), depleted (D-FP) and enriched (E-FP) ferropicrite suites (Heinonen & Luttinen, 2008; Heinonen *et al.*, 2010), average N-MORB (Gale *et al.*, 2013), and average OIB (Sun & McDonough, 1989) are shown for comparison.

Most of the CT3 dykes exhibit primitive mantle-normalized incompatible element patterns typified by an overall convex shape caused by relatively depleted highly incompatible elements Th, U, Nb and Ta and the HREE contrasted by pronounced positive Ba, K, and Pb anomalies; the least-evolved dykes also show positive Sr anomalies (Fig. 5b). Some of the most altered samples show less pronounced or negative anomalies in these mobile elements. The CT3-E dykes have similar incompatible element patterns to the normal CT3 dykes, but at higher concentration levels. Their positive Ba, K, and Pb anomalies are smaller, however, and the negative Sr anomalies probably stem from plagioclase fractionation. Both subtypes of CT3 have relatively unfractionated $(Th/Ta)_N$ in general, but they also include samples characterized by enriched Th and U contents with $(Th/Ta)_N > 3$ (Fig. 5b).

Low-Nb magma type

Seven dykes from Plogen and Mannefallknausane (Fig. 2) are grouped as the Low-Nb magma type (Table 5). They have high Ti/Zr (110–140), Ti/P (15–17), and initial ε_{Nd} (from +5·9 to +7·7) combined with low

initial $^{87}Sr/^{86}Sr$ (0·7032–0·7035) and distinctively low concentrations of immobile highly incompatible elements (e.g. Nb 2–3 ppm) and low Nb/Y (0·1–0·2) (Figs 3g, 6 and 7). They are depleted in LREE and HREE with $(La/Sm)_N = 0·7–0·9$ and $(Sm/Yb)_N = (2·3–2·6)$ (Fig. 4c); their primitive mantle-normalized incompatible element patterns are somewhat normal (N)-MORB-like owing to depletion of Th, U, Nb and Ta (Fig. 5c). The otherwise smooth incompatible element patterns are characterized by positive Ba, K, Pb, and Sr anomalies similar to those of many CT3 dykes. The Low-Nb magma type can be classified as Karoo low-Ti CFB, but, importantly, it shows a strong geochemical resemblance to the high-Ti affinity depleted ferropicrite suite of Vestfjella with similar incompatible element patterns and DM-like Nd and Sr isotopic compositions (Figs 5–7). This resemblance is further supported by Pb and Os isotope data previously reported by Heinonen *et al.* (2010).

High-Nb magma type

Six closely spaced dykes from Utpostane make up the High-Nb magma type (Table 5). These dykes are typified by moderate Ti/Zr (60–100), low Ti/P (3–9), high
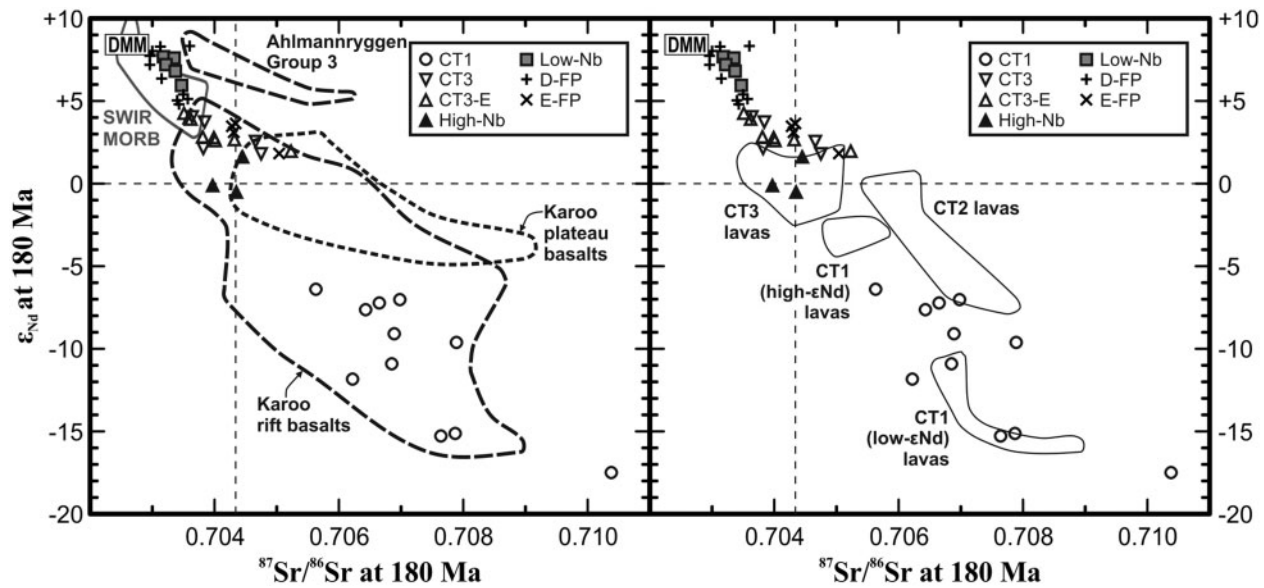
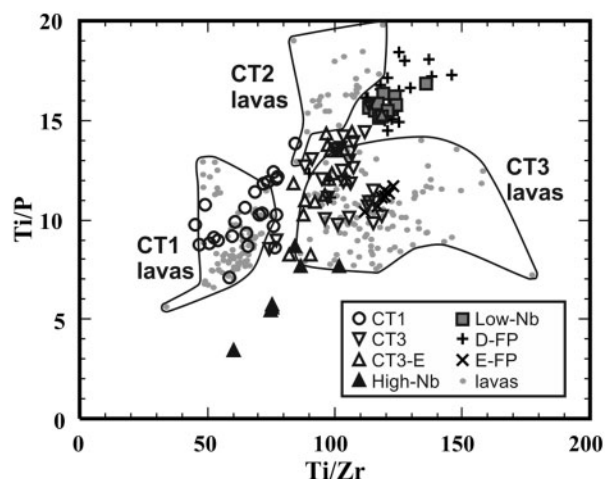**Fig. 6.** Initial ε_{Nd} vs $^{87}Sr/^{86}Sr$ (180 Ma) compositions of the Vestfjella dykes (D-FP, depleted ferropicrite suite; E-FP, enriched ferropicrite suite; see Supplementary Data Electronic Appendix 1 for data sources) compared with those of (a) Karoo rift-assemblage and plateau-assemblage CFBs (Hawkesworth *et al.*, 1984; Ellam & Cox, 1989; Harris *et al.*, 1990; Sweeney *et al.*, 1994; Luttinen *et al.*, 1998, 2010; Luttinen & Furnes, 2000; Riley *et al.*, 2005, 2006; Jourdan *et al.*, 2007a; Neumann *et al.*, 2011) and (b) rift-assemblage lavas of Vestfjella (Luttinen *et al.*, 1998; Luttinen & Furnes, 2000). Compositions of rift-assemblage Group 3 dykes of Ahlmannryggen (Riley *et al.*, 2005), depleted MORB mantle (DMM; Workman & Hart, 2005), and SWIR MORB (compiled from the Petrological Database of the Ocean Floor (http://www.petdb.org)) are also indicated. DMM and SWIR MORB have been back-calculated to 180 Ma using Rb/Sr and Sm/Nd of the DMM reservoir (Workman & Hart, 2005).

Table 5: Pertinent geochemical characteristics of the Vestfjella magma types

Magma type:	CT1 lavas low-Ti	CT1 dykes low-Ti	CT2 lavas trans-Ti	CT3 lavas low-Ti	CT3 dykes low-Ti	CT3-E dykes high-Ti	Low-Nb dykes low-Ti	D-FP dykes trans-Ti	High-Nb dykes high-Ti	E-FP dykes high-Ti
TiO_2 (wt %)	0·8–1·8	0·5–2·2	1·6–3·5	1·0–2·8	1·3–2·4	2·8–4·8	1·3–1·8	1·3–4·0	2·1–3·1	3·0–3·5
MgO (wt %)	4–26	5–11	5–12	4–19	5–17	4–6	7–20	5–28	5–7	10–16
Ti/Zr	49–73	45–84	85–113	89–121	70–118	82–118	113–137	90–146	60–102	112–123
Ti/P	7–12	7–14	13–19	8–13	8–16	8–15	15–17	11–18	3–9	10–12
$(La/Sm)_N$*	2·2–2·8	1·8–3·0	1·2–1·9	1·0–1·9	1·0–1·7	1·2–1·9	0·7–0·9	1·1–1·8	2·2–2·5	1·5–1·7
$(Sm/Yb)_N$*	2·1–2·9	2·5–3·3	2·0–2·9	1·9–2·8	2·0–3·4	2·1–3·0	2·3–2·6	3·2–5·0	3·4–4·8	4·9–5·4
ε_{Nd} (max/min)†	–3/–16	–6/–18	0/–8	+2/–2	+4/+2	+4/+2	+8/+6	+8/+5	+2/–1	+4/+2

*$(La/Sm)_N$ and $(Sm/Yb)_N$ are chondrite-normalized values (McDonough & Sun, 1995).
†ε_{Nd} values are calculated at 180 Ma.
Data for the CT1–CT3 lavas are from Luttinen *et al.* (1998) and Luttinen & Furnes (2000), and data for the CT1, CT3, CT3-E, Low-Nb, High-Nb, and the depleted ferropicrite (D-FP) and enriched ferropicrite (E-FP) suite dykes are from Supplementary Data Electronic Appendix 1 (see references therein).

$(La/Sm)_N$ (2·2–2·5) and $(Sm/Yb)_N$ (3·4–4·8), and close to chondritic initial ε_{Nd} (from –0·5 to +1·6) and $^{87}Sr/^{86}Sr$ (0·7040–0·7045) values (Figs 4d, 6 and 7). They are readily distinguished by their relatively smooth, OIB-like primitive mantle-normalized incompatible element patterns and remarkably high Nb/Y (0·7–1·0) and Nb/Zr (>0·1) (Fig. 5d). The High-Nb dykes show geochemical affinities to the enriched ferropicrite suite of Vestfjella (Fig. 5d) and could be also classified as Karoo high-Ti magmas on the basis of relatively high TiO_2 (2–3 wt %). Two dykes show enrichment of U; we do not provide an explanation for this anomalous character, but point out that the High-Nb dykes are metamorphosed by the nearby Utpostane layered intrusion.

The depleted and enriched ferropicrite suites

Geochemical data for the ferropicrite suites from Basen, Kjakebeinet and Muren have been reported by Heinonen & Luttinen (2008) and Heinonen *et al.* (2010) (see Table 5).

Samples representing 11 dykes belonging to the depleted ferropicrite suite show notably variable MgO (5–28 wt %) and can be classified as basalt, (ferro)picrite and meimechite, with TiO_2 contents ranging from 1·3 to 4 wt % and indicating a transitional character between low-Ti and high-Ti magma types. The depleted ferropicrite suite is typified by high Ti/Zr (90–150) and Ti/P (11–18), relatively low $(La/Sm)_N$ (1·1–1·4), and high $(Sm/Yb)_N$ (3·2–4·6) coupled with high initial ε_{Nd} (+5 to +8) and low

Fig. 7. Ti/P vs Ti/Zr for the Vestfjella dykes (D-FP, depleted ferropicrite suite; E-FP, enriched ferropicrite suite; see Supplementary Data Electronic Appendix 1 for data sources). Compositions of Vestfjella CT1, CT2, and CT3 lavas (Luttinen *et al.*, 1998; Luttinen & Furnes, 2000) are shown for comparison.
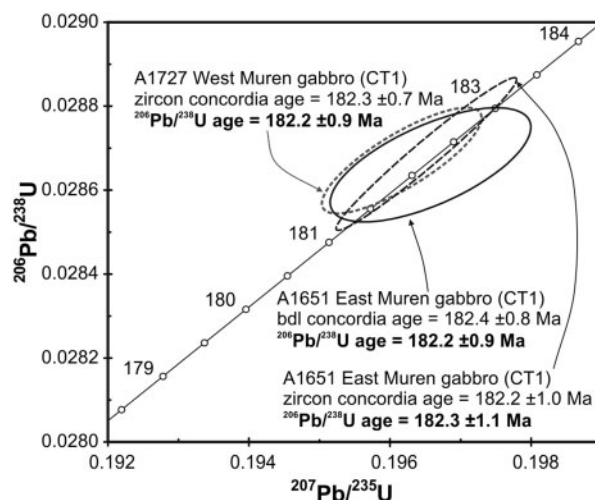

Fig. 8. Concordia diagram showing zircon and baddeleyite (bdl) U–Pb analytical results for the gabbroic CT1 dykes of West and East Muren (Table 4). $^{206}Pb/^{238}U$ ages are preferred over concordia ages.

initial $^{87}Sr/^{86}Sr$ (0·7030–0·7036) (Figs 4c, 6 and 7). The relatively smooth primitive mantle-normalized incompatible element patterns of the depleted subtype show relative depletion of highly incompatible elements (Th, U, Ta, Nb); together with their DM-affinity Sr, Nd, Pb, and Os isotopic compositions this indicates compositional affinity to the low-Nb dykes (Figs 5c and 6a) (Heinonen *et al.*, 2010). Some of the depleted ferropicrite dykes also exhibit positive Ba, K, Sr, and Pb anomalies (Fig. 5c).

The enriched ferropicrite suite includes one basaltic and one picritic dyke that can be readily distinguished by their general enrichment of highly incompatible elements (e.g. Nb 17–21 ppm) at a given MgO (10–15 wt %; Fig. 3g). They have $(La/Sm)_N$ of 1·5–1·7, $(Sm/Yb)_N$ of 4·9–5·5, initial ε_{Nd} from +2 to +4, and initial $^{87}Sr/^{86}Sr$ of 0·7043–0·7050 (Figs 4 and 6). Concentrations of TiO_2 (3·0–3·5 wt %) are typical of high-Ti magma types. The primitive mantle-normalized incompatible element patterns are relatively smooth and resemble those of average ocean island basalts, although the concentrations are somewhat lower in the enriched ferropicrites (Fig. 5d).

GEOCHRONOLOGY

The results of $^{40}Ar/^{39}Ar$ plagioclase and U–Pb zircon and baddeleyite dating of the Vestfjella dyke swarm are summarized in Figs 8 and 9 and Tables 3 and 4. The complete $^{40}Ar/^{39}Ar$ dataset is listed in Supplementary Data Electronic Appendix 2. Owing to uncertainties related to the decay constant of ^{235}U (Schoene *et al.*, 2006; Mattinson, 2010), we have used $^{206}Pb/^{238}U$ results for age calculations. The obtained U/Pb ages are in all cases the same as the concordia ages (Fig. 8). Previous dating of Vestfjella CFBs demonstrated a secondary overprint of the plagioclase Ar spectra in visually

weakly altered lava and dyke samples (Zhang *et al.*, 2003). Our hand-picked plagioclase fractions typically are small owing to secondary alteration and strict selection criteria. Samples representing the High-Nb magma type and the enriched ferropicrite suite were considered unsuitable for dating owing to alteration or lack of plagioclase phenocrysts. The errors are reported at the 2σ level.

Dating of CT1 magma type

Two dolerite dykes representing the CT1 magma type were selected for $^{40}Ar/^{39}Ar$ plagioclase dating. The $^{40}Ar/^{39}Ar$ step-heating spectrum of sample 121-KHG-91 is indicative of excess Ar, and a plateau age cannot be determined. The bulk (= raw) plagioclase fraction of sample 115-KHG-91 gave a low-temperature miniplateau age of 176·7 ± 1·3 Ma (2σ including all sources of uncertainties; MSWD = 1·1; P = 0·37) that includes 58% of ^{39}Ar released (Fig. 9a), whereas the hand-picked fraction gave a plateau age of *c.* 189·2 ± 2·3 Ma (MSWD = 0·93; P = 0·46) that includes 72% of ^{39}Ar released (Fig. 9b). The low-temperature age probably reflects secondary processes associated with sericitized plagioclase (see Zhang *et al.*, 2003; Verati & Jourdan, 2014), whereas the picked pristine plagioclase separate, which yielded a nearly constant Ca/K signal, is interpreted as the emplacement age of the CT1 dyke at *c.* 189 Ma. It should be noted that this age is older than any of the preferred ages of Karoo CFBs and, if confirmed, implies that the southern Vestfjella lavas and dykes may represent an exposure of significantly older magmatism than the Karoo main-stage CFBs [see compilation of Jourdan *et al.* (2008)].

Zircon-bearing samples of two CT1 gabbro dykes were used for U/Pb dating. Sample A1727 represents a medium-grained gabbro from the roof zone of the West
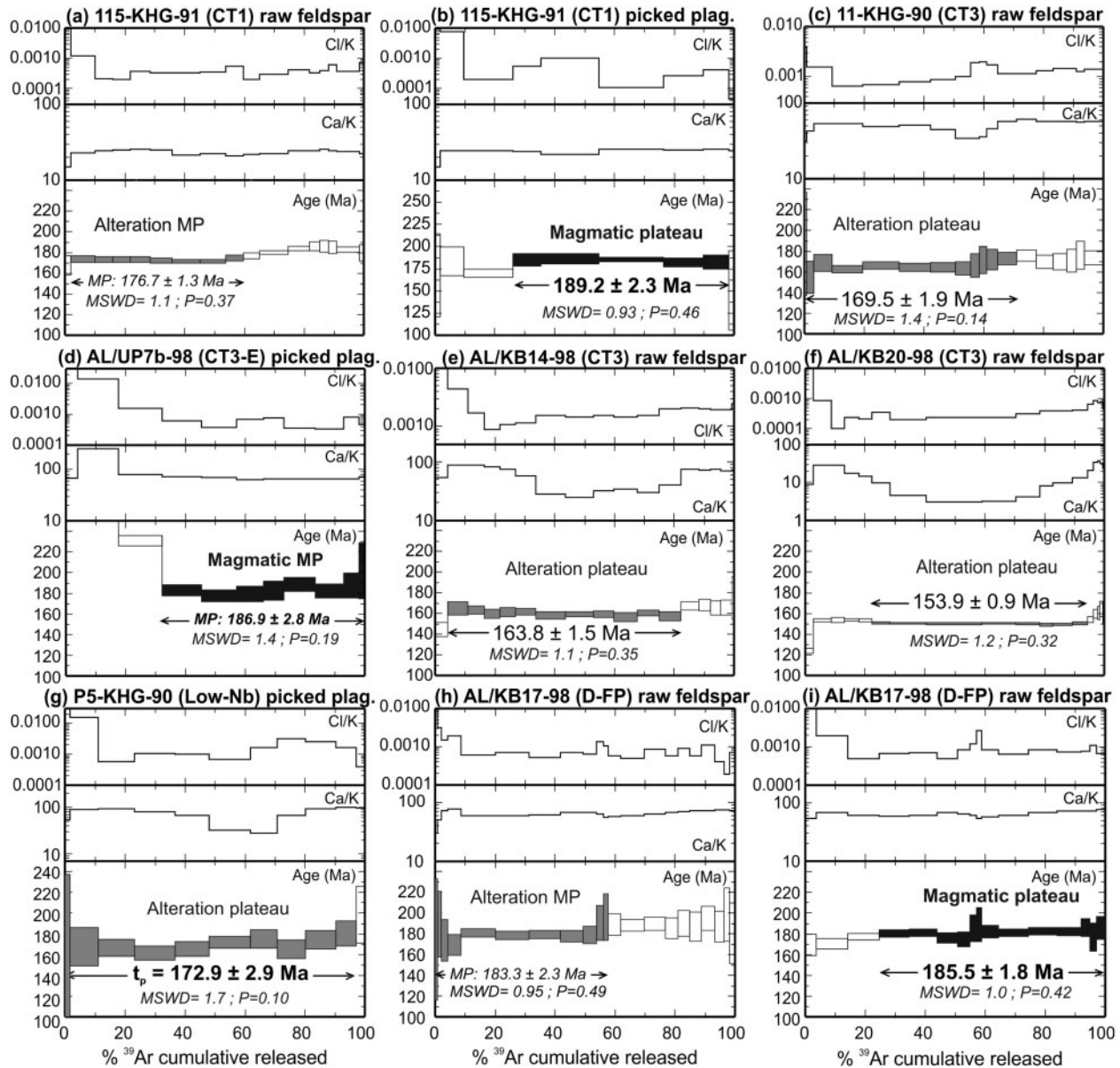
Fig. 9. Apparent ^{40}Ar/^{39}Ar age spectra and related Cl/K and Ca/K spectra indicating the age and composition of plagioclase (picked) and raw feldspar separates vs cumulative percentage of ^{39}Ar released. Reported 2σ errors do not include systematic errors. Plateau ages (>70% of ^{39}Ar released) and mini-plateau ages (MP; 50–70% of ^{39}Ar released) are indicated. Magmatic ages are interpreted to be those that exhibit high-temperature plateaux and limited variation in Ca/K and Cl/K (see text).

Muren dyke. The separated zircon fraction is dominated by brownish, translucent to turbid and fragmented crystals. Many of these contain a nucleus of dark brown mineral (baddeleyite?) that is parallel to the *c*-axis of the host. Rare colorless, transparent zircon crystals were also detected. A concordant fraction consisting of the most translucent fragments of brownish zircon (A) yielded a ^{206}Pb/^{238}U age of 182·2 ± 0·9 Ma, which we interpret as the crystallization age of the CT1-type West Muren dyke (Table 3; Fig. 8).

The U/Pb dating sample A1651 represents a coarse gabbro type from the middle zone of the CT1-type East Muren dyke and contains two types of zircons: (1) dark brown, transparent, prismatic zircons; (2) translucent to

transparent, pale-coloured, and elongated zircons with predominantly streaky crystal faces. Baddeleyite is found as rare platy crystals, although dark brown inclusions and intergrowths in type 2 zircon are probably baddeleyite as well (Table 3). A carefully hand-picked fraction of platy baddeleyite (D) yielded a U/Pb age of 182·2 ± 0·9 Ma (Fig. 8). Also, analysis of a fraction (E) of transparent, dark brown, prismatic type 1 zircons yielded a U/Pb age of 182·3 ± 1·1 Ma (Fig. 8). The combined age results of the two fractions gives a weighted mean age of 182·2 ± 0·76 Ma (MSWD = 0·043; P = 0·86) for the CT1-type East Muren dyke. In addition to these, a few analyses gave discordant age data; these are not discussed further.

Dating of the CT3 magma type

Six samples of the CT3 magma type were used for $^{40}Ar/^{39}Ar$ plagioclase dating. Two bulk fractions of sample 38-KHG-90 showed constantly rising step-heating patterns and did not yield meaningful ages. The bulk and hand-picked fractions of sample 113-KHG-91 also failed to provide an acceptable plateau age. The hand-picked fraction of sample 11-KHG-90 has a saddle-shape spectrum indicative of excess Ar and one of the bulk fractions yielded disturbed low-temperature age data corresponding to *c.* 170 Ma ages, but no plateau age could be calculated. The second bulk fraction, however, provided a low-*T* plateau age of 169·5 ± 1·9 Ma (MSWD = 1·4; *P* = 0·14) that includes 71% of ^{39}Ar released (Fig. 9c). The fact that this low-*T* plateau was obtained from the unpicked fraction (whereas no plateau was developed from the picked fraction) suggests that most of the $^{40}Ar*$ signal arises from sericite in the plagioclase. This is supported by the strongly structured Ca/K spectrum that shows a pronounced tilde-shaped pattern and variation between 32 and 57. The presence of only *c.* 10% of secondary sericite (K$_2$O ~10 wt %) can overprint the crystallization age of the plagioclase and yield the age of the sericitization event within a few per cent uncertainty (Jourdan *et al.*, 2009; Verati & Jourdan, 2014). Therefore, we do not regard this age to represent a reliable emplacement age, but rather the age of a secondary hydrothermal event.

Three samples of the CT3 magma type yielded robust plateau ages. First, a plagioclase phenocryst directly removed from the sample AL/UP7b-98 indicates considerable excess argon and variable Ca/K at low temperatures, probably owing to alteration (Fig. 9d). The high-temperature steps, however, show nearly constant Ca/K values and provide a mini-plateau age of 186·9 ± 2·8 Ma (MSWD = 1·4; *P* = 0·19) including 67% of ^{39}Ar released. We interpret this as the likely emplacement age of this CT3-E dyke. It is possible, however, that excess $^{40}Ar*$ may affect the mini-plateau so that we cannot preclude a somewhat younger emplacement age for the dyke intrusion. Second, whereas the hand-picked fraction of sample AL/KB14-98 was lost owing to a power cut during the measurement and one bulk fraction indicated an apparent age of *c.* 160 Ma (but gave no plateau), the other bulk fraction gave a plateau age of 163·8 ± 1·5 Ma (MSWD = 1·1; *P* = 0·35) Ma including nearly 80% of the ^{39}Ar liberated (Fig. 9e). Third, the hand-picked plagioclase fraction of dyke AL/KB20-98 yielded a low-resolution structured spectrum with highly variable Ca/K values and medium-*T* apparent ages as low as *c.* 148 Ma, whereas the bulk plagioclase fraction from the same dyke yielded a robust plateau age of 153·9 ± 0·8 Ma (MSWD = 1·2; *P* = 0·32) including 72% of ^{39}Ar (Fig. 9f). Given that the young plateau ages of 164 Ma and 154 Ma for samples AL/KB14-98 and AL/KB20-98, respectively, are associated with very structured, tilde-shaped Ca/K spectra, the plagioclase probably contained significant amounts of sericite and the plateau ages are more likely to correspond to secondary hydrothermal events than to the age of dyke emplacement (see Verati & Jourdan, 2014).

Summarizing, the CT3 $^{40}Ar/^{39}Ar$ age data are highly perturbed by a secondary process (see Zhang *et al.*, 2003). Nevertheless, one dyke yielded a mini-plateau $^{40}Ar/^{39}Ar$ age of 186·9 ± 2·8 Ma on plagioclase that we interpret as indicating the age of emplacement or at least a maximum age for the dyke. This age is coeval within error with the oldest Karoo ages from Africa (*c.* 186 Ma; recalculated from Jourdan *et al.*, 2008). The other mini-plateau and plateau ages at 170, 164 and 154 Ma rather indicate localized hydrothermal events that altered part or most of the plagioclase to sericite. The two ages at 164 and 154 Ma significantly post-date the preferred ages of Karoo CFB magmatism by 10–20 Myr and coincide with the incipient ocean spreading between Africa and Antarctica, which might explain the increase of hydrothermal activity during this period.

Dating of the Low-Nb magma type

Sample P5-KHG-90 represents the N-MORB-affinity Low-Nb magma type. The bulk plagioclase fraction did not yield a plateau, but the hand-picked plagioclase fraction yielded a robust plateau age of 172·9 ± 2·9 Ma (MSWD = 1·7; *P* = 0·09; 97% of ^{39}Ar liberated; Fig. 9g). However, although well developed, this plateau is associated with a pronounced tilde-shape Ca/K spectrum (Ca/K ranging from *c.* 95 to 25). We consider three possible explanations for obtaining such a well-developed plateau accompanied by a very variable Ca/K ratio: (1) the Ca/K variation indicates magmatic zoning in the grain and the age represents the intrusion age; (2) the Ca/K variation results from an alteration event synchronous with the magmatic age [see examples given by Jourdan *et al.* (2009)]; or (3) the Ca/K variation corresponds to an alteration event that totally overprinted the magmatic age of the plagioclase (alteration plateau age) and gives an age close or equal to the hydrothermal event, but unrelated to the age of magma emplacement. We regard case (1) to be unlikely and consider that the Ca/K variation stems from alteration (see Zhang *et al.*, 2003; Marzoli *et al.*, 2011). The alteration event may equally well have been concomitant with the emplacement or significantly younger. We therefore conclude that the N-MORB-affinity Low-Nb dyke was emplaced at or prior to 172·9 ± 2·9 Ma.

Dating of depleted ferropicrite suite

Samples AL/KB17-98, 117-KHG-91 and 128-KHG-91 represent basaltic dykes belonging to the depleted ferropicrite suite of Vestfjella (Heinonen & Luttinen, 2008). Generally, the $^{40}Ar/^{39}Ar$ spectra are complex, with samples 117-KHG-91 and 128-KHG-91 showing evidence of excess argon, notably old total integrated ages (*c.* 200–300 Ma), and Cl/K correlating positively with age in the low-*T* and high-*T* fractions (Supplementary Data Electronic Appendix 2). The intermediate-temperature steps yield imprecise ages of *c.* 180 Ma. The

hand-picked fraction of AL/KB17-98 did not yield a plateau age, but one of the bulk plagioclase fractions gave a mini-plateau age of 183.2 ± 2.3 Ma (MSWD = 0.95; P = 0.49) including 58% of ^{39}Ar released. The Ca/K spectrum shows only small variations, but the mini-plateau is part of an ambiguous double-deck age spectrum with the older portion yielding an apparent age of *c.* 191 Ma (Fig. 9h). The mini-plateau may be related to alteration processes, but we do not provide an unambiguous age for this fraction. On the other hand, the second bulk fraction gave a well-developed high-*T* plateau age of 185.5 ± 1.8 Ma (MSWD = 1.0; P = 0.42) including 75% of ^{39}Ar released and with a Ca/K spectrum showing only small variations, mostly between 60 and 75 (Fig. 9i). We regard the high-*T* plateau age of 185.5 ± 1.8 Ma to be robust and to indicate statistically indistinguishable emplacement ages for the depleted ferropicrites and the oldest Karoo CFBs in Africa [compare the age recalculated from Jourdan *et al.* (2008)]. We emphasize that our emplacement age for the Vestfjella depleted ferropicrite suite is compatible with studies that have associated generation of ferropicrites during the early stages of CFB magmatism (Gibson, 2002).

PETROGENESIS OF THE VESTFJELLA DYKE SWARM

Fractional crystallization of the magmas

The wide variation in MgO contents and Mg-numbers (Fig. 3; Table 1) and the presence of olivine, plagioclase, and clinopyroxene phenocrysts in the dolerite samples suggest a significant role for fractional crystallization in the evolution of the Vestfjella dyke swarm. Apart from the ferropicrite suites, the major element compositions of different extrusive and intrusive magma types show overlap suggestive of broadly similar parental melts and fractional crystallization history. Accordingly, we have modelled fractional crystallization using the PELE software (Boudreau, 1999) and an average of picritic Vestfjella samples (MgO = 12–19 wt %) as the parental melt composition (Supplementary Data Electronic Appendix 3). Owing to scattered geochemical trends and poorly constrained pressure conditions and water contents, numerous feasible models can be constructed by varying the model parameters. A decompression model shown in Fig. 3 provides a fairly good fit to our chemical and petrographic data on the dolerite and gabbro samples. In the model, olivine (Fo$_{87}$) starts to crystallize from the parental magma at 5 kbar. Subsequent crystallization is coupled with decompression from 5 to 1 kbar. During the rise of the magma, the differentiation process is first controlled by olivine fractionation until plagioclase and clinopyroxene become liquidus phases at *c.* 2.5 kbar when MgO$_{melt}$ is *c.* 7 wt %. At lower pressures, the model indicates a gabbroic fractionating assemblage of plagioclase (*c.* 50%), clinopyroxene (*c.* 30 %), and olivine (*c.* 20%). Except for the anomalous ferropicrite suites (see Heinonen & Luttinen, 2008), the geochemical compositions

of the Vestfjella magma types plot close to the modelled liquid line of descent. The CT3-E samples and the Low-Nb samples plot slightly above and below the modelled trend, respectively. In the case of CT1, there is considerable overlap with the modelled trend at relatively high MgO, but a clear plagioclase-in inflection is lacking, possibly owing to assimilation of felsic crustal materials as discussed below. Given that the compositional variations of the ferropicrite suites have been previously ascribed to polybaric (from 25 to 1 kbar) fractionation of olivine, Cr-spinel, clinopyroxene, and plagioclase (Heinonen & Luttinen, 2008), we conclude that the major element trends of the different magma types belonging to the Vestfjella dyke swarm have been largely controlled by fractional crystallization of high-Mg parental magmas.

Generation of the different magma types by contamination

Although the general major and trace element trends of the dolerite dykes and gabbros belonging to the Vestfjella dyke swarm can be explained by olivine, plagioclase, and clinopyroxene fractionation, generation of the magma types typified by different incompatible element and isotopic ratios (Figs 3–7) requires different magma sources or mixing processes, or both. With the exception of the DM-affinity depleted ferropicrite and Low-Nb magma types, the compositional characteristics are largely compatible with involvement of lithospheric materials during magma petrogenesis. Previous studies have favoured heterogeneous mantle sources to be primarily responsible for the compositional diversity of the Vestfjella low-Ti CFBs (Luttinen & Furnes, 2000). Here we explore the possibility that the different magma types could have been generated by contamination of a common parental magma type.

We have evaluated the role of crustal contamination using the energy-constrained assimilation and fractional crystallization model (EC-AFC), which simulates concurrent crystallization of the parental magma and partial melting of the crustal wall-rock (Spera & Bohrson, 2001). We have used an Archaean tonalite–trondhjemite–granodiorite (TTG) from the Kaapvaal craton and average upper crust to represent wall-rocks belonging to the Archaean Grunehogna craton and the Proterozoic Maud Belt, respectively (Table 6). In the case of SCLM contamination, we used AFC modelling (DePaolo, 1981) because of uncertainties regarding partial melting and dissolution processes in veined SCLM (e.g. Foley, 1992). A Vestfjella lamproite (Luttinen *et al.*, 2002) was used as a proxy for an SCLM-derived contaminant melt. For the parental melt composition we used the fractionation-corrected Low-Nb type sample P27-AVL (Table 6): this has the highest initial ε$_{Nd}$ of the Low-Nb samples and may well represent an uncontaminated magma type (see Luttinen & Furnes, 2000; Heinonen *et al.*, 2010). Rocks belonging to the depleted

Table 6: Input parameters for the EC-AFC (Spera & Bohrson, 2001) and AFC (DePaolo, 1981) models

Variable	PM†		AC*	PC*	SCLM*
Model	EC-AFC ± AFC		EC-AFC	EC-AFC	AFC
Magma liquidus T (initial T) [°C]	1500		-	-	-
Contaminant liquidus T [°C]	-		1000	1000	-
Contaminant initial T [°C]	-		600	600	-
Solidus T [°C]	-		850	850	-
Equilibration T [°C]	-		980	980	-
Isobaric specific heat [J/kg K]	1600		1370	1370	-
Crystallization enthalpy [J/kg]	400000		-	-	-
Fusion enthalpy [J/kg]	-		270000	270000	-
SiO_2 [wt. %]	47.85		-	-	-
TiO_2 [wt. %]	1.33		-	-	-
Al_2O_3 [wt. %]	10.56		-	-	-
FeO_{tot} [wt. %]	11.22		-	-	-
MnO [wt. %]	0.19		-	-	-
MgO [wt. %]	17.63		-	-	-
CaO [wt. %]	9.31		-	-	-
Na_2O [wt. %]	1.62		-	-	-
K_2O [wt. %]	0.17		-	-	-
P_2O_5 [wt. %]	0.11		-	-	-
		D_m			
Th [ppm]	0.17	(0.0003)	3.6	10.5	26.1
Nb [ppm]	2.35	(0.001)	5	12	170
Ta [ppm]	0.13	(0.001)	0.4	0.9	14.6
La [ppm]	3.73	(0.0003)	34.5	31	278
Ce [ppm]	9.17	(0.0003)	64	63	502
P [ppm]	491	(0.0003)	698	655	15099
Nd [ppm]	7.90	(0.0002)	22	27	229
Zr [ppm]	65	(0.001)	132	193	1076
Hf [ppm]	1.85	(0.0029)	3.4	5.3	26.6
Sm [ppm]	2.89	(0.0002)	3.52	4.7	36.4
Eu [ppm]	1.07	(0.0002)	1.01	1.0	10
Ti [ppm]	7970	(0.002)	1739	3837	23860
Gd [ppm]	3.26	(0.0003)	3.8	4.0	23
Tb [ppm]	0.59	(0.0005)	0.4	0.7	2.91
Y [ppm]	16.50	(0.001)	10	21	37
Yb [ppm]	1.30	(0.0052)	0.5	1.96	1.48
Lu [ppm]	0.20	(0.0085)	0.1	0.31	0.23
$^{143}Nd/^{144}Nd_{(t)}$	0.512829		0.510551	0.511800	0.512089
$\varepsilon_{Nd\ (t)}$	+8.3		−36.2	−11.8	−6.7

†Parental melt: Composition calculated by adding 33% of equilibrium olivine ($K_d(Fe-Mg)^{ol-liq} = 0.35$; Heinonen and Luttinen, 2010) into low-Nb sample P27-AVL (Luttinen and Furnes, 2000) until in equilibrium with depleted MORB source peridotite (Fo_{90}; Workman and Hart, 2005). Magma liquidus T estimated to be ∼100°C lower than the ones calculated with the methods of Putirka et al. (2007) and reported by Heinonen and Luttinen (2010) (cf. Coogan et al., 2014). Isobaric specific heat calculated using the partial molar isobaric heat capacities listed by Spera and Bohrson (2001). Crystallization enthalpy calculated and partition coefficients for the crystallizing magma (D_m) estimated using PELE software (Boudreau, 1999; olivine K_D values of Jean Bedard). Nd isotopic composition after the model of Heinonen et al. (2010).

*Lithospheric contaminants: Archaean crust (AC) – trace element and Nd isotopic composition after TTG sample 96/203 (Kreissig et al., 2000; U after sample 96/226-L; Ta and Hf estimated after average Ta/Nb and Hf/Zr presented in Kleinhanns et al., 2003); Upper Proterozoic crust (PC) – trace element composition after the average upper crust of Rudnick and Gao (2003) and Nd isotopic composition after the model of Jourdan et al. (2007a); Subcontinental lithospheric mantle – composition after lamproite AL/KB8-98 (Luttinen et al., 2002).

AFC process (r = 0.5) has been modeled to take place after 15% of olivine fractionation. In the case of crustal contaminants, the bulk partition coefficient values (D_c) of 0.1 and 0.5 were used for all elements (in two separate runs) and thermal parameters represent standard upper crustal case with initial temperatures taking account the effect of mafic underplating in an active continental rift setting (cf. Bohrson and Spera, 2001). Nd isotopic data reported at 180 Ma, except for the lamproite at 160 Ma.

ferropicrite suite probably also represent uncontaminated magmas, but they are too enriched in incompatible elements (i.e. low-degree melts; Heinonen *et al.*, 2010) to represent the parental magmas of the dolerite dykes and gabbros.

We emphasize that the model parameters have not been optimized to improve the fit of the models. For example, we have used the same *D* value (0·1 and 0·5 in two separate runs) for all incompatible elements in the partial melting of the crustal contaminants. This specific simplification leads to underestimation of inter-element fractionation during melting, but it also allows us to avoid speculations on poorly constrained restite mineralogy. Our quantitative modelling concentrates on HFSE, REE, and Nd isotopes, which are likely to be more resistant to secondary processes than LILE and Sr isotopes. We also consider that the EC-AFC modelling of Sr isotopes is significantly complicated by the poorly constrained behaviour of plagioclase-compatible Sr during wall-rock melting. The best-fit results of the
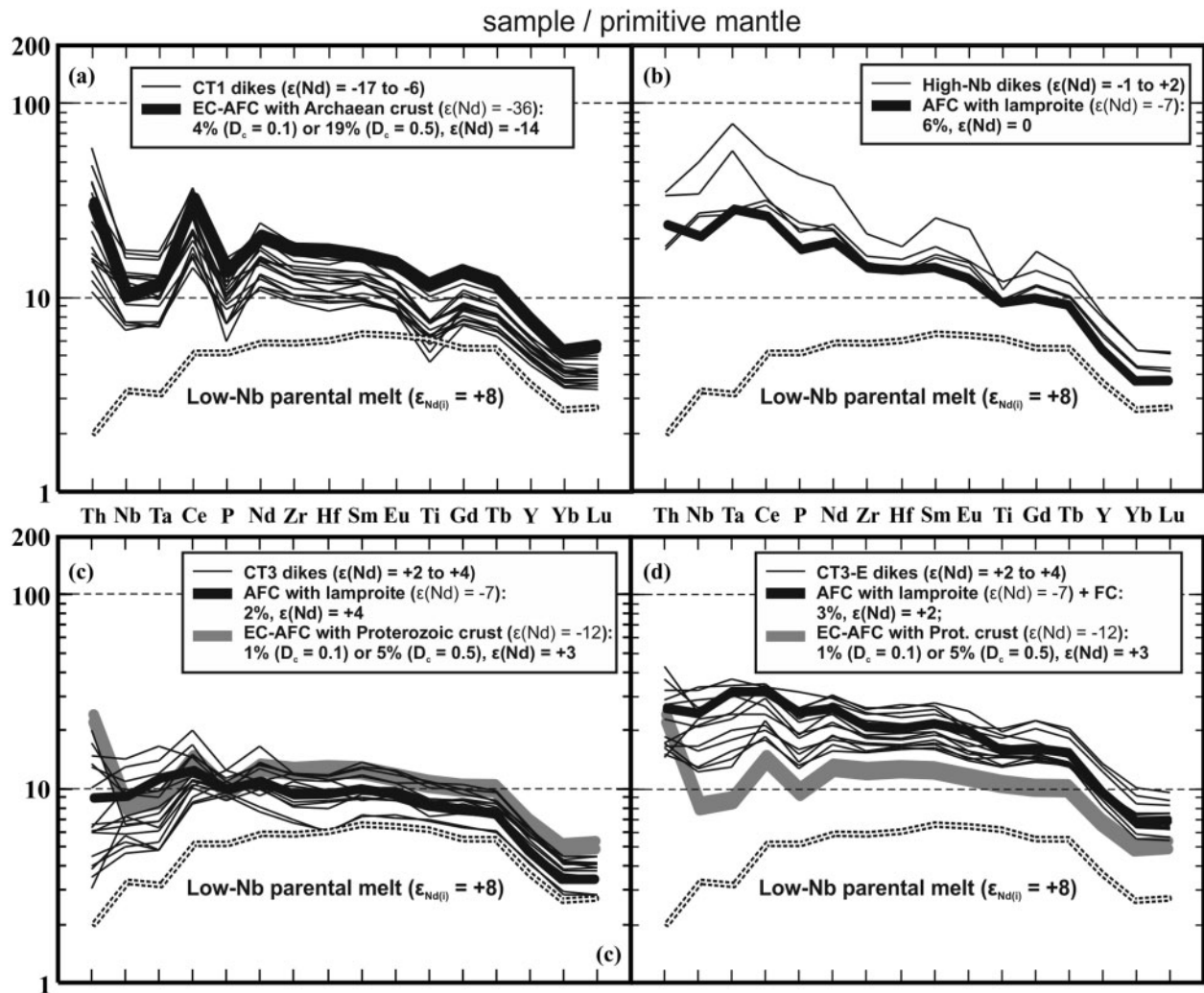
Fig. 10. Primitive mantle-normalized (Sun & McDonough, 1989) immobile incompatible element patterns and Nd isotopic compositions for (a) CT1 dykes, (b) High-Nb dykes, (c) CT3 dykes, and (d) CT3-E dykes. Compositions of fractionation-corrected Low-Nb parental melt and the best-fit results of EC-AFC and AFC contamination modeling of different magma types are indicated by dashed and continuous lines, respectively. The amount (%) of contaminant in the best-fit models [EC-AFC models with contaminant bulk partition coefficients (D_c) of 0·1 and 0·5] are indicated relative to the volume of the parental melt (see text and Table 6). In (d) the best-fit result represents AFC and subsequent fractional crystallization (until MgO ≈ 4 wt %; see Supplementary Data Electronic Appendix 3). In (c) and (d) contamination with Proterozoic crust can explain the elevated Th/Nb and Ce/Ta observed in some of the CT3 samples. Nd isotopic data are calculated at 180 Ma, except for the lamproite component used in the AFC models (160 Ma).

models are illustrated in Figs 10 and 11 and the petrogenetic model is summarized in schematic form in Fig. 12.

Generation of CT1 magma type

The CT1 dykes exhibit strong indications of a lithospheric component by their crust-like incompatible element and isotopic ratios; that is, high Th/Ta, La/Sm, Ce/Nb, and Ce/P and low Ti/Zr ratios and highly unradiogenic initial ε_{Nd} (Figs 5a and 6). Indeed, our model demonstrates that the salient features of CT1 can be modelled fairly well by combined fractional crystallization and contamination of a Low-Nb type parental magma with minor quantities (4–19% depending on the choice of *D* values for the assimilant) of Archaean crust-derived melt (Figs 10 and 11). In comparison,

contamination only with SCLM-sourced Vestfjella lamproite fails to explain the negative Nb and Ti anomalies as well as the lowest ε_{Nd} values of CT1 (see Fig. 10a). It is noteworthy, however, that the least-enriched CT1 samples exhibit lower Ti contents and Sm/Yb values than the hypothetical parental melt (Fig. 10a). This difference could indicate a HREE- and Ti-depleted crustal contaminant or, perhaps more likely, that the HREE and Ti were relatively more compatible during crustal melting (e.g. garnet in the restite) than in our simple model. Also, the parental melts of CT1 could have represented higher degree of partial melting and/or a more depleted source than in the case of the Low-Nb parental melt. In our view, adjustments of the model end-members would not significantly strengthen the feasibility of the contamination model.
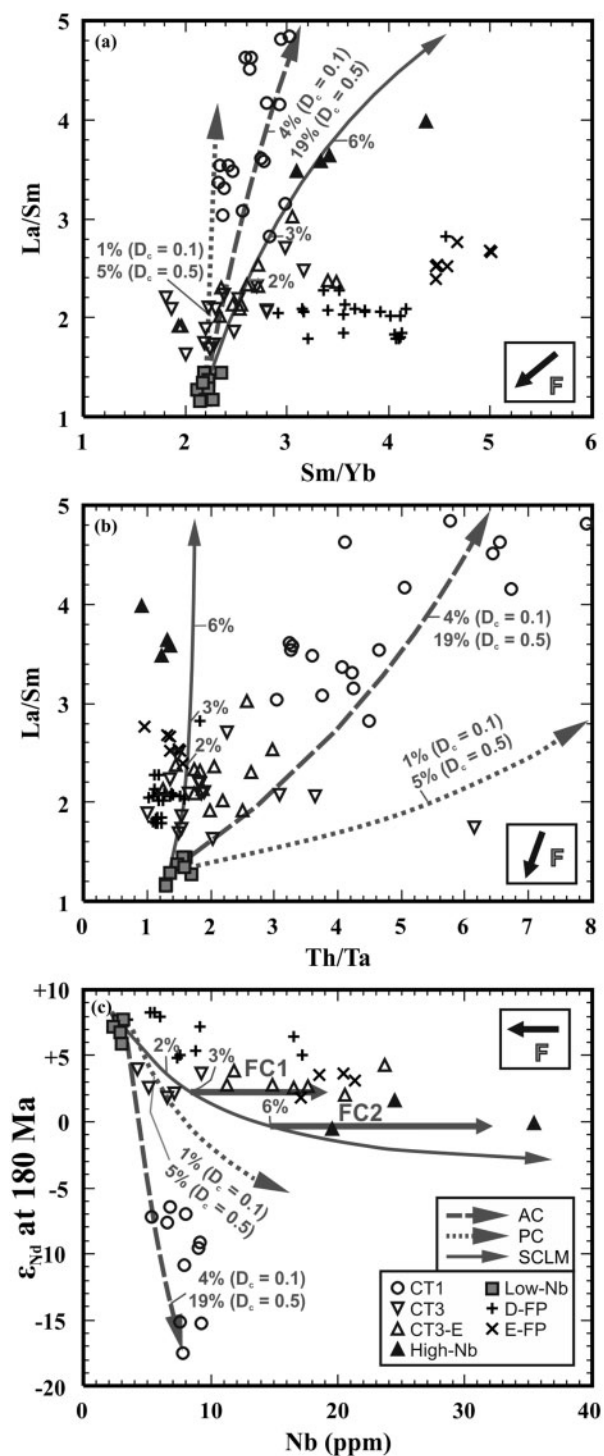
Fig. 11. (a) La/Sm vs Sm/Yb, (b) La/Sm vs Th/Ta, and (c) ε_{Nd} (at 180 Ma) vs Nb content of the Vestfjella dykes (D-FP, depleted ferropicrite suite; E-FP, enriched ferropicrite suite; see Supplementary Data Electronic Appendix 1 for data sources). The results of contamination modelling using Archaean crust (AC), Proterozoic crust (PC), and SCLM as contaminants are also shown (see text and Table 6). Tick-marks indicate the amount (%) of contaminant in the best-fit models relative to the volume of the parental melt (see Fig. 10) and *F* indicates the overall effect of increasing degree of melting. In (c) grey arrows labeled FC1 and FC2 indicate the effect of further fractional crystallization of SCLM-contaminated melts (FC1 = 3%; FC2 = 6%).

The contamination model for CT1 is also compatible with previously reported Nd and Sr isotope data for basalt-hosted silicic crustal xenoliths in Vestfjella (Luttinen & Furnes, 2000). These samples were not used in the EC-AFC models owing to incomplete chemical data, but their ε_{Nd}(180 Ma) (*c.* −50) and $^{87}Sr/^{86}Sr$ (180 Ma) (*c.* 0·710) values indicate availability of isotopically plausible Archaean crustal contaminants for CT1 in the Vestfjella region. Overall, we consider that our model lends support to a predominant crustal contaminant for CT1, but does not preclude involvement of additional minor SCLM-derived components (Fig. 12).

Generation of CT3 magma type

Geochemical similarities suggest a close genetic relationship between the Low-Nb and CT3 magma types (Fig. 5; Table 5). Overall, the CT3 magmas have relatively more enriched highly incompatible element contents, higher Th/Ta and Ce/P, and lower ε_{Nd}, which is compatible with mild contamination of CT3 with lithospheric material.

The incompatible element patterns of most CT3 dykes suggest that crustal material was not the principal contaminant and, in fact, they can be modelled fairly well by low-degree (2%) contamination of a Low-Nb parental magma with SCLM-derived melt (AFC model in Fig. 10c). Such a model, however, cannot account for the notably high incompatible element concentration levels of the CT3-E subtype (Fig. 10d). The high incompatible element and low MgO contents of CT3-E could be at least partially explained by a slightly higher degree of contamination (3%) and/or advanced fractional crystallization (AFC + FC model in Figs 10d and 11c), but a more enriched SCLM-derived melt (e.g. compared with Smoky Butte lamproites; Fraser *et al.*, 1985) or a less depleted parental magma than that used in our model may be required to explain the most extreme incompatible element enrichments of CT3-E (see Figs 3 and 11c). It is also important to note that the CT3 and CT3-E samples with anomalously high Th/Ta and Ce/Ta are likely to require an additional crustal contaminant or an SCLM-contaminant with more crust-like incompatible element ratios. For example, minor incorporation ($\leq$5%) of Proterozoic upper crust (see Figs 10c, d and 11b) could viably explain such trace element characteristics without resulting in negative ε_{Nd} values (see Fig. 10a). Overall, contamination of a Low-Nb parental magma with SCLM and/or Proterozoic crust provides a feasible explanation for the incompatible element and isotopic characteristics of the CT3 and CT3-E magma types (Fig. 12).

Generation of High-Nb magma type

The High-Nb magma type shows strongly enriched OIB-like mantle-normalized incompatible element patterns rather similar to those of the enriched ferropicrite suite (Fig. 5d). Many of their characteristic features, such as near-chondritic Sr–Nd isotopic ratios, high
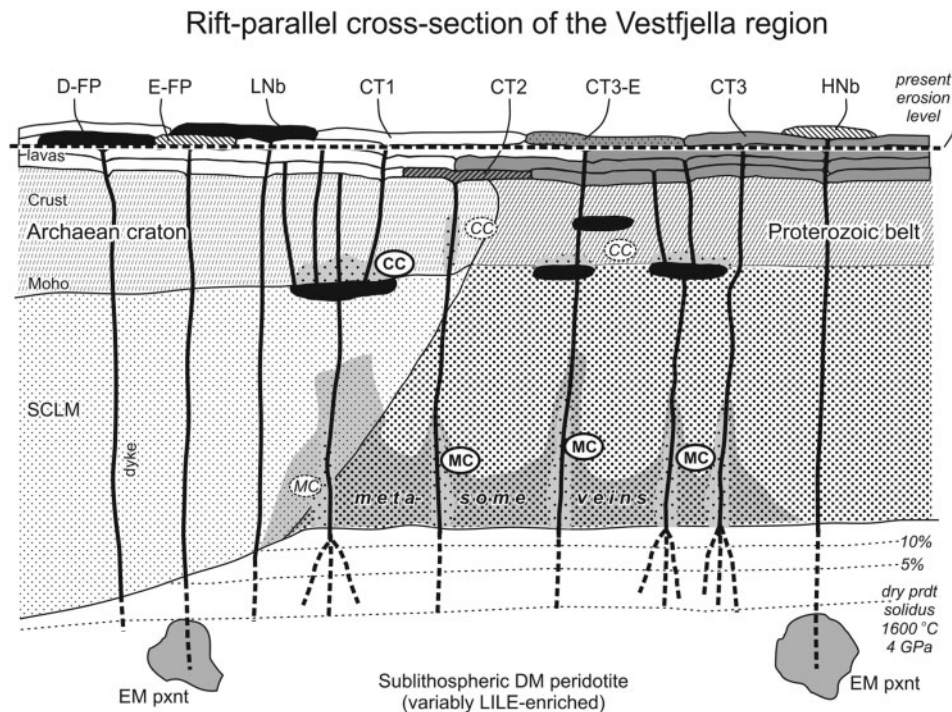
Fig. 12. Petrogenetic model for the Vestfjella CFB suite in a schematic cross-section along the Africa–Antarctica rift zone at 189–182 Ma (see text and Table 6). Initial partial melting of hot, sublithospheric DM peridotite at *c.* 4 GPa and 1600°C (Hirschmann, 2000) is broadly compatible with previous *P–T* estimates based on the depleted ferropicrite (D-FP) suite magmas (Heinonen & Luttinen, 2010). The Low-Nb and depleted ferropicrite magmas represent relatively higher and lower degrees of melting, respectively. Modification of DM-sourced magmas by contamination with crust (CC) and SCLM (MC) yielded diverse, enriched rift-assemblage magma types. At a relatively early stage contamination of Low-Nb magmas principally with Archaean crust produced CT1 lavas (CC), although contamination with SCLM material may also have occurred (MC). In contrast, contamination of Low-Nb magma with lamproite-like melts derived from metasomatic veins in the SCLM produced CT3 lavas (MC). At a relatively late stage, emplacement of contaminated CT1 and CT3 dykes and uncontaminated DM-sourced Low-Nb and depleted ferropicrite suite dykes, as well as OIB-type enriched ferropicrite suite (E-FP) and High-Nb dykes from pyroxenite-bearing enriched mantle domains, occurred coevally. The CT3-E dykes represent compositions modified by SCLM-contamination (MC) and subsequent fractional crystallization. CT3 and CT3-E that show high Th/Nb have been additionally contaminated with Proterozoic crust (CC). The origin of the CT2 lavas possibly resembled that of Th-enriched CT3 (see Luttinen & Furnes, 2000). The magma pathways through the lithosphere and the fusible metasomatic vein SCLM material may have originated as a result of the *c.* 1 Gyr multistage magmatic–tectonic history of the rift system (Jourdan *et al.*, 2004).

La/Sm and Sm/Yb, and the overall incompatible element patterns and Nd isotopic composition could be modelled fairly well by relatively high-degree (6%) contamination of a Low-Nb parental melt with SCLM material (Figs 10b and 11). On the other hand, the low Th/Ta of the High-Nb magma type is not readily explained by contamination with lithospheric materials. Given that Th/Ta is highly sensitive to incorporation of typical lithospheric material (see Table 6; Figs 10b and 11b), we consider that the High-Nb magma type is not derived from Low-Nb type magma, but represents melting of an enriched mantle source component similar to that inferred for the enriched ferropicrite suite by Heinonen *et al.* (2010) (Fig. 12).

Summary of contamination models
Our contamination models demonstrate that incorporation of highly enriched partial melts of SCLM and continental crust can effectively overprint DM-sourced parental magmas and lead to generation of diverse enriched CFB magma types. In the case of the Vestfjella

dyke swarm, the compositional features of the CT1 and CT3 magma types can be explained remarkably well by using a common Low-Nb type N-MORB-affinity parental melt, simple modelling parameters, and compositions of local or representative lithospheric rock types.

We emphasize two important implications of the contamination model. First, the application of EC-AFC modelling yields a relatively good fit for CT1 without the high degrees (>20%) of crustal contamination inferred from previous AFC models (see Luttinen & Furnes, 2000). Second, the modelling of CT3-E dykes demonstrates the possibility of generating high-Ti affinity magma types from low-Ti parental magmas by contamination.

Mantle sources
Depleted mantle
Available data show the 186 Ma depleted ferropicrite suite and the still loosely age-constrained (≥173 Ma) Low-Nb magma type to be isotopically (Sr, Nd, Pb, Os) indistinguishable from each other and from depleted

MORB-source mantle (DMM) (see Heinonen *et al.*, 2010). Furthermore, the primitive mantle-normalized incompatible element patterns of these magma types exhibit similar diagnostic features, despite notably different concentration levels (Fig. 5c). Combined, the available data suggest that the depleted ferropicrite suite and Low-Nb magma types represent, respectively, relatively low- and high-degree partial melts of the same garnet-bearing peridotitic (Heinonen & Luttinen, 2010) DM-like source in the sublithospheric mantle (Heinonen *et al.*, 2010) (Fig. 12).

Based on our contamination models, we consider that the same DM source was also involved in the generation of the numerous CT1 and CT3 dykes, as well as the voluminous CT1 and CT3 lavas (Figs 10–12). This interpretation has the fundamental implication that the great majority of the CFB magmas in the Vestfjella section of the Africa–Antarctica rift were primarily derived from relatively homogeneous DM sources (up to 80–100%; see Fig. 10).

It is important to note that some of the least-contaminated and least-altered samples of the Low-Nb magma type and the depleted ferropicrite suite have notably high LILE relative to HFSE (Fig. 5). In fact, this selective LILE enrichment characterizes all but few of the Vestfjella dykes (Fig. 5) and has been previously recognized as a key character of the Vestfjella lavas (Luttinen & Furnes, 2000). Crucially, the LILE enrichment does not correlate with visual or chemical indications of secondary alteration (e.g. Luttinen & Furnes, 2000) and is also decoupled from LREE enrichment, Nd and Sr isotopic compositions, and other typical geochemical indicators of crustal and SCLM contamination (e.g. Heinonen & Luttinen, 2008; Luttinen *et al.*, 2010). Regardless of the exact carrier of LILE (e.g. subduction-related fluid or recycled gabbro; see Luttinen & Furnes, 2000; Heinonen & Luttinen, 2008; Luttinen *et al.*, 2010), we regard the selective LILE enrichment to be an intrinsic feature of the DM source and point out that comparable LILE enrichments have been reported for hotspot-affinity basalts and picrites (e.g. Hofmann & Jochum, 1996; Sobolev *et al.*, 2000; Kent *et al.*, 2002) as well as from the Southwest Indian Ocean Ridge, the present manifestation of the Africa–Antarctica rift (le Roex *et al.*, 1989).

In summary, the geochemical characteristics of the depleted ferropicrite suite and the Low-Nb dykes, combined with the results of contamination models, suggest variably LILE-enriched, peridotite-dominated sublithospheric DM as the principal magma source of the Vestfjella CFBs (Fig. 12).

Enriched mantle
Enriched subcontinental lithospheric mantle has been widely regarded as the principal mantle source of many CFB magmas and has been the favoured mantle source also in the Karoo province (e.g. Hawkesworth *et al.*, 1984; Sweeney *et al.*, 1994; Luttinen & Furnes, 2000; Ellam, 2006; Jourdan *et al.*, 2007*a*). In the case of

low-Mg tholeiites, however, it is very difficult to distinguish an SCLM-sourced magma composition from one generated by mixing of DM-sourced magma with SCLM and/or crustal material. Bearing in mind the uncertainties related to the generation of voluminous, dry tholeiites from hydrous SCLM (e.g. Arndt *et al.*, 1993) and the results of our contamination models, we argue for the possibility that SCLM was not the preponderant mantle source of the Karoo magma types represented by the Vestfjella dyke swarm, but, instead, it was an important modifier of enriched CFBs (CT3).

The OIB-affinity enriched ferropicrite and High-Nb magma types probably represent magmas that have been insignificantly modified by contamination. Reliable age data for these dykes are unavailable, but greenschist-facies contact metamorphism of the High-Nb dykes implies emplacement prior to the adjacent $181 \cdot 2 \pm 0 \cdot 5$ Ma (recalculated from Zhang *et al.*, 2003) Utpostane layered intrusion. It also seems likely that the enriched ferropicrite dykes were emplaced during a relatively early stage or the main stage of Karoo magmatism; they are found close to the base of the >1 km thick lava succession and their amygdaloidal texture is suggestive of near-surface vesiculation (see Gerlach, 1986).

Heinonen & Luttinen (2008, 2010) and Heinonen *et al.* (2010) have previously suggested derivation of the enriched ferropicrites from pyroxenite-rich mantle sources. Our data on the High-Nb dykes are inadequate for detailed source characterization, but we consider that broadly similar, but not identical, pyroxenite-rich sources could have produced both the enriched ferropicrite and High-Nb magma types (Fig. 12). Given that the enriched ferropicrite and High-Nb magma types are unsuitable as parental magmas of other magma types and that they are found only as two small sets of closely spaced cross-cutting dykes at Basen and Utpostane, respectively, pyroxenite-dominated sources probably made volumetrically minor and temporally brief contributions to magmatism in the Vestfjella region.

Development of the Vestfjella rift section
The broadly seaward-dipping Vestfjella CFB lava succession and the crosscutting Vestfjella dyke swarm represent a section of the Africa–Antarctica rift that developed into a volcanic rifted margin during the Gondwana breakup process. Here we combine the available geochemical, petrological, and chronological data into a schematic evolutionary model of rift magmatism in Vestfjella (Fig. 12).

The early and main magmatic stages (181–189 Ma)
Our results and the previously published age data of Zhang *et al.* (2003) indicate an age range from 181 to 189 Ma for Karoo magmatism in Vestfjella. The >1 km thick volcanic succession exposed in Vestfjella has not been reliably dated; previous attempts have failed

owing to hydrothermal alteration of the lavas (Zhang *et al.*, 2003). The Vestfjella dyke swarm shows an intrusive relationship with the lava succession, however, and the dyke ages thus constrain the minimum age of the wall-rock flood basalts (see Fig. 12): our intrusive ages for the dolerite dykes and gabbros overlap with and exceed the preferred ages of Karoo CFB magmatism (Jourdan *et al.*, 2008). Most notably, dyke 115-KHG-91, dated at 189·2 ± 2·3 Ma, cross-cuts a *c.* 300 m thick sequence of lavas at the summit of nunatak Kjakebeinet (Fig. 2), which suggests that the Vestfjella dykes and lavas record up to *c.* 8 Myr of magmatic activity and include some of the earliest eruptions of the Karoo CFB province. This possibility is compatible with the presence of several sandstone intercalations between compound flow fields of CT1 and CT3 lavas (Hjelle & Winsnes, 1972; Luttinen *et al.*, 1998), which indicates contemporaneous effusive volcanism and sedimentation; that is, a relatively early stage of local eruptive activity (Jerram & Widdowson, 2005). Although this interpretation is also compatible with the characteristic association of ferropicrites with early stage CFB magmatism (Gibson, 2002), it is based on few age data and should be confirmed by additional well-defined isotopic ages before it is firmly accepted.

Geochemical data for the Vestfjella lavas and dykes suggest that an early stage of low-Ti (CT1 and CT3) and transitional-Ti (CT2) lava eruptions was followed by contemporaneous, although possibly periodic emplacement of low-Ti (CT1, CT3) and high-Ti affinity (CT3-E, High-Nb, the ferropicrite suites) magmas (Fig. 12). We consider that the wide compositional range of the Vestfjella magma types resulted essentially from diversification of DM-sourced magmas by melting and contamination processes and that the rare High-Nb and enriched ferropicrite suite dykes represent subordinate enriched components in the sublithospheric mantle (Fig. 12).

All of the Vestfjella lavas and dykes exhibit high Sm/Yb diagnostic of a high-pressure origin (see Fram & Lesher, 1993). Interestingly, the CT1 and CT3 dyke rocks are characterized by higher $(Sm/Yb)_N$ values (typically 2·4–3·0) than the wall-rock lavas (typically 2·0–2·4; see Luttinen & Furnes, 2000). This compositional change is contrary to the expected result of progressive rifting and could indicate lower average degrees of partial melting and cooling of the inferred DM source of the dykes (Fig. 12); however, compositional differences in the DM source or in lithospheric contaminants cannot be ruled out at present. The 181 Ma Utpostane layered gabbro intrusion (Fig. 2) represents the youngest dated CFB event and the only low Sm/Yb magma emplacement in Vestfjella (recalculated from Zhang *et al.*, 2003; Vuori & Luttinen, 2003). Rather than indicating rapid lithospheric thinning in the Vestfjella region, however, the low $(Sm/Yb)_N$ values (1·4 ± 0·1) and other geochemical evidence suggest that it is genetically linked to the plateau-assemblage low-Sm/Yb CFB lavas of Kirwanveggen and Sembberget (Luttinen *et al.*, 2010).

Overall, the geochemical and age data for the Vestfjella dyke swarm and the associated lavas do not indicate progressive thinning of the lithosphere within the Africa–Antarctica rift during the main stage of Karoo magmatism (see Tegner *et al.*, 1998).

The late tectono-magmatic stage (140–173 Ma)

The *c.* 173 Ma alteration plateau age of the Vestfjella Low-Nb dykes is marginally younger than the *c.* 176 Ma intrusive age of the late-stage Rooi Rand dykes in Africa (recalculated from Jourdan *et al.*, 2007*b*). As pointed out above, it is also possible that the *c.* 173 Ma alteration age only marginally postdates the intrusion age of the Low-Nb dykes, so that these geochemically N-MORB-type rocks (e.g. ε_{Nd} + 8) could represent late-stage magmatism in Vestfjella, although our geochemical models suggest production of Low-Nb type parental magmas of CT1 and CT3 already during the main stage.

The previously reported crystallization ages of amygdale K-feldspar at 140 and 152 Ma (recalculated from Zhang *et al.*, 2003) and our new 154, 164 and 170 Ma alteration plateau ages suggest prolonged hydrothermal activity in Vestfjella. Hydrothermal processes might have been associated with the development of the Antarctic rifted margin and contemporaneous with the assumed onset of seafloor spreading between Africa and Antarctica (Jokat *et al.*, 2003). Alternatively, the alteration events may have been caused by regional or local tectonic conditions (e.g. Jourdan *et al.*, 2009), or, alternatively, proximal magmatic activity, such as indicated by the 162 Ma lamproite intrusions of southern Vestfjella (recalculated from Luttinen *et al.*, 2002). We also cannot preclude the possibility that the 170–154 Ma alteration ages of the CT3 dykes only marginally postdate dyke emplacement, although we consider it improbable.

AFRICA–ANTARCTICA RIFT MAGMATISM

Evidence for diverse sublithospheric magma sources in the rift

Geochemical studies of the Africa–Antarctica rift zone have also demonstrated emplacement of MORB- and OIB-affinity magma types in the Ahlmannryggen region and the Lebombo Monocline (Duncan *et al.*, 1990; Sweeney *et al.*, 1994; Riley *et al.*, 2005). Here we review the available geochemical and chronological evidence for sublithospheric depleted and enriched mantle sources of the Karoo rift assemblage magmatism (Figs 13–15).

In western Dronning Maud Land, the uncontaminated Group 3 (ferropicrite) dykes of Ahlmannryggen have high ε_{Nd}(180 Ma) values (+7 to +9) and incompatible element ratios indicative of a broadly MORB-affinity depleted sublithospheric mantle source (Riley *et al.*, 2005) (Figs 13–15). Geochemical comparison indicates that the depleted sources of the Vestfjella and Ahlmannryggen magma types were different, however,
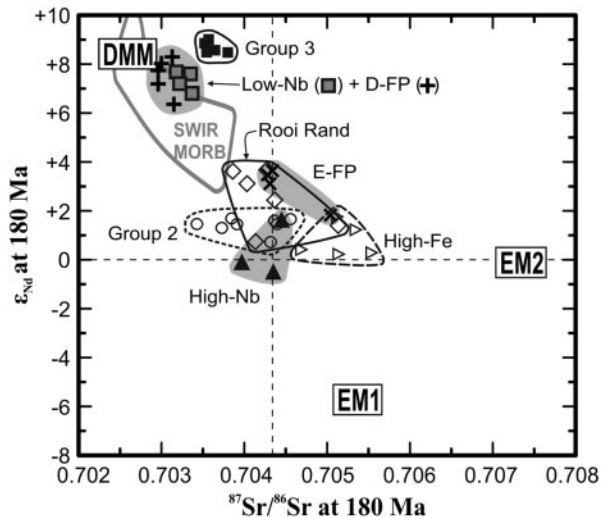
Fig. 13. Comparison of initial $^{87}Sr/^{86}Sr$ and ε_{Nd} values of MORB- and OIB-like rift-assemblage Low-Nb, High-Nb, depleted and enriched ferropicrite suites (this study; Luttinen & Furnes, 2000; Heinonen & Luttinen, 2008; Heinonen *et al.*, 2010), Rooi Rand (Hawkesworth *et al.*, 1984; Sweeney *et al.*, 1994), Group 2 and Group 3 (Riley *et al.*, 2005), and High-Fe (Sweeney *et al.*, 1994) magma types. DMM and SWIR MORB as in Fig. 6. Compositions of enriched mantle components EM1 and EM2 (Hart, 1988) have been back-calculated using Rb/Sr and Sm/Nd values reported by Willbold & Stracke (2006).

Fig. 14. Primitive mantle-normalized (Sun & McDonough, 1989) immobile incompatible element patterns for depleted (a), moderately enriched (b), and highly enriched (c) MORB- and OIB-like rift-assemblage Karoo magma types. Low-Nb, D-FP, E-FP, Group 2, and Group 3 are fairly homogeneous magma types and only representative samples are shown for clarity. Rooi Rand dyke swarm includes both LREE-depleted and moderately LREE-enriched samples. In the case of High-Fe lavas, REE data exist only for two samples. Data sources as in Fig. 13, apart from Rooi Rand magma type (Duncan *et al.*, 1990; Meth, 1996).

and that the latter contained a significant pyroxenite component (see Heinonen *et al.*, 2013, 2014). A sub-group of E-MORB-affinity dykes belonging to the Group 2 of Ahlmannryggen lack negative Nb anomalies (Fig. 14) and may represent uncontaminated magmas from mildly enriched sublithospheric mantle sources in the Ahlmannryggen rift section on the basis of their positive ε_{Nd} ($+1$ to $+2$) values and mildly LREE-enriched mantle-normalized incompatible element patterns (Riley *et al.*, 2005) (Figs 13 and 14). The Group 2 and Group 3 dykes of Ahlmannryggen have not yet been precisely dated, but existing age constraints are compatible with their generation during the early or main stage of Karoo magmatism (see Riley *et al.*, 2005).

At the conjugate African margin, the Rooi Rand dolerites form a geographically distinctive and geochemically exceptional dyke swarm in southern Lebombo (Armstrong *et al.*, 1984; Duncan *et al.*, 1990; Meth, 1996; Watkeys *et al.*, 2001) (Figs 1 and 15). The Rooi Rand dyke swarm and rare compositionally similar lavas and dykes in southern and central Lebombo (Fig. 15) have been recognized for their MORB affinities (Sweeney *et al.*, 1994; Jourdan *et al.*, 2007*b*). The available geochemical data show compositions ranging from LREE-depleted to LREE-enriched and existing isotopic data indicate ε_{Nd}(180 Ma) from $+1$ to $+4$ (Hawkesworth *et al.*, 1984; Duncan *et al.*, 1990; Sweeney *et al.*, 1994; Meth 1996) (Figs 13 and 14). Some of the mildly LREE-enriched Rooi Rand dykes show apparently uncontaminated mantle-normalized incompatible element patterns similar to those of Group 2 of Ahlmannryggen (Fig. 14b) and could
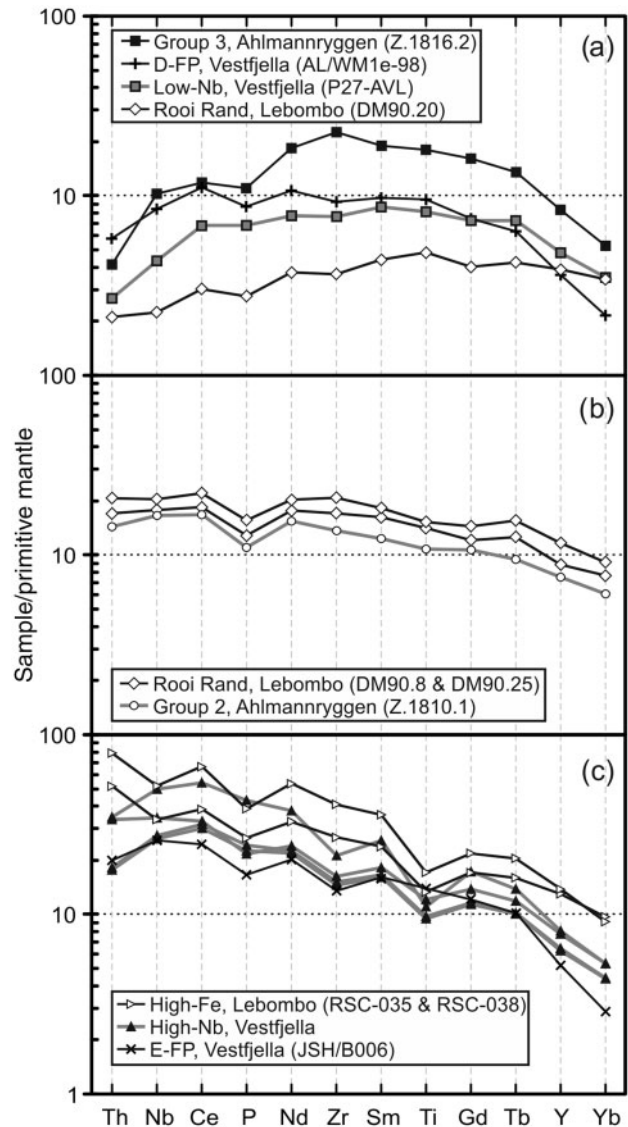
represent melting of an enriched sublithospheric mantle component along the southern and central Lebombo rift sections (Fig. 15). Recent $^{40}Ar/^{39}Ar$ plagioclase ages, however, indicate emplacement of the E-MORB-like Rooi Rand magma type at *c.* 176 Ma; that is, significantly after the main stage of Karoo rift-assemblage magmatism in the Lebombo Monocline (Jourdan *et al.* 2007*b*). The strongly LREE-depleted Rooi Rand dyke compositions (Meth, 1996; Watkeys *et al.*, 2001) (Fig. 14a) suggest melting of sublithospheric DM sources in the southern Lebombo rift section (Fig. 15),
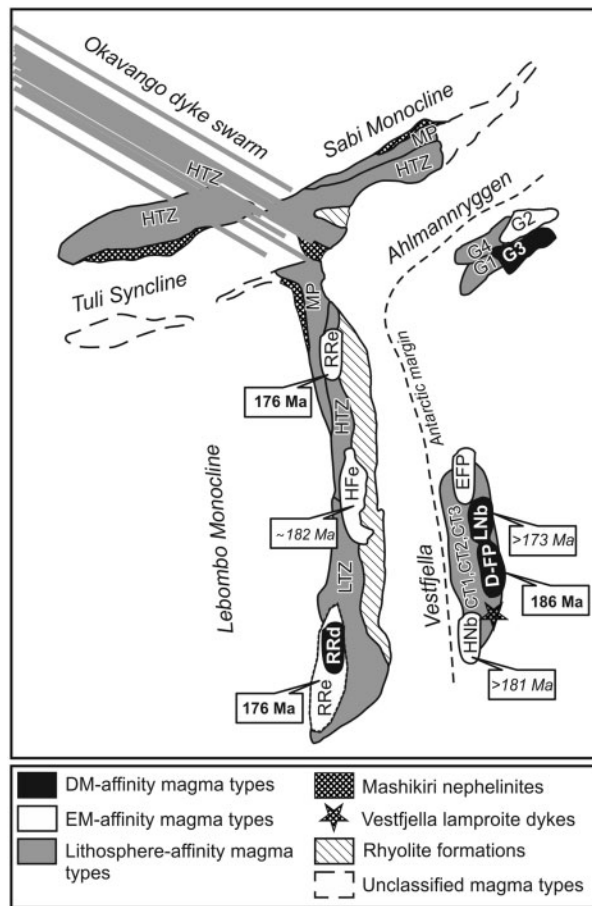
Fig. 15. Distribution of the predominant Karoo rift-assemblage magma types (schematic reconstruction is not to scale; modified after Cox & Bristow, 1984). Measured (bold) and inferred (italics) emplacement ages of the DM-affinity and EM-affinity magma types are indicated (see Riley *et al.*, 2004; recalculated from Zhang *et al.*, 2003; recalculated from Jourdan *et al.*, 2007*b*; this study). D-FP, depleted ferropicrite suite; LNb, Low-Nb dykes; E-FP, enriched ferropicrite suite; HNb, High-Nb dykes; G1–4, Group 1–4 dykes; RRd, LREE-depleted Rooi Rand dykes; RRe, LREE-enriched Rooi Rand dykes; HFe, High-Fe lavas and dykes; LTZ, low-Ti-Zr lavas and dykes; HTZ, high-Ti-Zr lavas and dykes; MP, Mwenezi picrites.

but isotopic and age data for this N-MORB-like variety of the Rooi Rand magma type are still lacking.

The OIB-affinity high-Fe magma type of central Lebombo represents a possible example of magmas derived from an enriched sublithospheric mantle (plume) source (Sweeney *et al.*, 1994) (Fig. 15). Representative samples show ε_{Nd}(180 Ma) from 0 to +2 and some chemical resemblance to the enriched ferro-picrite suite, High-Nb dykes, and Group 2 (Figs 13 and 14), which implies derivation of these magma types from broadly similar enriched mantle sources. However, small negative Nb anomalies are suggestive of some lithospheric contamination of the high-Fe CFB, such that their incompatible element and isotopic composition (e.g. relatively high initial $^{87}Sr/^{86}Sr$) may have been overprinted (compare our model for the CT3-E dykes). The high-Fe lavas and dykes have not been

dated, but they are intercalated with silicic volcanic units dated at *c.* 180–182 Ma using the U/Pb zircon sensitive high-resolution ion microprobe (SHRIMP) method (Riley *et al.*, 2004) (Fig. 15).

Overall, evidence from the MORB- and OIB-affinity CFBs from the Antarctic and African rifted margins points to emplacement of compositionally diverse sublithospheric mantle-derived magmas in the Vestfjella and Ahlmannryggen regions, and along the Lebombo Monocline at different evolutionary stages of the Karoo CFB province during the period 176–186 Ma (Fig. 15).

Importance of sublithospheric and lithospheric mantle sources

Magma types with lithospheric affinities are by far more abundant in the Africa–Antarctica rift-assemblage than MORB- or OIB-affinity magma types (Fig. 15). Conventionally, the numerous compositionally different low-Ti and high-Ti tholeiite magma types that exhibit lithosphere affinity in Vestfjella (low-Ti CT1and CT3, transitional-Ti CT2 lavas, and high-Ti CT3-E), Ahlmannryggen (low-Ti Group 1, high-Ti Group 4), the Lebombo Monocline (low-Ti–Zr and high-Ti–Zr basalts, high-Ti Mwenezi picrites), and the Okavango dyke swarm (high-Ti–Zr basalts) have been ascribed to principal magma sources within heterogeneous SCLM (e.g. Hawkesworth *et al.*, 1984; Ellam & Cox, 1989; Sweeney *et al.*, 1994; Luttinen & Furnes, 2000; Ellam, 2006; Jourdan *et al.*, 2007*a*). Such a hypothesis is compatible with the well-demonstrated similarity between the incompatible element and Nd and Sr isotopic compositions of the CFBs and South African mantle-derived xenoliths (e.g. Hawkesworth *et al.*, 1984) and spatially associated highly alkaline magma types (e.g. Mashikiri nephelinites, Harmer *et al.*, 1998; Vestfjella lamproites, Luttinen *et al.*, 2002) (see Fig. 15). The SCLM source model further avoids unrealistically high degrees of contamination implied by previous mixing and AFC models of lithosphere-affinity CFBs (e.g. Luttinen *et al.*, 1998). However, opinions differ as to whether relatively cool SCLM is a viable source for voluminous tholeiites, and whether dehydration melting of metasomatized SCLM is compatible with the dry phenocryst assemblages of CFBs (e.g. Arndt & Christensen, 1992).

Ellam & Cox (1991) were the first to propose that the geochemical characteristics and Nd isotopic compositions of the high-Ti Mwenezi picrites (previously referred to as the Nuanetsi picrites) resulted from contamination of N-MORB-like parental magmas with highly enriched SCLM-sourced lamproite-like melts. They further suggested that a similar mixing process could account for the lithosphere affinity of other Karoo CFB magma types. Subsequently, several studies have applied the 'SCLM-contamination' model using different kinds of parental magma types to address the petrogenesis of Karoo CFBs (Sweeney *et al.*, 1994; Luttinen & Furnes, 2000; Riley *et al.*, 2005; Ellam, 2006; Jourdan *et al.*, 2007*a*; Luttinen *et al.*, 2010). Overall, an important

role for SCLM-derived contaminants has been favoured, but the sublithospheric versus lithospheric source of the parental magmas has remained controversial. The presence of ≥173 Ma and 186 Ma DM-affinity (Low-Nb and depleted ferropicrite suite) magma types in Vestfjella confirms the involvement of sublithospheric DM sources in the Karoo rift-assemblage magmatism and, together with our EC-AFC and AFC models, lends new support to the feasibility of the Ellam & Cox (1991) hypothesis of a sublithospheric principal magma source in the case of Karoo rift-assemblage CFB. Importantly, the petrogenetic models demonstrate that it is theoretically possible to transform an N-MORB-affinity parental magma into diverse lithosphere-affinity low-Ti and high-Ti CFB magmas with only a minor quantity of highly incompatible element-enriched partial melt of lithospheric material (Figs 10 and 11). Although our study does not invalidate predominantly SCLM mantle sources for Karoo CFB, it suggests that, despite the limited occurrence of MORB- and OIB-like CFB, sublithospheric mantle may have been an important, or even the predominant source of the rift-assemblage magmas.

Rift-assemblage versus plateau-assemblage magmatism

In summary, we suggest that the voluminous lithosphere-affinity low-Ti and high-Ti CFBs of the rift-assemblage were produced by effective mixing of SCLM-derived melts and crustal material into sublithospheric mantle-sourced parental magmas as they ascended through the lithosphere. The magma pathways through thick lithosphere and the high abundance of fusible metasomatic vein SCLM material within the Africa–Antarctic rift may have originated as a result of the *c.* 1 Gyr multistage tectono-magmatic history proposed for the triple rift pattern (Jourdan *et al.*, 2004). Bearing in mind that reliable age data are not available for the rift-assemblage basalt and picrite lavas of the Lebombo Monocline, Mwenezi area, Sabi Monocline, Lupata area (Jourdan *et al.*, 2008) and Ahlmannryggen (Riley *et al.*, 2005), our 182–189 Ma emplacement ages of the Vestfjella dykes raise the question of whether at least some of these rift-assemblage CFBs might predate the province-wide 179–183 Ma main-stage CFBs (see Svensen *et al.*, 2007, 2012; Jourdan *et al.*, 2008) and represent the earliest phase of Karoo magmatism. Although this interesting interpretation calls for additional age constraints, our 173–154 Ma hydrothermal ages and the previously dated 162 Ma lamproites (recalculated from Luttinen *et al.*, 2002), as well as 151 and 140 Ma hydrothermal potassium feldspars (recalculated from Zhang *et al.*, 2003), provide evidence for continued magmatic and tectonic activity along the Antarctic rifted margin until the continental rift had transformed into a juvenile mid-ocean ridge system at 160–150 Ma (Jokat *et al.*, 2003); that is, long after the main magmatic stage and the assumed onset of oceanization along the African margin at 176 Ma (Jourdan *et al.*, 2007*b*; Klausen, 2009).

It is important to bear in mind that our study is focused on the Karoo rift-assemblage magmas only. Several previous studies have demonstrated that the relatively monotonous and more widespread plateau-assemblage CFBs are geochemically different from the rift-assemblage CFBs and were emplaced rapidly at 179–183 Ma (Duncan *et al.*, 1984; Furnes *et al.*, 1987; Harris *et al.*, 1990; Marsh *et al.*, 1997; Svensen *et al.*, 2007, 2012; Jourdan *et al.*, 2008). On the basis of diverging Nd and Sr isotopic trends (Fig. 6; see Elliot & Fleming, 2000) and different melting depths indicated by REE characteristics, it is even possible that the rift-assemblage and the plateau-assemblage CFBs represent different petrogenetic lineages derived from distinctive mantle sources (Jourdan *et al.*, 2007*a*; Luttinen *et al.*, 2010), although the principal sources of the voluminous plateau-assemblage CFB remain enigmatic owing to poorly constrained parental magma compositions (Jourdan *et al.*, 2007*a*; Neumann *et al.*, 2011). Overall, our results are compatible with the view that the petrogenesis and duration of Karoo CFB magmatism within the Africa–Antarctica triple rift and the surrounding lava plateaux may have been fundamentally different (see Cox, 1972; Elliot & Fleming, 2000; Jourdan *et al.*, 2007*a*; Luttinen *et al.*, 2010).

CONCLUSIONS

This study is focused on the CFB of the Africa–Antarctica rift (i.e. the Karoo rift-assemblage magmas). Combined, our age results and geochemical data and previously published data on the Vestfjella dykes lead to the following conclusions.

1. The Vestfjella dyke swarm cross-cuts Karoo CFB lavas at the rifted margin of western DML. The swarm is composed of geochemically diverse basaltic and picritic CFBs that can be grouped into seven Low-Ti and High-Ti tholeiitic magma types on the basis of their trace element and isotopic compositions: magma types CT1 (Low-Ti) and CT3 (Low-Ti) can be correlated with similarly designated CFB lavas of Vestfjella (CT2 is not found as dykes; see Luttinen & Furnes, 2000), whereas Low-Nb (Low-Ti), CT3-E (High-Ti), High-Nb (High-Ti) and the depleted (Trans-Ti) and enriched ferropicrite suites (High-Ti) are found only as dykes. The initial Nd and Sr isotope compositions calculated at 180 Ma exhibit wide ranges (ε_{Nd} from +8 to –17 and $^{87}Sr/^{86}Sr$ from 0·70318 to 0·71038, respectively) that span the whole compositional spectrum of Karoo CFB.
2. Our $^{40}Ar/^{39}Ar$ age data indicate a subsolidus overprint even in visually unaltered, hand-picked plagioclase fractions. Four dyke samples yielded plateau ages of 172·9 ± 2·9, 169·5 ± 1·9, 163·8 ± 1·5, and 153·9 ± 0·8 Ma that we interpret as alteration ages based on notably variable Ca/K signals. The plateau ages of 189·2 ± 2·3 Ma (CT1) and 185·5 ± 1·8 Ma

(depleted ferropicrite suite) and the mini-plateau age of $186·9 \pm 2·8$ Ma (CT3-E) exhibit consistent Ca/K and are interpreted as magma emplacement ages that predate the 179–183 Ma main stage of Karoo magmatism. Two indistinguishable $^{206}Pb/^{238}U$ zircon ages (CT1) of $182·2 \pm 0·7$ and $182·2 \pm 0·9$ Ma prove synchronous main-stage CFB magmatism in the African and Antarctic rift sections. The wide $^{40}Ar/^{39}Ar$ age range calls for further chronological constraints on the still poorly dated Karoo rift-assemblage magmatism.

3. The isotopically indistinguishable Low-Nb dykes and the depleted ferropicrite suite have MORB affinities and were derived from the same overall DM-type sublithospheric mantle source, whereas the rare High-Nb and the enriched ferropicrite suite dykes show broad OIB affinities and probably represent partial melts of enriched, possibly pyroxenite-bearing, components of the sublithospheric mantle. The currently available geochemical and isotopic data indicate the presence of heterogeneous depleted and enriched sublithospheric mantle components beneath the Vestfjella, Ahlmannryggen, and Lebombo sections of the Africa–Antarctica rift.

4. Our geochemical EC-AFC and AFC models indicate that the CT1, CT3, and CT3-E magma types were generated by crustal and SCLM contamination of Low-Nb type parental magmas, which suggests that sublithospheric depleted mantle may have been the predominant magma source in the Vestfjella rift section. The model for CT3-E dykes implies that high-Ti magmas with lithospheric geochemical characteristics can be generated by low-degree contamination of N-MORB-like (low-Ti) parental magmas and supports the view that depleted mantle may be the predominant source of the Karoo rift-assemblage CFB.

ACKNOWLEDGEMENTS

FUNDING

SUPPLEMENTARY DATA

Supplementary data for this paper are available at *Journal of Petrology* online.

REFERENCES

Armstrong, R. A., Bristow, J. W. & Cox, K. G. (1984). The Rooi Rand dyke swarm, southern Lebombo. In: Erlank, A. J. (ed.) *Petrogenesis of the Volcanic Rocks of the Karoo Province. Geological Society of South Africa Special Publication* **13**, 77–86.

Arndt, N. T. & Christensen, U. (1992). The role of lithospheric mantle in continental flood volcanism: Thermal and geochemical constraints. *Journal of Geophysical Research* **97**(**B7**), 10967–10981.

Arndt, N. T., Czamanske, G. K., Wooden, J. L. & Fedorenko, V. A. (1993). Mantle and crustal contributions to continental flood volcanism. *Tectonophysics* **223**, 39–52.

Aucamp, A. P. H., Wolmarans, L. G. & Neethling, D. C. (1972). The Urfjell Group, a deformed (?) early Paleozoic sedimentary sequence, Kirwanveggen, western Dronning Maud Land. In: Adie, R. J. (ed.) *Antarctica Geology and Geophysics*. Universitetsforlaget, pp. 557–561.

Barton, J. M., Jr, Klemd, R., Allsopp, H. L., Auret, S. H. & Copperthwaite, Y. E. (1987). The geology and geochronology of the Annandagstoppane granite, Western Dronning Maud Land, Antarctica. *Contributions to Mineralogy and Petrology* **97**, 488–496.

Bohrson, W. A. & Spera, F. J. (2001). Energy-constrained open-system magmatic processes II: Application of energy-constrained assimilation–fractional crystallization (EC-AFC) model to magmatic systems. *Journal of Petrology* **42**, 1019–1041.

Boudreau, A. E. (1999). PELE—a version of the MELTS software program for the PC platform. *Computers and Geosciences* **25**, 201–203 (Version 7.07 of the software downloaded in 2010 from http://fds.duke.edu/db/Nicholas/eos/faculty/boudreau).

Brewer, T. S., Rex, D., Guise, P. G. & Hawkesworth, C. J. (1996). Geochronology of Mesozoic tholeiitic magmatism in Antarctica: implications for the development of the failed Weddell Sea rift system. In: Storey, B. C., King, E. C. & Livermore, R. A. (eds) *Weddell Sea Tectonics and Gondwana Break-up. Geological Society, London, Special Publications* **108**, 45–61.

Burke, K. & Dewey, J. F. (1973). Plume-generated triple junctions: key indicators in applying plate tectonics to old rocks. *Journal of Geology* **81**, 406–433.

Coogan, L. A., Saunders, A. D. & Wilson, R. N. (2014). Aluminum-in-olivine thermometry of primitive basalts: Evidence of an anomalously hot mantle source for large igneous provinces. *Chemical Geology* **368**, 1–10.

Corner, B. (1994). Geological evolution of western Dronning Maud Land within a Gondwana framework: Geophysics subprogramme. Final project report to SACAR. Johannesburg: Department of Geophysics, Witwatersrand University, 21 pp.

Cox, K. G. (1972). The Karoo volcanic cycle. *Journal of the Geological Society, London* **128**, 311–336.

Cox, K. G. & Bristow, J. W. (1984). The Sabie River Basalt Formation of the Lebombo Monocline and south-east Zimbabwe. In: Erlank, A. J. (ed.) *Petrogenesis of the Volcanic Rocks of the Karoo Province. Geological Society of South Africa Special Publication* **13**, 125–147.

Cox, K. G., Bell, J. D. & Pankhurst, R. J. (1979). *The Interpretation of Igneous Rocks*. George Allen & Unwin, 450 pp.

DePaolo, D. J. (1981). Trace element and isotopic effects of combined wallrock assimilation and fractional crystallization. *Earth and Planetary Science Letters* **53**, 189–202.

Di Vincenzo, G. & Skála, R. (2009). ^{40}Ar–^{39}Ar laser dating of tektites from the Cheb Basin (Czech Republic): Evidence for

coevality with moldavites and influence of the dating standard on the age of the Ries impact. *Geochimica et Cosmochimica Acta* **73**, 493–513.

Duncan, A. R., Erlank, A. J. & Marsh, J. S. (1984). Regional geochemistry of the Karoo igneous province. In: Erlank, A. J. (ed.) *Petrogenesis of the Volcanic Rocks of the Karoo Province. Geological Society of South Africa Special Publication* **13**, 355–388.

Duncan, A. R., Armstrong, R. A., Erlank, A. J., Marsh, J. S. & Watkins, R. T. (1990). MORB-related dolerites associated with the final phases of Karoo flood basalt volcanism in Southern Africa. In: Parker, A. J., Rickwood, P. C. & Tucker, D. H. (eds) *Mafic Dykes and Emplacement Mechanisms; Proceedings of the Second International Dyke Conference*. Balkema, pp. 119–129.

Duncan, R. A., Hooper, P. R., Rehacek, J., Marsh, J. S. & Duncan, A. R. (1997). The timing and duration of the Karoo igneous event, southern Gondwana. *Journal of Geophysical Research* **102(B8)**, 18127–18138.

Ellam, R. M. (2006). New constraints on the petrogenesis of the Nuanetsi picrite basalts from Pb and Hf isotope data. *Earth and Planetary Science Letters* **245**, 153–161.

Ellam, R. M. & Cox, K. G. (1989). A Proterozoic lithospheric source for Karoo magmatism: evidence from the Nuanetsi picrites. *Earth and Planetary Science Letters* **92**, 207–218.

Ellam, R. M. & Cox, K. G. (1991). An interpretation of Karoo picrite basalts in terms of interaction between asthenospheric magmas and the mantle lithosphere. *Earth and Planetary Science Letters* **105**, 330–342.

Ellam, R. M., Carlson, R. W. & Shirey, S. B. (1992). Evidence from Re–Os isotopes for plume–lithosphere mixing in Karoo flood basalt genesis. *Nature* **359**, 718–721.

Elliot, D. H. & Fleming, T. H. (2000). Weddell triple junction: The principal focus of Ferrar and Karoo magmatism during initial breakup of Gondwana. *Geology* **28**, 539–542.

Erlank, A. J., Duncan, A. R., Marsh, J. S., Sweeney, R. J., Hawkesworth, C. J., Milner, S. C., Miller, R. M. & Rogers, N. W. (1988). A laterally extensive geochemical discontinuity in the subcontinental Gondwana lithosphere. In: *Geochemical Evolution of the Continental Crust, Conference Abstracts*. Poços de Caldas, Brazil, pp. 1–10.

Faure, G. & Elliot, D. H. (1971). Isotope composition of strontium in Mesozoic basalt and dolerite from Dronning Maud Land. *British Antarctic Survey Bulletin* **25**, 23–27.

Foland, K. A., Fleming, T. H., Heimann, A. & Elliot, D. H. (1993). Potassium–argon dating of fine-grained basalts with massive Ar loss: application of the $^{40}Ar/^{39}Ar$ technique to plagioclase and glass from the Kirkpatrick Basalt, Antarctica. *Chemical Geology* **107**, 173–190.

Foley, S. (1992). Vein-plus-wall-rock melting mechanisms in the lithosphere and the origin of potassic alkaline magmas. *Lithos* **28**, 435–453.

Fram, M. S. & Lesher, C. E. (1993). Geochemical constraints on mantle melting during creation of the North Atlantic basin. *Nature* **363**, 712–714.

Fraser, K. J., Hawkesworth, C. J., Erlank, A. J., Mitchell, R. H. & Scott-Smith, B. H. (1985). Sr, Nd and Pb isotope and minor element geochemistry of lamproites and kimberlites. *Earth and Planetary Science Letters* **76**, 57–70.

Furnes, H. & Mitschell, J. G. (1978). Age relationships of Mesozoic basalt lava and dykes in Vestfjella, Dronning Maud Land, Antarctica. *Norsk Polarinstitutt Skrifter* **169**, 45–68.

Furnes, H., Neumann, E. & Sundvoll, B. (1982). Petrology and geochemistry of Jurassic basalt dykes from Vestfjella, Dronning Maud Land, Antarctica. *Lithos* **15**, 295–304.

Furnes, H., Vad, E., Austrheim, H., Mitchell, J. G. & Garmann, L. B. (1987). Geochemistry of basalt lavas from Vestfjella and adjacent areas, Dronning Maud Land, Antarctica. *Lithos* **20**, 337–356.

Gale, A., Dalton, C. A., Langmuir, C. H., Su, Y. & Schilling, J. (2013). The mean composition of ocean ridge basalts. *Geochemistry, Geophysics, Geosystems* **14**, 489–518, doi:10.1029/2012GC004334.

Gerlach, T. (1986). Exolution of H_2O, CO_2, and S during eruptive episodes of Kilauea volcano, Hawaii. *Journal of Geophysical Research* **91**, 12177–12185.

Gibson, S. A. (2002). Major element heterogeneity in Archean to recent mantle plume starting-heads. *Earth and Planetary Science Letters* **195**, 59–74.

Grind, H., Siivola, J. & Luttinen, A. (1991). A geological overview of the Vestfjella Mountains in western Dronning Maud Land. *Antarctic Reports of Finland* **1**, 11–15.

Groenewald, P. B., Moyes, A. B., Grantham, G. H. & Krynauw, J. R. (1995). East Antarctic crustal evolution: geological constraints and modelling in western Dronning Maud Land. *Precambrian Research* **75**, 231–250.

Harmer, R. E., Lee, C. A. & Eglington, B. M. (1998). A deep mantle source for carbonatite magmatism: evidence from the nephelinites and carbonatites of the Buhera District, SE Zimbabwe. *Earth and Planetary Science Letters* **158**, 131–142.

Harris, C., Marsh, J. S., Duncan, A. R. & Erlank, A. J. (1990). The petrogenesis of the Kirwan Basalts of Dronning Maud Land, Antarctica. *Journal of Petrology* **31**, 341–369.

Harris, C., Watters, B. R. & Groenewald, P. B. (1991). Geochemistry of the Mesozoic regional basic dykes of western Dronning Maud Land, Antarctica. *Contributions to Mineralogy and Petrology* **107**, 100–111.

Hart, S.R. (1988). Heterogeneous mantle domains: Signatures, genesis, and mixing chronologies. Earth and Planetary Science Letters 90, 273–296.

Hawkesworth, C. J., Marsh, J. S., Duncan, A. R., Erlank, A. J. & Norry, M. J. (1984). The role of continental lithosphere in the generation of the Karoo volcanic rocks: evidence from combined Nd- and Sr-isotope studies. In: Erlank, A. J. (ed.) *Petrogenesis of the Volcanic Rocks of the Karoo Province. Geological Society of South Africa Special Publication* **13**, 341–354.

Heinonen, J. S. & Luttinen, A. V. (2008). Jurassic dikes of Vestfjella, western Dronning Maud Land, Antarctica: Geochemical tracing of ferropicrite sources. *Lithos* **105**, 347–364.

Heinonen, J. S. & Luttinen, A. V. (2010). Mineral chemical evidence for extremely magnesian subalkaline melts from the Antarctic extension of the Karoo large igneous province. *Mineralogy and Petrology* **99**, 201–217.

Heinonen, J. S., Carlson, R. W. & Luttinen, A. V. (2010). Isotopic (Sr, Nd, Pb, and Os) composition of highly magnesian dikes of Vestfjella, western Dronning Maud Land, Antarctica: A key to the origins of the Jurassic Karoo large igneous province? *Chemical Geology* **277**, 227–244.

Heinonen, J. S., Luttinen, A. V., Riley, T. R. & Michallik, R. M. (2013). Mixed pyroxenite–peridotite sources for mafic and ultramafic dikes from the Antarctic segment of the Karoo continental flood basalt province. *Lithos* **177**, 366–380.

Heinonen, J. S., Carlson, R. W., Riley, T. R., Luttinen, A. V. & Horan, M. F. (2014). Subduction-modified oceanic crust mixed with a depleted mantle reservoir in the sources of the Karoo continental flood basalt province. *Earth and Planetary Science Letters* **394**, 229–241.

Hirschmann, M. M. (2000). Mantle solidus: Experimental constraints and the effects of peridotite composition. *Geochemistry, Geophysics, Geosystems* **1**, 2000GC000070.

Hjelle, A. & Winsnes, T. (1972). The sedimentary and volcanic sequence of Vestfjella, Dronning Maud Land; Antarctic geology and geophysics. In: Adie, R. J. (ed.) *Antarctica Geology and Geophysics*. Universitetsforlaget, pp. 539–547.

Hofmann, A. W. & Jochum, K. P. (1996). Source characteristics derived from very incompatible trace elements in Mauna Loa and Mauna Kea basalts, Hawaii Scientific Drilling Project. *Journal of Geophysical Research* **101**(B5), 11831–11839.

Jacobs, J., Thomas, R. J. & Weber, K. (1993). Accretion and indentation tectonics at the southern edge of the Kaapvaal craton during the Kibaran (Grenville) orogeny. *Geology* **21**, 203–206.

Jerram, D. A. & Widdowson, M. (2005). The anatomy of Continental Flood Basalt Provinces: geological constraints on the processes and products of flood volcanism. *Lithos* **79**, 385–405.

Johnson, D. M., Hooper, P. R. & Conrey, R. M. (1999). XRF analysis of rocks and minerals for major and trace elements on a single low dilution Li-tetraborate fused bead. *Advances in X-ray Analysis* **41**, 843–867.

Jokat, W., Boebel, T., König, M. & Meyer, U. (2003). Timing and geometry of early Gondwana breakup. *Journal of Geophysical Research* **108**(B9), doi:10.1029/2002JB001802.

Jones, D. L., Duncan, R. A., Briden, J. C., Randall, D. E. & MacNiocaill, C. (2001). Age of the Batoka basalts, northern Zimbabwe, and the duration of Karoo Large Igneous Province magmatism. *Geochemistry, Geophysics, Geosystems* **2**, doi:10.1029/2000GC000110.

Jourdan, F., Féraud, G., Bertrand, H., Kampunzu, A. B., Tshoso, G., Le Gall, B., Tiercelin, J. J. & Capiez, P. (2004). The Karoo triple junction questioned: evidence from Jurassic and Proterozoic $^{40}Ar/^{39}Ar$ ages and geochemistry of the giant Okavango dike swarm (Botswana). *Earth and Planetary Science Letters* **222**, 989–1006.

Jourdan, F., Féraud, G., Bertrand, H., Kampunzu, A. B., Tshoso, G., Watkeys, M. K. & Le Gall, B. (2005). Karoo large igneous province: Brevity, origin, and relation to mass extinction questioned by new $^{40}Ar/^{39}Ar$ age data. *Geology* **33**, 745–748.

Jourdan, F., Bertrand, H., Schaerer, U., Blichert-Toft, J., Féraud, G. & Kampunzu, A. B. (2007a). Major and trace element and Sr, Nd, Hf, and Pb isotope compositions of the Karoo large igneous province, Botswana–Zimbabwe: lithosphere vs mantle plume contribution. *Journal of Petrology* **48**, 1043–1077.

Jourdan, F., Féraud, G., Bertrand, H. & Watkeys, M. K. (2007b). From flood basalts to the inception of oceanization: example from the $^{40}Ar/^{39}Ar$ high-resolution picture of the Karoo large igneous province. *Geochemistry, Geophysics, Geosystems* **8**, doi:10.1029/2006GC001392.

Jourdan, F., Féraud, G., Bertrand, H., Watkeys, M. K. & Renne, P. R. (2008). The $^{40}Ar/^{39}Ar$ ages of the sill complex of the Karoo large igneous province: Implications for the Pliensbachian–Toarcian climate change. *Geochemistry, Geophysics, Geosystems* **9**, doi:10.1029/2008GC001994.

Jourdan, F., Marzoli, A., Bertrand, H., Cirilli, S., Tanner, L. H., Kontak, D. J., McHone, G., Renne, P. R. & Bellieni, G. (2009). $^{40}Ar/^{39}Ar$ ages of CAMP in North America: Implications for the Triassic–Jurassic boundary and the ^{40}K decay constant bias. *Lithos* **110**, 167–180.

Juckes, L. M. (1972). *The geology of north-eastern Heimefrontfjella, Dronning Maud Land. British Antarctic Survey, Scientific Report* **65**, 44 pp.

Kent, A. J. R., Baker, J. A. & Wiedenbeck, M. (2002). Contamination and melt aggregation processes in continental flood basalts: constraints from melt inclusions in Oligocene basalts from Yemen. *Earth and Planetary Science Letters* **202**, 577–594.

Klausen, M. B. (2009). The Lebombo monocline and associated feeder dyke swarm: Diagnostic of a successful and highly volcanic rifted margin? *Tectonophysics* **468**, 42–62.

Kleinhanns, I. C., Kramers, J. D. & Kamber, B. S. (2003). Importance of water for Archaean granitoid petrology: a comparative study of TTG and potassic granitoids from Barberton Mountain Land, South Africa. *Contributions to Mineralogy and Petrology* **145**, 377–389.

Knaack, C., Cornelius, S. B. & Hooper, P. R. (1994). Trace element analyses of rocks and minerals by ICP-MS. GeoAnalytical Lab, Washington State University, Pullman, WA http://environment.wsu.edu/facilities/geolab/technotes/icp-ms_method.html.

Kreissig, K., Naegler, T. F., Kramers, J. D., van Reenen, D. D. & Smit, C. A. (2000). An isotopic and geochemical study of the northern Kaapvaal Craton and the Southern Marginal Zone of the Limpopo Belt: are they juxtaposed terranes? *Lithos* **50**, 1–25.

Krogh, T. E. (1973). A low-contamination method for hydrothermal decomposition of zircon and extraction of U and Pb for isotopic age determinations. *Geochimica et Cosmochimica Acta* **37**, 485–494.

Krogh, T. E. (1982). Improved accuracy of U–Pb zircon ages by the creation of more concordant systems using an air abrasion technique. *Geochimica et Cosmochimica Acta* **46**, 637–649.

Krynauw, J. R., Watters, B. R., Hunter, D. R. & Wilson, A. H. (1991). A review of the field relations, petrology and geochemistry of the Borgmassivet intrusions in the Grunehogna Province, western Dronning Maud Land, Antarctica. In: Thomson, M. R. A., Crame, J. A. & Thomson, J. W. (eds) *Geological Evolution of Antarctica; Proceedings of the Fifth International Symposium on Antarctic Earth Sciences*. Cambridge University Press, pp. 33–39.

Lawver, L. A., Gahagan, L. M. & Coffin, M. F. (1992). The development of paleoseaways around Antarctica. In: Kennett, J. P. & Warnke, D. A. (eds) *Antarctic Paleoenvironment: a Perspective on Global Change. American Geophysical Union, Antarctic Research Series* **56**, 7–30.

Leat, P. T., Luttinen, A. V., Storey, B. C. & Millar, I. L. (2006). Sills of the Theron Mountains, Antarctica: evidence for long distance transport of mafic magmas during Gondwana break-up. In: Hanski, E. J., Mertanen, S., Rämö, O. T. & Vuollo, J. (eds) *Dyke Swarms: Time Markers of Crustal Evolution*. Taylor & Francis, pp. 183–199.

Le Bas, M. J. (2000). IUGS reclassification of the high-Mg and picritic volcanic rocks. *Journal of Petrology* **41**, 1467–1470.

Le Gall, B., Tshoso, G., Jourdan, F., Féraud, G., Bertrand, H., Tiercelin, J. J., Kampunzu, A. B., Modisi, M. P., Dyment, J. & Maia, M. (2002). $^{40}Ar/^{39}Ar$ geochronology and structural data from the giant Okavango and related mafic dyke swarms, Karoo igneous province, northern Botswana. *Earth and Planetary Science Letters* **202**, 595–606.

Leitchenkov, G. L., Miller, H. & Zatzepin, E. N. (1996). Structure and Mesozoic evolution of the eastern Weddell Sea, Antarctica: history of early Gondwana break-up. In: Storey, B. C., King, E. C. & Livermore, R. A. (eds) *Weddell Sea Tectonics and Gondwana Break-up. Geological Society, London, Special Publications* **108**, 175–190.

le Roex, A. P., Dick, H. J. B. & Fisher, R. L. (1989). Petrology and geochemistry of MORB from 25°E to 46°E along the Southwest Indian Ridge: evidence for contrasting styles of mantle enrichment. *Journal of Petrology* **30**, 947–986.

Ludwig, K. R. (1991). *PbDat: A computer program for processing Pb–U–Th isotope data, version 1.21. US Geological Survey, Open-File Report* **88-542**, 35 pp.

Ludwig, K. R. (2008). *Isoplot 3.6: a geochronology toolkit for Microsoft Excel. Berkeley Geochronology Center, Special Publication* **4**, 77 pp.

Luttinen, A. V. & Furnes, H. (2000). Flood basalts of Vestfjella: Jurassic magmatism across an Archaean–Proterozoic lithospheric boundary in Dronning Maud Land, Antarctica. *Journal of Petrology* **41**, 1271–1305.

Luttinen, A. V., Rämö, O. T. & Huhma, H. (1998). Neodymium and strontium isotopic and trace element composition of a Mesozoic CFB suite from Dronning Maud Land, Antarctica: Implications for lithosphere and asthenosphere contributions to Karoo magmatism. *Geochimica et Cosmochimica Acta* **62**, 2701–2714.

Luttinen, A. V., Zhang, X. & Foland, K. A. (2002). 159 Ma Kjakebeinet lamproites (Dronning Maud Land, Antarctica) and their implications for Gondwana breakup processes. *Geological Magazine* **139**, 525–539.

Luttinen, A. V., Leat, P. T. & Furnes, H. (2010). Björnnutane and Sembberget basalt lavas and the geochemical provinciality of Karoo magmatism in western Dronning Maud Land, Antarctica. *Journal of Volcanology and Geothermal Research* **198**, 1–18.

Manninen, T., Eerola, T., Mäkitie, H., Vuori, S., Luttinen, A., Sénvano, A. & Manhica, V. (2008). The Karoo volcanic rocks and related intrusions in southern and central Mozambique. In: Pekkala, Y., Lehto, T. & Mäkitie, H. (eds) *GTK Consortium Geological Surveys in Mozambique 2002–2007. Geological Survey of Finland, Special Paper* **48**, 211–250.

Marschall, H. R., Hawkesworth, C. J., Storey, C. D., Dhuime, B., Leat, P. T., Meyer, H. & Tamm-Buckle, S. (2010). The Annandagstoppane Granite, East Antarctica: Evidence for Archaean Intracrustal recycling in the Kaapvaal–Grunehogna Craton from zircon O and Hf isotopes. *Journal of Petrology* **51**, 2277–2301.

Marsh, J. S., Hooper, P. R., Rehacek, J., Duncan, R. A. & Duncan, A. R. (1997). Stratigraphy and age of Karoo basalts of Lesotho and implications for correlations within the Karoo igneous province. In: Mahoney, J. J. & Coffin, M. F. (eds) *Large Igneous Provinces: Continental, Oceanic, and Planetary Flood Volcanism. American Geophysical Union, Geophysical Monograph* **100**, 247–272.

Marzoli, A., Jourdan, F., Puffer, J. H., Cuppone, T., Tanner, L. H., Weems, R. E., Bertrand, H., Cirilli, S., Bellieni, G. & De Min, A. (2011). Timing and duration of the Central Atlantic magmatic province in the Newark and Culpeper basins, eastern U.S.A. *Lithos* **122**, 175–188.

Mattinson, J. M. (2010). Analysis of the relative decay constants of ^{235}U and ^{238}U by multi-step CA-TIMS measurements of closed-system natural zircon samples. *Chemical Geology* **275**, 186–198.

McDonough, W. F. & Sun, S. S. (1995). The composition of the Earth. *Chemical Geology* **120**, 223–253.

Meth, D. L. (1996). The geology and geochemistry of the Rooi Rand Dyke Swarm. PhD thesis, University of Natal, Durban, 189 pp.

Neumann, E., Svensen, H., Galerne, C. Y. & Planke, S. (2011). Multistage evolution of dolerites in the Karoo Large Igneous Province, central South Africa. *Journal of Petrology* **52**, 959–984.

Peters, M. (1989). *Die Vulkanite im westlichen und mittleren Neuschwabenland, Vestfjella und Ahlmannryggen, Antarktika: Petrographie, Geochemie, Geochronologie, Palaeomagnetismus, geotektonische Implikationen. Alfred-Wegener-Institut für Polar- und Maareforschung, Berichte zur Polarforschung* **61**, 186 pp.

Peters, M., Haverkamp, B., Emmermann, R., Kohnen, H. & Weber, K. (1991). Palaeomagnetism, K–Ar dating and geodynamic setting of igneous rocks in western and central Neuschwabenland, Antarctica. In: Thomson, M. R. A., Crame, J. A. & Thomson, J. W. (eds) *Geological Evolution of Antarctica, Proceedings of the Fifth International Symposium on Antarctic Earth Sciences.* Cambridge University Press, pp. 549–555.

Putirka, K. D., Perfit, M., Ryerson, F. J. & Jackson, M. G. (2007). Ambient and excess mantle temperatures, olivine thermometry, and active vs passive upwelling. *Chemical Geology* **241**, 177–206.

Renne, P. R. (2014). Some footnotes to the optimization-based calibration of the $^{40}Ar/^{39}Ar$ system. In: Jourdan, F., Mark, D. F. & Verati, C. (eds) *Advances in 40Ar/39Ar Dating: from Archaeology to Planetary Sciences. Geological Society, London, Special Publications* **378**, 21–31.

Renne, P. R., Mundil, R., Balco, G., Min, K. & Ludwig, K. R. (2010). Joint determination of ^{40}K decay constants and $^{40}Ar*/^{40}K$ for the Fish Canyon sanidine standard, and improved accuracy for $^{40}Ar/^{39}Ar$ geochronology. *Geochimica et Cosmochimica Acta* **74**, 5349–5367.

Renne, P. R., Balco, G., Ludwig, K. R., Mundil, R. & Min, K. (2011). Response to the comment by W. H. Schwarz *et al.* on 'Joint determination of 40K decay constants and 40Ar*/40K for the Fish Canyon sanidine standard, and improved accuracy for 40Ar/39Ar geochronology' by P. R. Renne *et al.* (2010). *Geochimica et Cosmochimica Acta* **75**, 5097–5100.

Riley, T. R., Millar, I. L., Watkeys, M. K., Curtis, M. L., Leat, P. T., Klausen, M. B. & Fanning, C. M. (2004). U–Pb zircon (SHRIMP) ages for the Lebombo rhyolites, South Africa; refining the duration of Karoo volcanism. *Journal of the Geological Society, London* **161**, 547–550.

Riley, T. R., Leat, P. T., Curtis, M. L., Millar, I. L., Duncan, R. A. & Fazel, A. (2005). Early–Middle Jurassic dolerite dykes from Western Dronning Maud Land (Antarctica): Identifying mantle sources in the Karoo Large Igneous Province. *Journal of Petrology* **46**, 1489–1524.

Riley, T. R., Curtis, M. L., Leat, P. T., Watkeys, M. K., Duncan, R. A., Millar, I. L. & Owens, W. H. (2006). Overlap of Karoo and Ferrar magma types in KwaZulu-Natal, South Africa. *Journal of Petrology* **47**, 541–566.

Riley, T. R., Curtis, M. L., Leat, P. T. & Millar, I. L. (2009). The geochemistry of Middle Jurassic dykes associated with the Straumsvola–Tvora alkaline plutons, Dronning Maud Land, Antarctica and their association with the Karoo large igneous province. *Mineralogical Magazine* **73**, 205–226.

Rudnick, R. L. & Gao, S. (2003). The composition of the continental crust. In: Rudnick, R. L. (ed.) *The Crust. Treatise on Geochemistry 3.* Elsevier–Pergamon, pp. 1–64.

Ruotoistenmäki, T. & Lehtimäki, J. (1997). Analysis of bedrock geology and thermal gradients using geophysical ground measurements on glaciated terrain in Queen Maud Land, Antarctica. In: Ricci, C. A. (ed.) *The Antarctic Region: Geological Evolution and Processes.* Terra Antartica[Setter: Antartica - NB: this is the correct spelling], pp. 1149–1152.

Schoene, B., Crowley, J. L., Condon, D. J., Schmitz, M. D. & Bowring, S. A. (2006). Reassessing the uranium decay constants for geochronology using ID-TIMS U–Pb data. *Geochimica et Cosmochimica Acta* **70**, 426–445.

Sobolev, A. V., Hofmann, A. W. & Nikogosian, I. K. (2000). Recycled oceanic crust observed in 'ghost plagioclase' within the source of Mauna Loa lavas. *Nature* **404**, 986–990.

Spera, F. J. & Bohrson, W. A. (2001). Energy-constrained open-system magmatic processes I: General model and

energy-constrained assimilation and fractional crystallization (EC-AFC) formulation. *Journal of Petrology* **42**, 999–1018.

Stacey, J. S. & Kramers, J. D. (1975). Approximation of terrestrial lead isotope evolution by a two-stage model. *Earth and Planetary Science Letters* **26**, 207–221.

Sun, S. S. & McDonough, W. F. (1989). Chemical and isotopic systematics of oceanic basalts: Implications for mantle composition and processes. In: Saunders, A. D. & Norry, M. J. (eds) *Magmatism in the Ocean Basins. Geological Society, London, Special Publications* **42**, 313–345.

Svensen, H., Planke, S., Chevallier, L., Malthe-Sörensen, A., Corfu, F. & Jamtveit, B. (2007). Hydrothermal venting of greenhouse gases triggering Early Jurassic global warming. *Earth and Planetary Science Letters* **256**, 554–566.

Svensen, H., Corfu, F., Polteau, S., Hammer, Ø. & Planke, S. (2012). Rapid magma emplacement in the Karoo Large Igneous Province. *Earth and Planetary Science Letters* **325–326**, 1–9.

Sweeney, R. J., Duncan, A. R. & Erlank, A. J. (1994). Geochemistry and petrogenesis of central Lebombo basalts of the Karoo igneous province. *Journal of Petrology* **35**, 95–125.

Tegner, C., Lesher, C. E., Larsen, L. M. & Watt, W. S. (1998). Evidence from the rare-earth element record of mantle melting for cooling of the Tertiary Iceland plume. *Nature* **395**, 591–594.

Vaasjoki, M., Tapani Rämö, O. & Sakko, M. (1991). New U–Pb ages from the Wiborg rapakivi area: constraints on the temporal evolution of the rapakivi granite–anorthosite–diabase dyke association of southeastern Finland. *Precambrian Research* **51**, 227–243.

Verati, C. & Jourdan, F. (2014). Modelling effect of sericitization of plagioclase on the $^{40}K/^{40}Ar$ and $^{40}Ar/^{39}Ar$ chronometers: implication for dating basaltic rocks and mineral deposits. In: Jourdan, F., Mark, D. F. & Verati, C. (eds) *Advances in 40Ar/39Ar Dating: from Archaeology to Planetary Sciences. Geological Society, London, Special Publications* **378**, 155–174.

Vuori, S. K. (2004). Petrogenesis of the Jurassic gabbroic intrusions of Vestfjella, Dronning Maud Land, Antarctica. PhD thesis, University of Helsinki, 25 pp.

Vuori, S. K. & Luttinen, A. V. (2003). The Jurassic gabbroic intrusion of Utpostane and Muren: insights into Karoo-related plutonism in Dronning Maud Land, Antarctica. *Antarctic Science* **15**, 283–301.

Watkeys, M. K., Meth, D. L. & Harmer, R. E. (2001). The Rooi Rand Dyke Swarm, Southern Africa. In: *Proceedings of the 4th International Dyke Conference, Programme and Abstracts*. KwaZulu-Natal, South Africa, p. 31.

Willbold, M. & Stracke, A. (2006). Trace element composition of mantle end-members: Implications for recycling of oceanic and upper and lower continental crust. *Geochemistry, Geophysics, Geosystems* **7**, doi:10.1029/2005GC001005.

Wolmarans, L. G. & Kent, K. E. (1982). Geological investigations in western Dronning Maud Land, Antarctica—a synthesis. *South African Journal of Antarctic Research, Supplements* **2**, 93 pp.

Workman, R. K. & Hart, S. R. (2005). Major and trace element composition of the depleted MORB mantle (DMM). *Earth and Planetary Science Letters* **231**, 53–72.

Zhang, X., Luttinen, A. V., Elliot, D. H., Larsson, K. & Foland, K. A. (2003). Early stages of Gondwana breakup: the $^{40}Ar/^{39}Ar$ geochronology of Jurassic basaltic rocks from western Dronning Maud Land, Antarctica, and implications for the timing of magmatic and hydrothermal events. *Journal of Geophysical Research* **108**(**B9**), doi:10.1029/2001JB001070.